Sager, W., Hoernle, K., Höfig, T.W., Blum, P., and the Expedition 391 Scientists
*Proceedings of the International Ocean Discovery Program* Volume 391
publications.iodp.org

# Expedition 391 summary[1]

W. Sager, K. Hoernle, T.W. Höfig, A.J. Avery, R. Bhutani, D.M. Buchs, C.A. Carvallo, C. Class, Y. Dai, G. Dalla Valle, A.V. Del Gaudio, S. Fielding, K.M. Gaastra, S. Han, S. Homrighausen, Y. Kubota, C.-F. Li, W.R. Nelson, E. Petrou, K.E. Potter, S. Pujatti, J. Scholpp, J.W. Shervais, S. Thoram, S.M. Tikoo-Schantz, M. Tshiningayamwe, X.-J. Wang, and M. Widdowson[2]

[1] Sager, W., Hoernle, K., Höfig, T.W., Avery, A.J., Bhutani, R., Buchs, D.M., Carvallo, C.A., Class, C., Dai, Y., Dalla Valle, G., Del Gaudio, A.V., Fielding, S., Gaastra, K.M., Han, S., Homrighausen, S., Kubota, Y., Li, C.-F., Nelson, W.R., Petrou, E., Potter, K.E., Pujatti, S., Scholpp, J., Shervais, J.W., Thoram, S., Tikoo-Schantz, S.M., Tshiningayamwe, M., Wang, X.-J., and Widdowson, M., 2023. Expedition 391 summary. In Sager, W., Hoernle, K., Höfig, T.W., Blum, P., and the Expedition 391 Scientists, Walvis Ridge Hotspot. Proceedings of the International Ocean Discovery Program, 391: College Station, TX (International Ocean Discovery Program). https://doi.org/10.14379/iodp.proc.391.101.2023
[2] **Expedition 391 Scientists' affiliations.**



**Keywords**
International Ocean Discovery Program, IODP, *JOIDES Resolution*, Expedition 391, Walvis Ridge Hotspot, Site U1575, Site U1576, U1577, Site U1578, Site U1584, Site U1585, Earth Connections, Tristan-Gough-Walvis Hotspot, true polar wander, isotopic zonation, large low shear-wave velocity province, LLSVP

**Core descriptions**

**Supplementary material**

**References (RIS)**

**MS 391-101**
Published 11 October 2023

Funded by NSF OCE1326927

## Abstract

Hotspot tracks (chains of seamounts, ridges, and other volcanic structures) provide important records of plate motions, as well as mantle geodynamics, magma flux, and mantle source compositions. The Tristan-Gough-Walvis Ridge (TGW) hotspot track, extending from the active volcanic islands of Tristan da Cunha and Gough through a province of guyots and then along Walvis Ridge to the Etendeka flood basalt province, forms one of the most prominent and complex global hotspot tracks. The TGW hotspot track displays a tight linear age progression in which ages increase from the islands to the flood basalts (covering ~135 My). Unlike Pacific tracks, which are often simple, nearly linear chains of seamounts, the TGW track is alternately a steep-sided narrow ridge, an oceanic plateau, subparallel linear ridges and chains of seamounts (most are flat-topped guyots). The track displays isotopic zonation over the last ~70 My. The zonation appears near the middle of the track just before it splits into two to three chains of ridge- and guyot-type seamounts. Walvis Ridge, forming the older part of the track, is also overprinted with age-progressive late-stage volcanism, which was emplaced ~30–40 My after the initial eruptions and has a distinct isotopic composition. The plan for Expedition 391 was to drill at six sites, three along Walvis Ridge and three in the seamounts of the Guyot Province, to collect igneous rocks to better understand the formation of volcanic edifices, the temporal and geochemical evolution of the hotspot, and the variation in paleolatitudes at which the volcanic edifices formed.

After a delay of 18 days to address a shipboard Coronavirus (COVID-19) outbreak, Expedition 391 proceeded to drill at four of the proposed sites: three sites on Walvis Ridge around Valdivia Bank, an ocean plateau within the ridge, and one site on the lower flank of a guyot in the Center track of the Guyot Province, a ridge located between the Tristan subtrack (which extends from the end of Walvis Ridge to the islands of Tristan da Cunha) and the Gough subtrack (which extends from Walvis Ridge to Gough Island). The first hole was drilled at Site U1575, located on a low portion of the northeastern Walvis Ridge just north of Valdivia Bank. At this location, 209.9 m of sediments and 122.4 m of igneous basement were cored. The sediments ranged in age from Late Pleistocene (~0.43–1.24 Ma) to Late Cretaceous (Campanian; 72–78 Ma). The igneous basement comprised 10 submarine lava units consisting of pillow, lobate, sheet, and massive lava flows, the thickest of which was ~21 m. Most lavas are tholeiitic, but some alkalic basalts were recovered. A portion of the igneous succession consists of low-Ti basalts, which are unusual because they appear in the Etendeka flood basalts but have not been previously found on Walvis Ridge. Two holes were drilled at Site U1576 on the west flank of Valdivia Bank. The first of these holes was terminated because a bit jammed shortly after entering the igneous basement. Hole U1576A recovered a remarkable ~380 m thick sedimentary section consisting mostly of chalk covering a nearly complete sequence from Late Pleistocene (~0.43–1.24 Ma) to Late Cretaceous (Campanian; ~79–

81.38 Ma). These sediments display short and long cyclic color changes that imply astronomically forced and longer term paleoenvironmental changes. The igneous basement recovered in Hole U1576B yielded 11 submarine lava units (total thickness = ~65 m). The flows range from pillows to massive flows with compositions varying from tholeiitic basalt to basaltic andesite, only the second occurrence of the latter composition recovered from the TGW track thus far. These units are separated by seven sedimentary chalk units that range 0.1–11.6 m in thickness, implying a long-term interplay of sedimentation and lava eruptions. These intercalated sediments revealed Upper Cretaceous (Campanian) ages of ~77–79 Ma for the upper two interbeds and ~79–81.38 Ma for the lower beds. Coring at Site U1577, on the extreme eastern flank of Valdivia Bank, penetrated a 154.8 m thick sedimentary section ranging from the Paleocene (Thanetian; ~58.8 Ma) to Upper Cretaceous (Campanian; ~81.43–83.20 Ma). Igneous basement coring progressed only 39.1 m below the sediment/basalt contact, recovering three massive submarine tholeiitic basalt lava flows that are 4.1, 15.5, and >19.1 m thick, respectively. Paleomagnetic data from Sites U1577 and U1576 indicate that the former volcanic basement formed just before the end of the Cretaceous Normal Superchron and the latter during Chron 33r, shortly afterward. Biostratigraphic and paleomagnetic data suggest that Valdivia Bank becomes younger from east to west. Site U1578, located on a Center track guyot, provided a long and varied igneous section. After coring through 184.3 m of pelagic carbonate sediments mainly consisting of Eocene and Paleocene chalk (~55.64–63.5 Ma), Hole U1578A cored 302.1 m of igneous basement. Basement lavas are largely pillows but are interspersed with sheet and massive flows. Lava compositions are mostly alkalic basalts with some hawaiite. Several intervals contain abundant olivine (some fresh), and some of the pillow stacks consist of basalt with remarkably high Ti content. The igneous sequence is interrupted by 10 sedimentary interbeds consisting of chalk and volcaniclastics and ranging 0.46–10.19 m in thickness. Investigations of toothpick samples from the intercalated sediments were examined, each revealing the same age range of ~63.5–64.81 Ma (lower Paleocene; Danian). Paleomagnetic data display a change in basement magnetic polarity ~100 m above the base of the hole. Combining magnetic stratigraphy with biostratigraphic data, the igneous section is inferred to span >1 My.

Nearly 7 months after Expedition 391, *JOIDES Resolution* transited from Cape Town to the north Atlantic. During this transit (Expedition 397T), 7.9 days of ship time were used to drill two holes (U1584A and U1585A) at sites on the Gough and Tristan tracks that had been omitted because of COVID-19–related time loss on the earlier cruise. For both, coring was begun only a short distance above the igneous basement to save time. The 75.2 m thick section drilled in Hole U1584A contains two sedimentary units: clay-rich carbonate sediments overlie a pumice-dominated volcaniclastic deposit containing basalt fragments. Because the goal was to core basalt and the base of the volcaniclastic deposit was not imaged in the seismic profile, the hole was terminated early to save operation time for the next site. In Hole U1585A, coring penetrated a 273.5 m thick sediment section overlying an 81.2 m thick pile of massive basalt flows. The sediment section is divided into four units:

- The uppermost unit consists of nannofossil chalk;
- The two intermediate units contain alternating chalk and volcaniclastic sediments containing several breccia units; and
- The lowermost unit consists of volcanic breccia containing juvenile blocks, bombs, and accretionary lapilli.

This thick sedimentary section documents a transition from shallow-water volcanism to open-ocean sedimentation as the seamount subsided. The thick underlying basalt section is made up of four sparsely to highly phyric massive flows, the thickest of which is >43 m thick. Samples of these units are mostly basalt with a few trachybasalts and one trachyandesite.

Although the igneous penetration was less than planned, coring during Expeditions 391 and 397T obtained samples that clearly will lead to an improved understanding of the evolution of the TGW hotspot and its track. Reasonable recovery of fresh basalt in some holes provides ample samples for geochemical, geochronologic, and paleomagnetic studies. Good recovery of Late Cretaceous and early Cenozoic chalk successions provides samples for paleoenvironmental study.

# 1. Introduction

At ~3100 km in length, the Tristan-Gough-Walvis Ridge (TGW) volcanic chain is one of Earth's longest quasi-linear, intraplate features on the seafloor. It was one of the first proposed to have been formed by a hotspot (Wilson, 1963), which Morgan (1971) proposed was a mantle plume, a melting anomaly at the top of a narrow, buoyant, columnar upwelling of higher temperature mantle material. Unlike the Hawaiian-Emperor and Louisville Seamount chains in the Pacific, which are mostly simple chains of individual volcanic seamounts and considered archetypal plume trails (Clague and Dalrymple, 1989; Koppers et al., 2004), the TGW chain is highly complex in its morphology, isotope geochemistry, and history.

Morphologically, the TGW chain includes a continuous ridge (Frio Ridge) with a straight side and top corrugated with faults, an oceanic plateau (Valdivia Bank), elongated ridges subparallel to the overall ridge trend, chains of guyots, and scattered seamounts (Figure **F1**). The post–60 Ma volcanism (referred to as the Guyot Province) can be divided into two distinct tracks of seamounts, one extending from the end of Walvis Ridge to Tristan Island (the Tristan track) and the other from Walvis Ridge to Gough Island (the Gough track). These two chains are characterized by distinct Pb isotopic compositions, but both have enriched mantle one (EMI)-type geochemistry (Rohde et al., 2013a; Hoernle et al., 2015). This represents the longest-lived hotspot zonation recognized thus far. A ridge and seamounts on the boundary of the Tristan and Gough subtracks have been considered as a separate Center track by some, but it is not clear whether its isotopic signature represents mixing of the Tristan and Gough end-members or constitutes a third distinct geochemical composition. The older Walvis Ridge (pre–70 Ma) has a Gough-type EMI isotopic composition. Younger guyot-type seamounts with a different high μ (HIMU)-type composition (high time-integrated U/Pb ratio resulting in radiogenic Pb isotope ratios) overlie the flat-topped and faulted Walvis Ridge basement. Both the EMI-type TGW chain and the HIMU seamounts continuing into Africa display remarkably linear age progressions, offset by 30–40 My, which are interpreted as reflecting two distinct plumes derived from distinct portions of the large low-shear velocity province (LLSVP) at the base of the lower mantle (Homrighausen et al., 2018, 2019, 2020). Moreover, the Valdivia Bank Plateau of Walvis Ridge apparently formed on the boundary of a

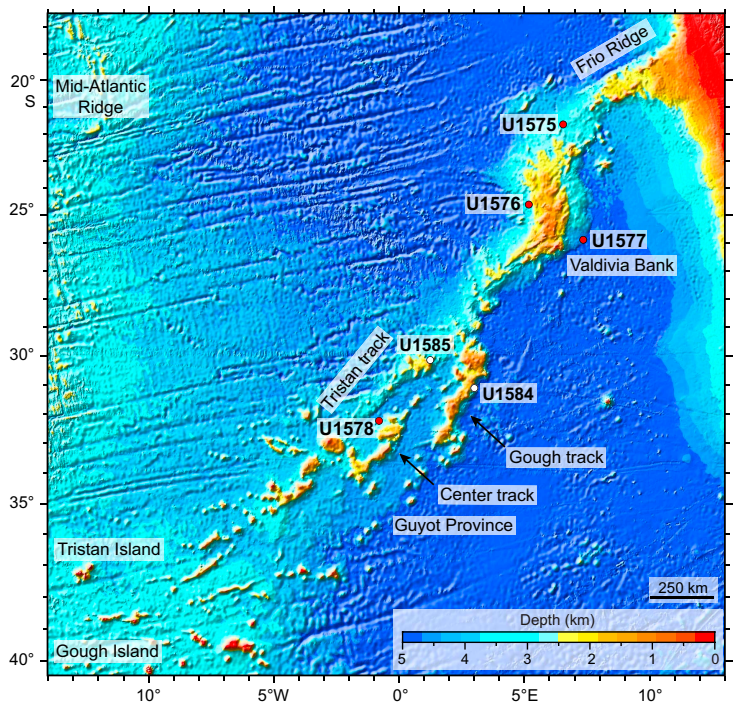


**Figure F1.** Bathymetry of Walvis Ridge with feature names. Red dots = Expedition 391 cored drill sites, white dots = Expedition 397T cored drill sites. Base map is satellite-altimetry predicted depths (Smith and Sandwell, 1994).

microplate, which may have affected its development along with that of its conjugate, the Rio Grande Rise on the South American plate (Sager et al., 2021).

The TGW chain is also an important geodynamic indicator. It is nearly antipodal to the Hawaiian-Emperor chain, which has been the fodder for debates about the fidelity of seamount chains to define plate motions relative to the underlying mantle. Two phenomena that can cause hotspot motion are mantle flow and true polar wander (TPW; the shift of the spin axis relative to the Earth's mantle). Because the two hotspots are nearly antipolar, if there was significant TPW during the Late Cretaceous and Cenozoic, the effect should be a coherent shift with Pacific and Atlantic hotspots (nominally, in the opposite direction from Hawaii). If other phenomena, such as plume motion, are the cause of TGW chain paleolatitude shifts, they are predicted to be in the same direction as Hawaii (Doubrovine et al., 2012). Moreover, the TGW track is the longest and most continuous on the African plate, so it plays an outsized role in determining the absolute motion of that plate. Thus, a better definition of the TGW chain age progression and paleolatitude is important for refining absolute plate motion models.

Owing to its complex nature, the TGW track can give important insights into (1) the interaction of mantle plume(s) with the Mid-Atlantic Ridge, (2) plume geochemical zonation, (3) complications (e.g., morphological and geochemical) related to a second hotspot event superimposed onto the first, (4) microplate formation, (5) plume movement, and (6) TPW. Expeditions 391 and 397T sought to explore these complexities by coring at six locations, three in the Guyot Province and three on Valdivia Bank (Figure **F1**).

The original plan for Expedition 391 included drilling at six sites, three on the older Walvis Ridge near Valdivia Bank and three in the Guyot Province just southeast of the split into two or three separate tracks. Unfortunately, Expedition 391 began in Cape Town, South Africa, during a spike in the COVID-19 pandemic, and an outbreak occurred on board. This required a return to Cape Town and a wait at the dock until the virus was eliminated from the ship. Eventually, this was achieved but at a loss of almost one-third of the allotted ship time. A pared-down plan was conceived to visit four of the six sites (Figure **F1**) with reduced time for deep penetration. The focus was to core the three sites on Valdivia Bank to gain an understanding and timing of the formation of that edifice and to core the Center track in the Guyot Province because it would be central to addressing geochemical zonation and paleolatitude questions. Later, during Expedition 397T, a transit from Cape Town to Lisbon, an opportunity arose to regain some of the lost drilling time. The two omitted sites in the Guyot Province were cored, penetrating to basaltic crust in one.

Drilling during Expedition 391 cored total sedimentary (Figure **F2**) and igneous (Figure **F3**) thicknesses of 949.6 m and 546.9 m, respectively. Expedition 397T added coring of 348.7 m of sediment and 81.2 m of igneous rock, making two expedition totals of 1298.3 m and 628.1 m. Drilling at Site U1575 on the northern Valdivia Bank penetrated 209.9 m of sediment and sedimentary rock and 122.4 m of igneous material comprising 10 units for 332.3 m total depth. Drilling at Sites U1576 and U1577 penetrated the west and east flanks of Valdivia Bank. Two holes at U1576 traversed 380.2 and 385.4 m of sediment and 17.9 and 64.9 m of basalt flows intercalated with sediment, totaling 398.1 and 450.3 m of total depth, respectively. The basement succession consists of 12 igneous units and 7 sedimentary interbeds. Site U1577 penetrated 154.8 m of sediment and 39.1 m of massive basalt flows, totaling 193.9 m. Site U1578, situated on the distal flank of a guyot, cored 184.3 m of sediment and 302.1 m of intercalated lava flows and sediment, ending at 486.4 mbsf. The igneous section at this site contains 12 volcanic units interspersed with 10 sedimentary interbeds. Coring at Site U1584 traversed 75.2 m of clay- and volcaniclastic-rich carbonate sediments lying atop pumice-dominated volcaniclastics. At Site U1585, a 273.5 m sedimentary section ranges from volcanic breccias to carbonate ooze. Beneath is an 81.2 m section with massive basalt flows.

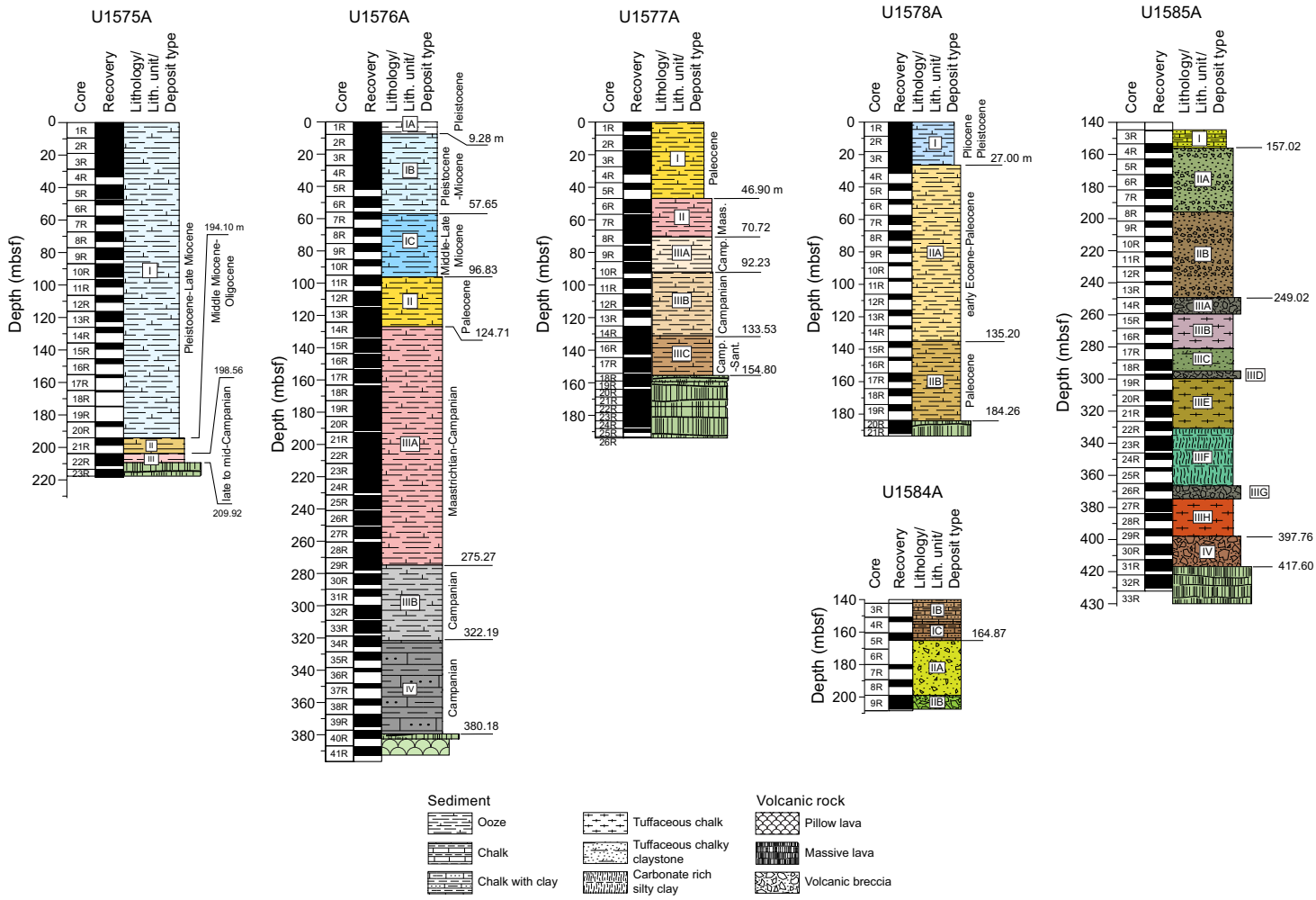


**Figure F2.** Lithostratigraphic summary of sediments, Holes U1575A, U1576A, U1577A, U1578A, U1584A, and U1585A.

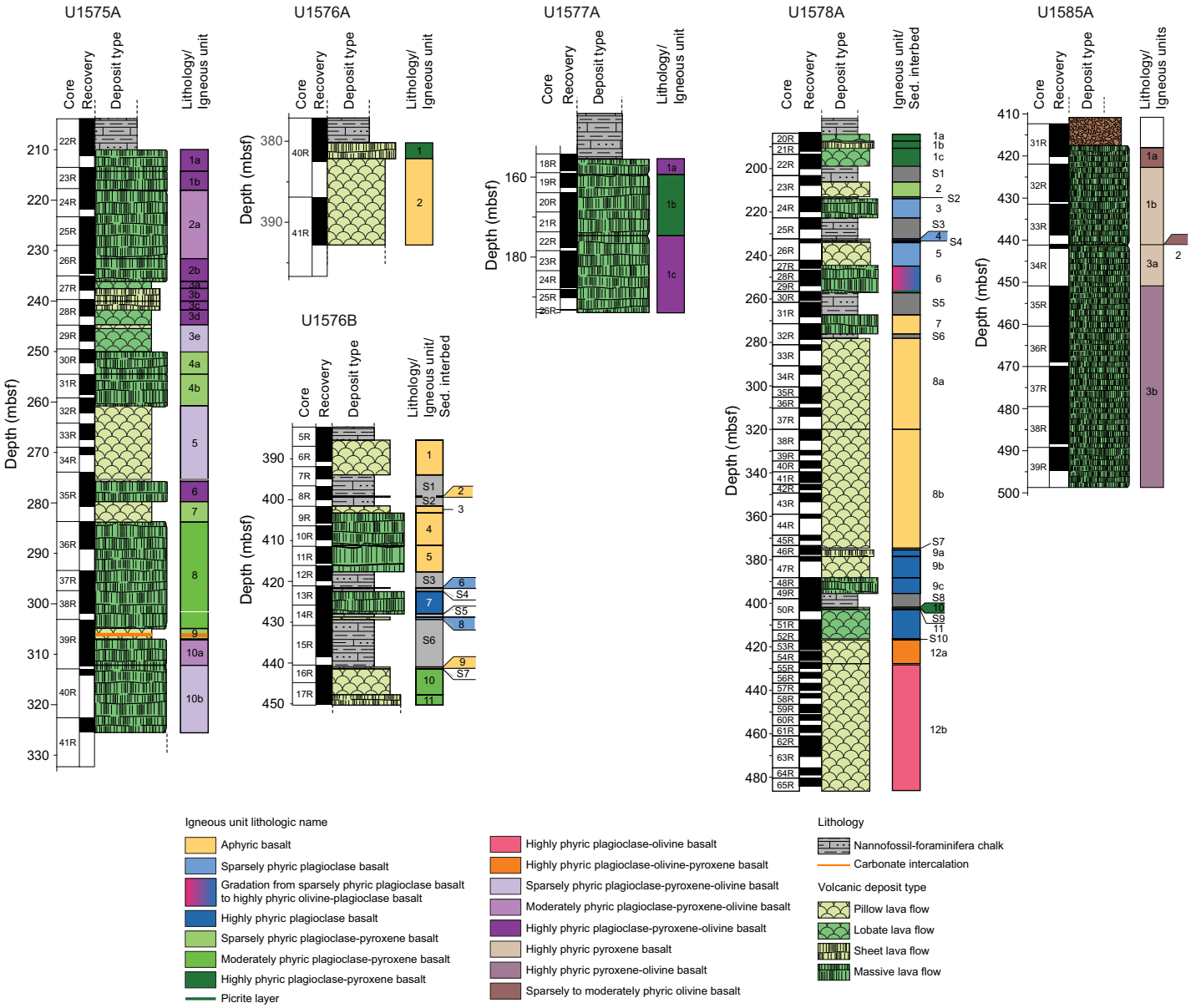


**Figure F3.** Lithostratigraphic summary of igneous rock, Holes U1575A, U1576A, U1576B, U1577A, U1578A, and U1585A.

# 2. Background

Most of the background information included here comes from the proposal that was accepted for Expedition 391 and related proposals and papers by the proposal authors. It is included here as a detailed justification and rationale for Expedition 391.

## 2.1. Hotspot models and geodynamics

Early concepts of hotspots were compelling because they seemed to fit nicely with the new paradigm of plate tectonics. Hotspots were explained as a melting anomaly beneath the lithospheric plates (Wilson, 1963) above a narrow thermal plume arising from the deep mantle (Morgan, 1971, 1972). Eventually, hotspot volcanic chains were widely used as a mantle reference frame (Morgan, 1971, 1972, 1981; Duncan, 1981; Duncan and Clague, 1985; Müller et al., 1993) because the volcanic sources seemed to be fixed within the mantle and thus volcanic chains were interpreted as an indication of absolute plate motion. This view lost favor as studies discovered problems with abso-

lute plate motion models. Some studies showed discrepancies between the Pacific and Indo-Atlantic hotspot reference frames (Stock and Molnar, 1987; Cande et al., 1995; Raymond et al., 2000). Other studies questioned the fixed hotspot hypothesis because numerical models implied perturbations by mantle flow (Steinberger and O'Connell, 1998, 2000; Steinberger, 2000; Steinberger et al., 2004). Paleolatitude data showed significant latitudinal motion of the Hawaiian hotspot (Tarduno and Cottrell, 1997; Tarduno et al., 2003) in contrast with limited motion for the Louisville hotspot (Koppers et al., 2012). Simultaneously, other authors questioned the plume model and the role of plumes in mantle convection (Foulger, 2005, 2007). The result was a shift of consensus from fixed to mobile hotspots. With renewed scrutiny, researchers have found the plume and hotspot hypotheses to be more complicated than was first thought. Although many researchers accept the plume hypothesis, the number, composition, sources, mobility, structure, and geodynamic implications are still debated (e.g., Courtillot et al., 2003; Anderson, 2005; Montelli et al., 2006; Foulger, 2007; Farnetani and Samuel, 2005; French and Romanowicz, 2015; Koppers et al., 2021; Liu and Leng, 2020).

Hotspot volcanic chains are most clearly expressed in the oceans as quasilinear seamount chains, but most are poorly sampled and studied, leaving room for uncertainty and speculation. The Hawaiian-Emperor chain is the archetypal hotspot track. Its apparent age progression is relatively simple (Clague and Dalrymple, 1989) and inspired Wilson (1963) to propose the hotspot hypothesis, followed by the mantle plume hypothesis (Morgan, 1971). Many Pacific seamount chains display a "string of pearls" morphology with largely individual volcanic seamounts, most of which are characterized by relatively flat tops (guyots), in a line recording the motion of the plate relative to the hotspot (e.g., Clague and Dalrymple, 1989; Koppers et al., 2011). This idea is widely accepted and applied to other linear seamount chains. In contrast to many Pacific seamount tracks, Atlantic seamount chains are diffuse and sometimes imply different rates of motion (e.g., O'Connor et al., 1999). Some chains, such as Ninetyeast Ridge and Walvis Ridge, have complex morphologies, containing quasiconical and ridge-like structures, plateaus, multiple tracks, and large offsets, which indicates that their shapes are partly a result of interactions with plate boundaries (e.g., Expedition 324 Scientists, 2010; Sager, 2021; Krishna et al., 2012; O'Connor and Jokat, 2015a, 2015b; Hoernle et al., 2016). In addition, there is evidence that large igneous provinces (LIPs) and mid-ocean ridges can interact over tens of millions of years (Krishna et al., 2012; Sager et al., 2016, 2019, 2021), suggesting that plume and mid-ocean ridge convection may be linked (Whittaker et al., 2015).

## 2.2. Geologic setting

The TGW chain, located in the South Atlantic (Figure **F1**), is one of the most geodynamically complex and significant hotspot tracks. It was one of the first proposed plume tracks (Morgan, 1971, 1972) and is considered to have formed by age-progressive volcanism like Hawaii (O'Connor and Duncan, 1990; O'Connor and le Roex, 1992; Rohde et al., 2013b; O'Connor and Jokat, 2015a, 2015b; Homrighausen et al., 2019). It is one of only three hotspot tracks that connect a continental flood basalt province to active volcanoes (Richards et al., 1989). It is also considered one of only seven primary (probably from the lower mantle) plumes (Courtillot et al., 2003). Furthermore, it is one of several South Atlantic hotspots tied to the edge of the African LLSVP at the base of the lower mantle, a possible plume generation zone (Torsvik et al., 2006; O'Connor et al., 2012; Hoernle et al., 2015; Homrighausen et al., 2018, 2019, 2020). Because of its prominence and ~120 My duration (Rohde et al., 2013b; O'Connor and Jokat, 2015b; Homrighausen et al., 2019), Walvis Ridge is a keystone in the Indo-Atlantic hotspot absolute motion reference frame (e.g., Duncan, 1981; Müller et al., 1993; Doubrovine et al., 2012), but with its geologic complexities and the uncertainty of plumes as fixed mantle markers, the geodynamic implications of the TGW track are unclear. Indeed, some authors posit that the TGW chain was formed by nonhotspot-related volcanism along shear zones and structural weaknesses (Fairhead and Wilson, 2005; Foulger, 2007, 2018). Although many researchers think there is strong evidence that Walvis Ridge was formed by a mantle plume, its complexity contrasts with the simple Hawaiian-Emperor chain. The TGW chain forms a narrow ridge near the continent after a sharp bend forms a plateau (Valdivia Bank) and then splits into two or three seamount chains farther southwest until it reaches a width of 400 km between the active volcanic island groups of Tristan da Cunha and Gough. This region of guy-

ots and ridge-type seamounts is known as the Guyot Province. The two outer seamount tracks end in the active volcanic islands (Figure **F1**). It may be that the TGW track is an example of a different type of mantle plume, emplaced near a ridge during its early history and from more diffuse or multiple upwellings (e.g., O'Connor et al., 2012; Anderson and Natland, 2014; Rohde et al., 2013b; Liu and Leng, 2020). The TGW track also represents the longest known (~70 My) geochemically zoned hotspot, and the onset of zonation occurs just before the morphologic split (Rohde et al., 2013a; Hoernle et al., 2015; Class et al., 2015). Moreover, the Valdivia Bank section of Walvis Ridge displays age-progressive secondary volcanism with a distinct isotopic composition (HIMU, or high time-integrated $^{238}U/^{204}Pb$ type) that lags the original volcanism by ~30 My, implying a secondary plume (Homrighausen et al., 2018, 2019, 2020). For these reasons, knowledge of the TGW track history is important for understanding hotspot geodynamics and volcanism.

### 2.2.1. Evolution of Walvis Ridge: Rio Grande Rise hotspot twins

Walvis Ridge and Rio Grande Rise (Figure **F4**) are considered examples of LIPs formed from a mantle plume located beneath a spreading ridge (Morgan, 1981; O'Connor and Duncan, 1990; Whittaker et al., 2015). While the plume was beneath the Mid-Atlantic Ridge during the Late Cretaceous, eruptions occurred on both the South American and African plates, forming Rio Grande Rise and Walvis Ridge (O'Connor and Duncan, 1990; Rohde et al., 2013b). Although the TGW chain appears as a quasilinear ridge and seamount chain, LIP eruptions formed two oceanic plateaus, Valdivia Bank (400 km × 550 km) and Rio Grande Rise Massif (500 km × 950 km), at ~80–90 Ma (Rohde et al., 2013b; Homrighausen et al., 2019; Sager et al., 2021). The hotspot and the Mid-Atlantic Ridge separated at ~65 Ma, and the hotspot erupted on the African plate thereafter. Consequently, volcanism ceased on the South American plate, whereas linear seamount chains extended southwest from Walvis Ridge. Since these pioneering studies, authors have tried to fit the TGW chain with hotspot models that have a monotonic age progression (Figure **F5**) (Duncan, 1981; O'Connor and le Roex, 1992; Müller et al., 1993; Torsvik et al., 2008; Doubrovine et al., 2012). Such simple hotspot models do a poor job of fitting the complex Walvis Ridge morphology. In response, authors have resorted to models with multiple hotspots (O'Connor and le Roex, 1992), moving hotspots (Doubrovine et al., 2012), hotspot-ridge interaction (O'Connor and Jokat, 2015b), and/or distinct plumelets beneath the Tristan and Gough subtracks (Rohde et al., 2013b)

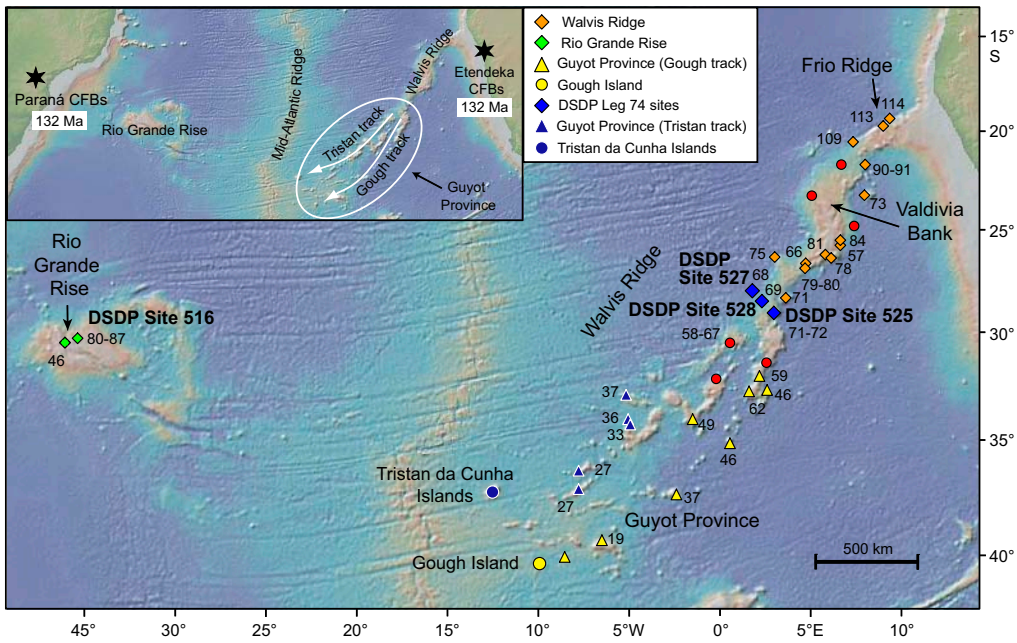


**Figure F4.** Bathymetry of the South Atlantic Ocean, features of Rio Grande Rise and Walvis Ridge, Expedition 391 and 397T drill sites, geochemical trends, and ages. Colored symbols = dredge sites in different provinces (Hoernle et al., 2015). Numbers = radiometric ages in Ma (Rohde et al., 2013b; O'Connor and Jokat, 2015a, 2015b; Homrighausen et al., 2018, 2019). Red dots = cored drill sites. Inset shows the broader region and location of Paraná and Etendeka continental flood basalts (CFBs) and the post–70 Ma split of Walvis Ridge.

to explain TGW track morphologic changes, but no hotspot model is entirely satisfactory. More recent studies, however, show that the TGW chain forms a very good age progression when younger volcanism with a distinct HIMU-type composition is considered separately from the EMI-type basement (Figure **F6**) (Homrighausen et al., 2019). A seismic tomographic study shows a narrow plume conduit (~100 km in diameter) extending to a depth of ~500 km beneath a point

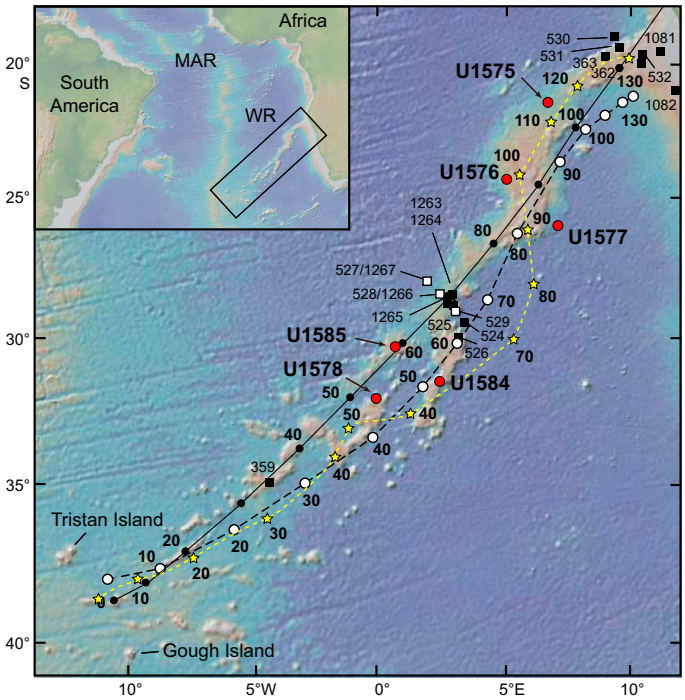


**Figure F5.** Walvis Ridge bathymetry (Smith and Sandwell, 1997), fixed hotspot age models, previous drill sites, and Expedition 391 and 397T drill sites. Solid line = central plume track of O'Connor and le Roex (1992) hotspot model, with black dots every 10 Ma. Dashed line = Torsvik et al. (2008) fixed hotspot model, with white dots every 10 Ma. Dashed line with yellow stars = moving hotspot model of Doubrovine et al. (2012). Small bold numbers = ages (Ma). Squares = DSDP and ODP holes drilled along Walvis Ridge (WR). Red dots = Expedition 391 and 397T cored drill sites. MAR = Mid-Atlantic Ridge.

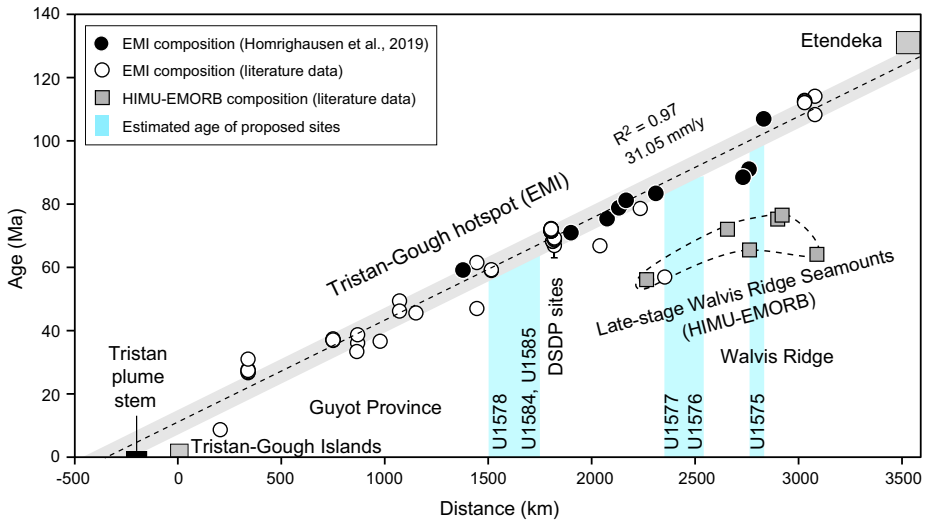


**Figure F6.** Walvis Ridge age progression from radiometrically dated igneous rocks. Samples with EMI composition follow a tight linear trend. Exceptions are samples with HIMU-type composition that yield ages ~30–40 My younger than the underlying basement with an EMI-type geochemical composition. Vertical blue bands = Expedition 391 and 397T cored sites (see Homrighausen et al. [2019] for sources of age data). EMORB = enriched mid-ocean-ridge basalt.

just southwest of the Tristan volcanic island complex (Schlömer et al., 2017). The study did not, however, include the area beneath Gough Island, so this picture is incomplete.

A further problem with the simple plume hypothesis for the older (pre–70 Ma) portion of the hotspot track is the dramatically different morphologies of Rio Grande Rise and the TGW chain. Rio Grande Rise contains two subrounded plateaus and a north–south ridge oriented parallel to the paleo–Mid-Atlantic Ridge axis, whereas Walvis Ridge is a curved linear feature whose morphology changes along its length (Figures **F1**, **F4**). Both the Rio Grande Rise Massif and the southeastern Rio Grande Rise are split by the prominent northwest–southeast oriented Cruzeiro do Sul rift. The current explanation for these troughs is a failed Eocene rifting event (Camboa and Rabinowitz, 1984; Mohriak et al., 2010), which occurred in a midplate setting and has no clear tectonic cause. A similar rift has been observed at Valdivia Bank (Jiménez García, 2017; Sager et al., 2021; Contreras et al., 2022), but its origin is still unknown. Notably, similar rifts are observed at other LIPs, such as the Manihiki Plateau (Danger Island and Suvorov Troughs) (Nakanishi et al., 2015; Pietsch and Uenzelmann-Neben, 2016). In contrast, the TGW chain changes morphology along its length from ridge to plateau to elongated ridges leading to several seamount trails. O'Connor and Jokat (2015a) explained the morphology changes along Walvis Ridge by the interaction of the TGW plume and the Mid-Atlantic Ridge and proposed that the seamounts on the ridge represented the best estimate of the actual TGW hotspot track. Homrighausen et al. (2018, 2019, 2020), however, showed that seamounts atop the original TGW chain form a secondary hotspot track ~30–40 Ma younger than the original TGW edifices. They also point out that extensional faulting appears to postdate substantial erosion of the originally subaerial Walvis Ridge, which places its relationship to TGW plume-ridge interaction into question. After the Mid-Atlantic Ridge drifted away from the TGW hotspot, individual seamount chains of the Guyot Province formed as the plume and Mid-Atlantic Ridge drifted apart (Rohde et al., 2013b; O'Connor and Jokat, 2015b).

When all recently published radiometric ages for Walvis Ridge are considered, they show a wide range of ages (up to 50 My) at a single location and only display a crude progression of ages that becomes older toward Namibia for much of the Late Cretaceous (Figure **F6**) (Rohde et al., 2013b; O'Connor and Jokat, 2015b; Homrighausen et al., 2018, 2019). Nevertheless, Homrighausen et al. (2018, 2019, 2020) showed that TGW chain volcanism forms two distinct geochemical types. The basement, which has undergone extensive erosion and faulting, has an EMI-type composition characterized by unradiogenic $^{206}Pb/^{204}Pb$ isotope ratios. In contrast, the younger seamounts on the EMI basement have a HIMU-type composition characterized by radiogenic $^{206}Pb/^{204}Pb$ isotope ratios. When only the EMI basement volcanics are considered, they show a tight age progression (Figure **F6**) (Homrighausen et al., 2019). The HIMU seamount volcanism shows a similar age progression but is offset by 30–40 My at a given location from the EMI basement lavas (Figure **F6**). The HIMU-type seamounts have been interpreted to reflect the passage of Walvis Ridge over a secondary hotspot ~30–40 My after formation of the Walvis Ridge EMI basement. It has been proposed that the EMI TGW hotspot was derived from the outer margin of the LLSVP, and the secondary HIMU hotspot was derived from an internal step in the LLSVP (Homrighausen et al., 2020). Reconstructions (Figure **F7**) imply that the main edifices of Rio Grande Rise and Valdivia Bank formed together at the Mid-Atlantic Ridge between ~80 and 90 Ma. Few radiometric dates are available from Rio Grande Rise. Tholeiitic basalt samples from Deep Sea Drilling Project (DSDP) Site 516 produced radiometric ages of 80–86 Ma, and a dredged alkali basalt from the edge of the Cruzeiro do Sul rift yielded an age of 46 Ma (Rohde et al., 2013b; O'Connor and Jokat, 2015a). Several authors recognized secondary volcanism in seismic lines and attributed it to a regional tectonic event of unknown cause (Camboa and Rabinowitz, 1984; Mohriak et al., 2010). Although age data thus far define an excellent age progression for Walvis Ridge, the scant age data from Rio Grande Rise and its complexity do not allow us to properly assess whether this volcanism is also age progressive in the direction of plate motion.

### 2.2.2. Did Rio Grande Rise Massif and Valdivia Bank form at a microplate?

Results from a recent study of Rio Grande Rise–Walvis Ridge tectonics based on tectonic fabric in satellite gravity and magnetic data (Sager et al., 2015, 2021; Thoram et al., 2019) reveal tectonic anomalies associated with the formation of the two LIPs. Seafloor fabric (orthogonal fracture zones and ridge fault blocks) is quite regular in most of the South Atlantic, except for the area

between Rio Grande Rise and Walvis Ridge and magnetic Chron 34 (83.7 Ma; anomaly ages from Ogg, 2020) and Chron 30 (66.3 Ma). The prominent magnetic anomaly of Chron 33r appears too early in reconstructions of Walvis Ridge and Rio Grande Rise, implying extra (older) material between the two. Coupled with discordant seafloor fabric, it is postulated that a microplate existed between Rio Grande Rise and Valdivia Bank during the Late Cretaceous (Figure **F8**) (Thoram et al., 2019; Sager et al., 2021). Given reconstructions showing a ring of igneous constructs around the proposed microplate, it is possible that microplate formation affected volcanism in both provinces. The cause is thought to be a reorganization of a long-offset fracture zone during the Late Cretaceous. First located north of Frio Ridge in the northeastern Walvis Ridge, the fracture zone broke apart between approximately 92 and 68 Ma and reformed as multiple fracture zones farther south (Sager et al., 2021).

The microplate hypothesis potentially changes the way we interpret the TGW chain and Rio Grande Rise during their most effusive phase. Rather than developing with a simple age progres-

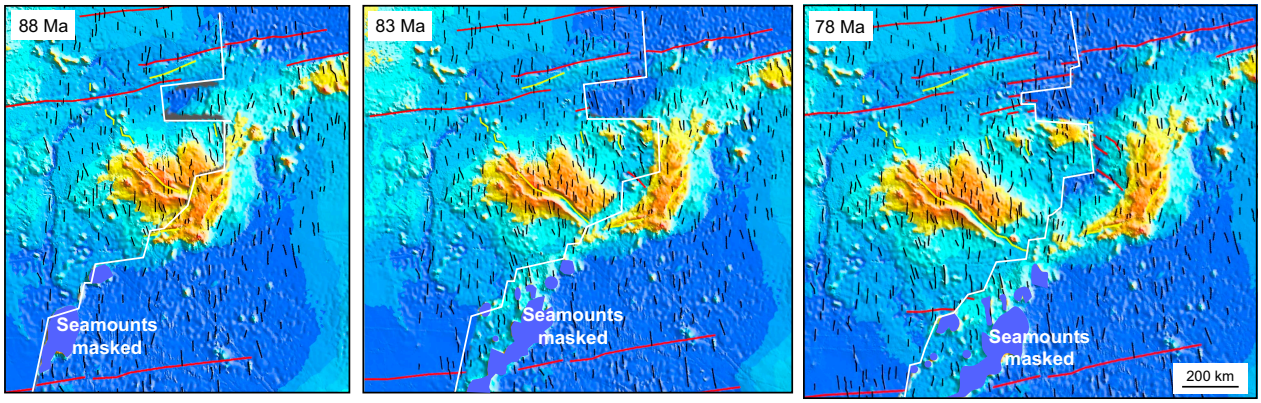


**Figure F7.** Bathymetry reconstruction of Rio Grande Rise and Valdivia Bank at 88, 83, and 78 Ma. At 88 Ma, the main Rio Grande Rise and Valdivia Bank formed at the Mid-Atlantic Ridge. Around 83 Ma, Rio Grande Rise, Valdivia Bank, and part of East Rio Grande Rise formed a volcanic ring surrounding a small basin that may have contained a microplate (Thoram et al., 2019; Sager et al., 2021). White line = location of the Mid-Atlantic Ridge inferred from existing age models (Müller et al., 2008). This reconstruction shows bathymetry by crustal age, so features that postdate crustal formation appear too early. For this reason, guyots younger than the seafloor are masked. (From Sager et al., 2021.)

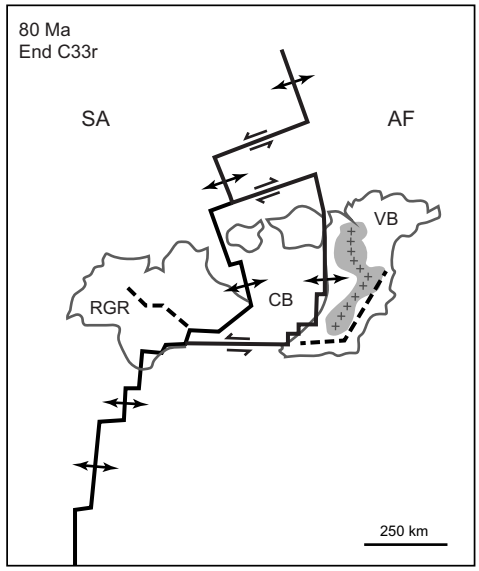


**Figure F8.** Tectonic sketch of the proposed microplate that briefly existed between Rio Grande Rise (RGR) and Valdivia Bank (VB) at 80 Ma (end of Chron 33r). Heavy lines = spreading ridges, arrows = spreading direction, gray lines = outlines of RGR and VB bathymetric highs, gray shaded area = positive magnetic anomaly zone, dashed line = rifts in RGR and VB. SA = South American plate, AF = African plate, CB = Centaurus Basin. (From Sager et al., 2021.)

sion, volcanism may have occurred in multiple places simultaneously: for example, at plate boundaries along the rim of the microplate or along the middle TGW chain where fracture zones created elongated ridges at about the time of the Chron C34 to C30 reorganization. Microplates often rotate (e.g., Schouten et al., 1993; Bird et al., 1998), which could cause misleading tectonic trends for hotspot models. In many other settings, ridge reorganizations, microplates, triple junctions, and LIPs occur together (Tamaki and Larson, 1988; Sager et al., 1999; Sager, 2005; Taylor, 2006; Chandler et al., 2012), implying possible linkages among these processes.

### 2.2.3. Paleolatitude and hotspot motion

Paleomagnetic polar wander is chiefly ascribed to plate motion (e.g., Butler, 1992). Less recognized are contributions from the movement of the spin axis relative to the entire Earth (i.e., TPW) (Gold, 1955; Goldreich and Toomre, 1969) and time-varying nondipole geomagnetic field components (Coupland and Van der Voo, 1980; Livermore et al., 1984; McElhinny et al., 1996). Although nondipole fields are generally believed to be small (<10% of dipole) (Livermore et al., 1984; McElhinny et al., 1996), TPW can be much larger. The maximum principle axis of inertia may even suddenly shift ~90° (inertial interchange TPW), causing the spin axis to follow (Kirschvink et al., 1997). Smaller spin axis shifts and oscillations probably also occur, controlled by convective currents and the viscoelastic relaxation time of the lithosphere and mantle (Creveling et al., 2012; Mitchell et al., 2021).

The difficulty with inferring TPW is that it is hard to define because it requires paleomagnetic data to be compared with an independent geographic reference frame. The hotspot reference frame was widely used as a basis to separate plate motions from TPW; the standard procedure was to subtract plate motion relative to the hotspots (mantle reference frame) from paleomagnetic polar wander (Gordon, 1987; Besse and Courtillot, 2002). The remaining polar drift was interpreted as TPW. When hotspots were considered fixed relative to the mantle, this comparison was simple. Recent research suggesting that hotspots may move relative to one another and to the mantle owing to convection (Steinberger and O'Connell, 1998; Steinberger, 2000; Steinberger et al., 2004) makes the definition of a hotspot reference frame uncertain. Several studies have tried to revive the hotspot reference frame by computing an average hotspot reference frame that minimizes interhotspot drift (O'Neill et al., 2005; Torsvik et al., 2008; Doubrovine et al., 2012).

Even with allowance for moving hotspots, differences occur between the average hotspot reference frame and paleomagnetic polar wander, implying TPW (Torsvik et al., 2008; Doubrovine et al., 2012; Koivisto et al., 2014). Furthermore, these moving hotspot models produce inconsistencies with other kinematic observations related to past ridge-axis positions (Wessel and Müller, 2016) and regional plate motion reorganizations (Seton et al., 2015). A robust mantle reference frame is needed to investigate and understand global surface tectonics and mantle geodynamics. To build such a reference frame, the size, direction, and timing of uniform hotspot drift (caused by TPW) must be firmly established. This requires better understanding of the paleomagnetic records from hotspots.

### 2.2.4. Paleolatitudes from scientific drilling in the Pacific

DSDP and Ocean Drilling Program (ODP) samples from the Emperor Seamounts show an offset from the current hotspot latitude of ~14° to 15° for the oldest edifices (Kono, 1980; Tarduno and Cottrell, 1997; Tarduno et al., 2003). At first, the offset was attributed to TPW (Gordon and Cape, 1981; Gordon, 1982). However, discrepancies and misfits with the hotspot reference frame (e.g., Stock and Molnar, 1987; Cande et al., 1995; Raymond et al., 2000) and models of mantle flow (e.g., Steinberger and O'Connell, 1998, 2000; Steinberger, 2000; Steinberger et al., 2004) favored the idea that hotspots are not fixed in the mantle (Steinberger et al., 2004; Tarduno et al., 2009). Paleomagnetic data from Integrated Ocean Drilling Program Expedition 330 to the Louisville Seamounts showed little motion of the Louisville hotspot in contrast to the large change for the contemporaneous Hawaiian hotspot, implying interhotspot motion consistent with mantle flow models (Koppers et al., 2012). Recently, however, Gordon and others suggested that interpretations of hotspot motion are overblown and that part of the Hawaiian hotspot paleolatitude change resulted from a Cenozoic episode of TPW (Woodworth and Gordon, 2018; Zheng et al., 2018; Wang et al., 2019).

### 2.2.5. Hotspot motion versus true polar wander

Although varying degrees of interhotspot motion are widely accepted, TPW cannot be dismissed. It has a robust theoretical underpinning (Gold, 1955; Goldreich and Toomre, 1969; Gordon, 1987; Creveling et al., 2012) and is supported by independent evidence of shifts in paleolatitude (Kirschvink et al., 1997; Prévot et al., 2000; Doubrovine et al., 2012). The debate about the role of TPW in hotspot latitude shifts continues because of difficulties in defining an absolute reference frame and sparse paleomagnetic data sets. Recent moving hotspot absolute plate motion models show promise in sorting out these phenomena (O'Neill et al., 2005; Torsvik et al., 2008; Doubrovine et al., 2012), but the uncertainties of such models are large because of combined uncertainties of plate motion and mantle flow, especially for times earlier than the Cenozoic, when mantle flow model uncertainties become large (Steinberger, 2000). As noted by Doubrovine et al. (2012), "substantial amounts of TPW at rates varying between ~0.1°/Ma and 1°/Ma" occur in their global moving hotspot model. In fact, TPW is the dominant part of motion between the paleomagnetic axis and hotspots in that model. Thus, it is important to determine the paleolatitude history of primary hotspots for constraints on hotspot motion and TPW. Even when significant paleomagnetic data exist for the same plate (as is the case for Africa), data from the hotspot track itself are critical for deciphering the different processes that contribute to its latitude history.

### 2.2.6. Paleolatitude changes for the Tristan-Gough-Walvis hotspot

There are few paleomagnetic data from the TGW chain, so we must look to continental paleomagnetic data. Such data imply significant paleolatitude changes for the TGW chain over the past 120 My (Figure **F9**) (Torsvik et al., 2008; Doubrovine et al., 2012). Between the mid-Cretaceous and early Cenozoic, there was a rapid southward paleolatitude shift, totaling ~18°–20°, from ~10°–12° north to ~5°–7° south of the current hotspot latitude. This was followed by slow drift northward to the current latitude. These trends are unexpected because they are not predicted by hotspot models. The total ~20° of northward motion implied by Walvis Ridge (Figure **F9**) can be explained by the ~7° southward motion of the hotspot and the ~13° northward motion of the African plate relative to the mantle (Doubrovine et al., 2012). Although this is one model, other moving-hotspot models give similar results (O'Neill et al., 2005; Torsvik et al., 2008), and no mantle flow models predict northward motion of the hotspot as implied by Cenozoic paleomagnetic data. The difference between the absolute plate motion model and observed paleomagnetic data is interpreted as TPW (Doubrovine et al., 2012), which may account for both the rapid southward shift during the Cretaceous and the northward Cenozoic shift (Figure **F9**).

The Cenozoic paleolatitude trend is similar to that expected for TPW rotation that causes a southward paleolatitude shift for the Hawaiian hotspot (as observed) and a northward shift for the TGW chain hotspot. It is true that the amplitude and timing of the shift appear different in the two oceans, but a contributing factor could be averaging: the paleolatitude curve in Figure **F9** is a 20 My running average that smooths and potentially shifts paleolatitude changes, whereas paleolatitude data from Pacific hotspots cover short time intervals. Coring on the TGW track should show a large paleolatitude change (~10°) from the oldest Cretaceous site to the early Cenozoic sites. Moreover, the Cenozoic sites should show a significant departure (~5° or 6°) from the present latitude. Given that well-averaged paleolatitudes from coring have uncertainties of ~5°, the predicted paleolatitude shifts are within the resolution of coring studies (Tarduno et al., 2003; Koppers et al., 2012). It is difficult to know beforehand the ages of the planned drill sites. According to a fixed hotspot model (Figure **F5**) (Torsvik et al., 2008), the guyot sites range ~45 Ma (Site U1578) to 56 Ma (proposed primary Sites TT-4A and GT-4A) and the Valdivia Bank sites range ~80–85 Ma (Sites U1576 and U1577) to 95 Ma (Site U1575). A moving hotspot model (Doubrovine et al., 2012) predicts an age of ~55 Ma for Site U1578 and ~64 Ma for proposed primary Sites TT-4A and GT-4A but shows a greater age span along the axis of Valdivia Bank, from ~85 Ma for Sites U1576 and U1577 and ~110 Ma for Site U1575. Reliable radiometric ages are sparse, but Homrighausen et al. (2019) gave an age of 59 Ma for the southern end of the ridge upon which Site U1578 is located, as well as oldest ages of 81–84 Ma on the southern Valdivia Bank (Sites U1576 and U1577) and ~109 Ma on the northwestern scarp of Frio Ridge (Figure **F6**).

## 2.3. Geochemical setting

### 2.3.1. Geochemistry and isotopic zonation

Increasingly, spatial geochemical zonation, present as subparallel geographically and geochemically distinct domains, is observed along hotspot tracks, including Hawaii, Galápagos, Samoa, Marquesas, Discovery, and TGW (e.g., Hoernle et al. 2000; Werner et al., 2003; Abouchami et al., 2005; Weis et al., 2011; Huang et al., 2011; Rohde et al., 2013a; Hoernle et al., 2015; Schwindrofska et al., 2016; Harrison et al. 2017; Homrighausen et al., 2019). The TGW hotspot track, which includes Walvis Ridge, Guyot Province, and active island groups around Tristan da Cunha and Gough Islands, has been recognized as the longest lived zoned hotspot system, displaying ~70 My of zonation (Rohde et al., 2013a; Hoernle et al., 2015; Homrighausen et al., 2019), compared to

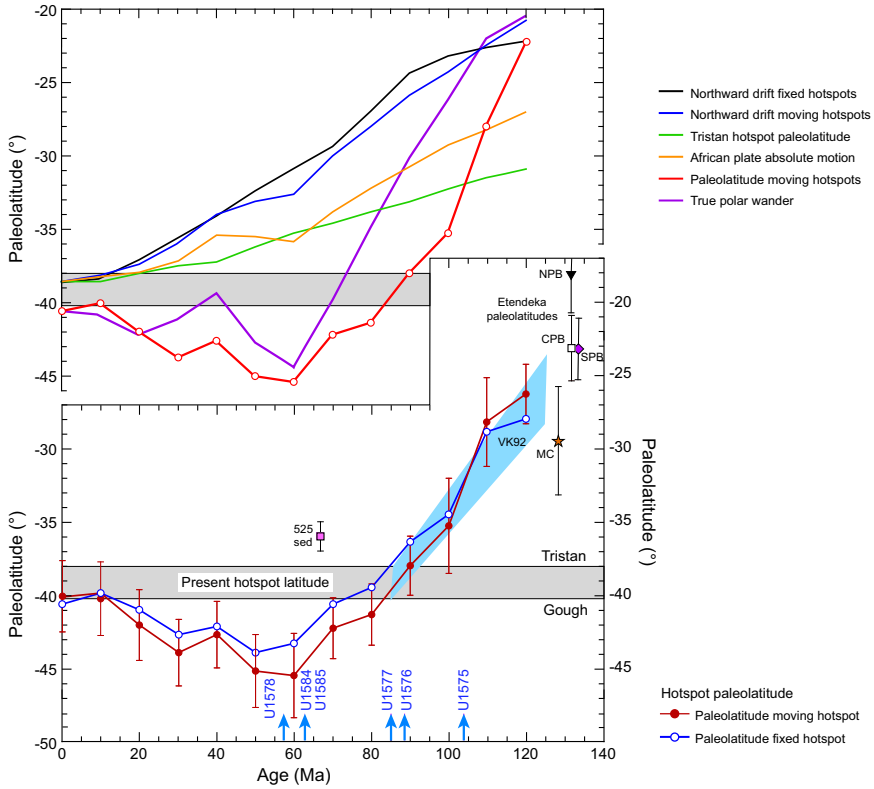


**Figure F9.** Predicted paleolatitude drift of the TGW hotspot, hotspot models, and TPW. Bottom: paleolatitude estimates. Red line with dots = estimated paleolatitudes calculated from the global average African plate apparent polar wander path (Torsvik et al., 2008) based on a plate motion model with moving hotspots (Doubrovine et al., 2012). Thin vertical lines = 95% confidence limits based on paleomagnetic data scatter only. This polar wander path was constructed with a 20 My window length, averaged every 10 Ma. Blue line with circles = same paleolatitude curve for a fixed hotspot model (Torsvik et al., 2008). Pink square = paleolatitude determined for 60–75 Ma sediments (sed) from Site 525 (Chave, 1984). Its departure from the paleolatitude curve may be a result of inclination shallowing that is common for sediments (Verosub, 1977). Black triangle (NPB), open square (CPB), and purple diamond (SPB) = paleolatitudes from the north, central, and south Paraná flood basalts, respectively (Ernesto et al., 1990, 1999). Orange star (MC) = paleolatitude of Messum gabbros in the Etendeka province (Renne et al., 2002). Blue band (VK92) = hotspot drift estimated by Van Fossen and Kent (1992). Blue arrows = estimated ages of proposed drill sites from an age progression model (Homrighausen et al., 2019, 2020). Top: northward drift and TPW. Red line = paleolatitudes estimated from paleomagnetic data (same as lower plot). Black line = northward drift of a seamount with time if formed at the Tristan hotspot location (Schlömer et al., 2017), assuming a fixed hotspot model (Torsvik et al., 2008). Blue line = a moving hotspot model (Doubrovine et al., 2012). Green line = paleolatitudes of the Tristan hotspot from a mantle flow model (Doubrovine et al., 2012), indicating ~7° southward motion in 120 My. Orange line = northward drift of the African plate in the moving hotspot model (Doubrovine et al., 2012). It is less than the fixed hotspot model because the Tristan hotspot is modeled as moving south. Adding the hotspot motion to the moving hotspot model absolute motion equals the total northward motion indicated by the morphology of the TGW chain and the fixed hotspot model. All absolute motion models indicate that the African plate moved nearly monotonically northward, so they do not explain the rapid southward shift in paleolatitudes during the Late Cretaceous or the northward offset of paleolatitudes during the early Cenozoic. The difference between modeled and observed paleolatitudes implies significant TPW (purple curve) (Doubrovine et al., 2012).

possibly 6.5 My for Hawaii (Harrison et al., 2017) and ~20 My for Galápagos (Hoernle et al., 2000; Werner et al., 2003). Between ~115 and 70 Ma and ~85 and 6.5 Ma, the enriched Gough and more depleted Kea components dominated the composition of the TGW and Hawaiian hotspot track, respectively (Portnyagin et al., 2008; Hoernle et al., 2015; Harrison et al., 2017; Homrighausen et al., 2019). Modeling suggests that a zoned hotspot track reflects bilateral zonation of and laminar flow within the plume stem, thus preserving evidence for distinct chemical reservoirs in the source region (e.g., Kerr and Mériaux, 2004; Lohmann et al., 2009; Farnetani and Samuel, 2005; Farnetani et al., 2012). Although most zoned hotspot tracks identified thus far consist of dual distinct chemical domains oriented parallel to the hotspot track, Hoernle et al. (2000) showed that the Galápagos hotspot track displays trilateral zonation and argued for trilateral zonation of the plume but noted that the central geochemical stripe may result from mixing of material from the outer two stripes. Modeling showed that such zonation is possible if the plume samples three distinct geochemical reservoirs at its base (Lohmann et al., 2009). New isotope data from Guyot Province dredge samples (Class et al., 2014, 2015; Sager et al., 2020) identified a possible third, intermediate zone in 3-D Pb isotopic space (Figures **F10**, **F11**), suggesting that the Tristan-Gough hotspot track may be formed by a long-lived, triple-zoned plume. If confirmed by drilling that the triple zonation does not result simply from mixing of the Tristan and Gough domains at their boundary, it would place tight constraints on the possible spatial distribution of components in the plume source (Lohmann et al., 2009). Geochemical zonation has not been found in the older TGW chain (Figure **F11**), leading Hoernle et al. (2015) to suggest that at ~70 Ma the plume source area either began to suck in Tristan-type material from outside the LLSVP margin, due to having exhausted Gough material near the boundary, or the base of the plume moved so that it straddled the boundary between the LLSVP and surrounding ambient mantle. Plume zonation places important constraints on plume dynamics and heterogeneity of the lower mantle at the LLSVP boundaries.

Although dredge data from the TGW chain provide a foundation for identifying the evolution of source zonation and plume-ridge interaction (Rohde et al., 2013a, 2013b; Hoernle et al., 2015; Class et al., 2014, 2015; Homrighausen et al., 2018, 2019, 2020), fundamental questions remain about source geometry, heterogeneity (how many end-members are required to explain the geochemical zonation?), and plume dynamics (O'Connor et al., 2012) that are important to further our understanding of the global spectrum of plume systems. Is zonation of the TGW plume caused by contributions from the LLSVP to one (or more) of the zones? What can this tell us about lower mantle heterogeneity, including LLSVP heterogeneity? Is TGW plume zonation linked to the split into separate chains, as suggested by Rohde et al. (2013b)? What is the role of plume-ridge

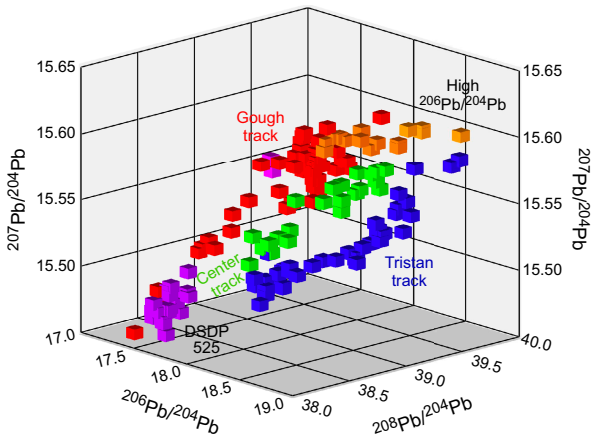


**Figure F10.** 3-D plot of the Pb isotopic composition of TGW hotspot track samples. Spatial geochemical zonation indicates a triple-zoned plume (Class et al., 2015) where new data from dredge samples extend the previously identified dual zonation (Rohde et al., 2013a; Hoernle et al., 2015). Gough track = red, orange, purple; Tristan track = blue; Center track = green. Only high-precision Pb isotope data are shown, and uncertainty is smaller than the symbol size. Samples from the Tristan track with added depleted component with high Hf, high Nd, and low Sr isotopic composition are not shown for clarity (Figure F13). Data sources: Salters and Sachi-Kocher (2010), Rohde et al. (2013a), Hoernle et al. (2015), and Homrighausen et al. (2019). New data on Gough, Tristan, and Inaccessible Islands as well as seamounts sampled by MV1203 and older dredge samples from McNish and RSA by C. Class (unpubl. data).

interaction in both the morphology of the plume trail and the geochemically distinct subparallel trends? To further address these questions, International Ocean Discovery Program (IODP) drill core sampling was required.

Geochemical observations are limited by dredging because we do not know the stratigraphic relationship between different samples in a dredge. Dredges also generally only sample exposed units and thus often don't provide more than a single composition (e.g., same lava flow sampled multiple times) for individual dredge sites, in this case representing only a single point in compositional space. In contrast, sampling of the islands and DSDP Site 527 showed a compositional range (Figure **F12**, black outlines), representing (temporal/downhole) geochemical variability (e.g., Salters and Sachi-Kocher, 2010). The potentially triple-zoned TGW plume can possibly be described by a set of five linear binary mixing arrays in 3-D Pb isotopic space, four of which are defined by arrays of island or drill site samples, namely Gough (forms two arrays), Tristan-Inaccessible, and DSDP Sites 527 and 528 (Figure **F12**). Only new drill cores can provide sufficient data to test whether there is indeed a geochemically distinct Center track (green in Figures **F10**, **F11**, **F12**, **F13**) (Class et al., 2014, 2015) or it simply reflects a mixture of the two outer (Tristan and Gough) geochemical domains, as is also possible for the central track identified in the Galápagos hotspot track (Hoernle et al., 2000; Werner et al., 2003). Furthermore, detailed isotopic studies, including isotopes of Os, rare gases, and other isotope systems, for which appropriate material has not yet been recovered by dredging, could provide evidence that the Center track lavas are derived from a distinct source that cannot be explained by mixing of Tristan and Gough compositional end-members. As noted above, isotope data for the different units at a drill site can form arrays on isotope diagrams, which could help distinguish between the aforementioned possibilities. If the arrays from different sites extend from the Gough to Tristan compositional domain, then mixing of Tristan and Gough is the more likely origin of the central domain. If the central samples form an array that is subparallel to the Tristan and Gough domains or if additional isotope systems show that the central domain has a composition that cannot be explained by mixing of Gough and Tristan compositions, this would argue for a distinct intermediate third domain. Most present models of plume zonation attribute the zonation to sampling of the LLSVP margin by part of the plume base and sampling of the

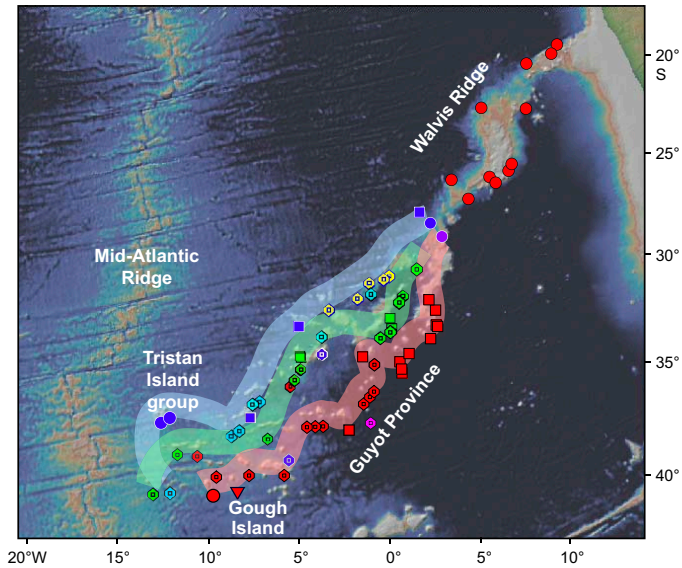


**Figure F11.** Spatial geochemical zonation of the Tristan-Gough hotspot track since 70 Ma. Symbols = locations of dredge samples with high-precision Pb and Sr-Nd-Hf isotope data. Gough track = red, purple; Tristan track = blue, turquoise (depleted), yellow (plume-ridge); Center track = green. The three tracks are highlighted with transparent lines (that do not reflect plate motion) that connect most of the samples of each compositional zone and demonstrate the mostly spatially well separated zones (though there is some overlap). Only the north prong of the TGW chain after the split shows geochemical evidence for interaction of the plume with the Mid-Atlantic Ridge. In contrast, Tristan track samples with depleted compositions can be found over the entire length of the Tristan track. The older Walvis Ridge (red circles) shows no chemical zonation but extends the Gough track signature (Hoernle et al., 2015; Homrighausen et al., 2019). Data sources: Salters and Sachi-Kocher (2010), Rohde et al. (2013a), Hoernle et al. (2015), and Homrighausen et al. (2019).

ambient mantle surrounding the LLSVP. In the simplest case, this should result in two geochemically distinct compositional fields that are not directly related. Evidence for an additional geochemical zone would place this simple model into question, requiring the presence of three or more distinct chemical reservoirs at the plume base (Lohmann et al., 2009). Zonation of the Discovery plume, with distinct zones of Gough-type material in the north and even more enriched and distinct EMI-type material in the south (but no evidence of the Tristan composition), indicates that the model proposed thus far to explain Tristan-Gough zonation may be too simple

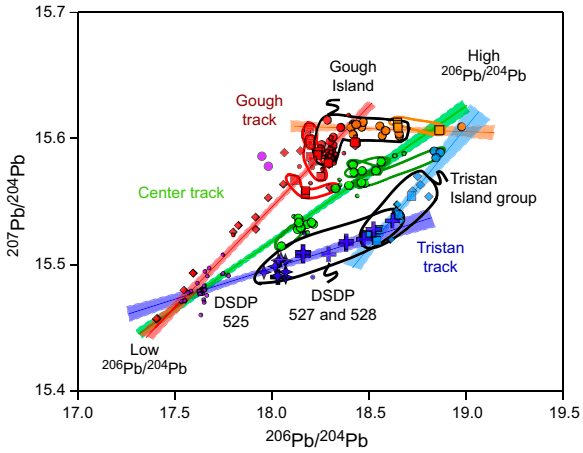


**Figure F12.** Spatial geochemical zonation of the TGW hotspot track in $^{206}Pb/^{204}Pb$ vs. $^{207}Pb/^{204}Pb$ space, justifying the need for drilling. The compositional range is described as linear mixing arrays, and 95% confidence belts are shown. Highlighted are DSDP 527 and 528, Tristan Island group, and Gough Island samples, which show that the islands and drill sites show compositional variability that define mixing arrays. In contrast, dredge locations generally give only one compositional point. The few dredge locations that gave a compositional range are outlined and generally follow mixing arrays. Drilling can help test the triple-zoned plume model; a drill site in each of the three zones should give arrays that are parallel to the proposed mixing arrays. If the Center zone instead shows mixing between the Gough and Tristan end-members (compositional array perpendicular to the Center track), this will support the current model that zoned plumes sample the LLSVP margin and the ambient mantle outside of the LLSVP. Gough track = orange, red, purple; Center track = green, purple; Tristan track = blue, purple; DSDP Site 525A = purple dots. Samples from the Tristan track with added depleted component with high Hf, high Nd, and low Sr isotopic composition are not shown for clarity and not included for confidence belt calculations. All three tracks share the DSDP Site 525 end-member.

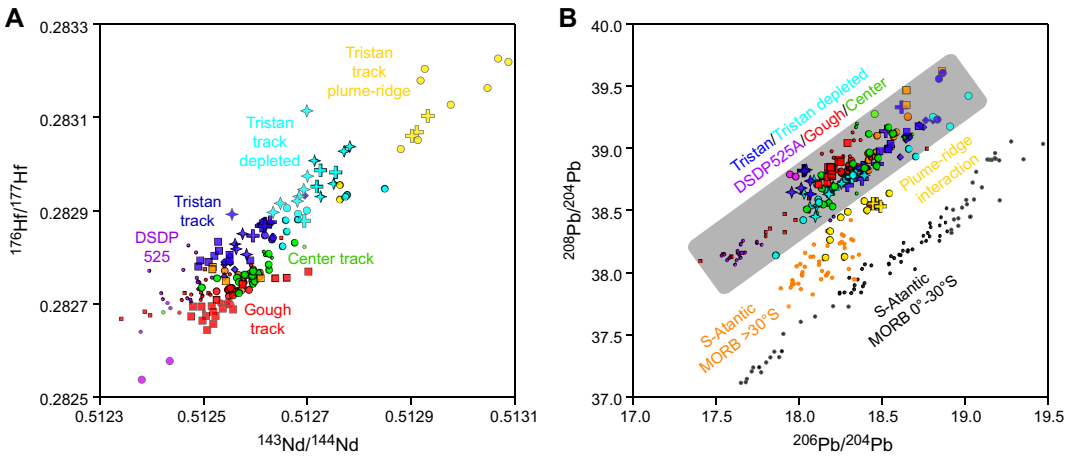


**Figure F13.** Plume-ridge interaction in Walvis Ridge samples. A. Tristan track samples extend to depleted compositions as shown by their high $^{143}Nd/^{144}Nd$ and $^{176}Hf/^{177}Hf$ isotopic compositions. Tristan track samples form a distinct trend from Gough track and Center track samples in this projection. B. All TGW chain samples overlap in $^{206}Pb/^{204}Pb$ vs. $^{208}Pb/^{204}Pb$ isotopic compositions (gray area). Only the most depleted samples (yellow) are displaced toward South Atlantic MORB compositions (orange = MORB 30°–55°S; black = MORB 0°–30°S), providing geochemical evidence for plume-ridge interaction (also MORB-type depleted trace element patterns, not shown here). Data sources: Salters and Sachi-Kocher (2010), Rohde et al. (2013a), Hoernle et al. (2015), and Homrighausen et al. (2019).

(Schwindrofska et al., 2016). If the Gough and Tristan tracks share a common end-member (e.g., low $^{206}Pb/^{204}Pb$), defined by the intersection of three main geographic arrays (Figure **F12**), this could also call into question the simple model that the LLSVP is the global cause for plume zonation because it would imply that all three TGW zones share at least one common end-member. Nevertheless, this could also point to mixing of ambient mantle with three distinct components with radiogenic Pb isotopes from the LLSVP. Being able to define small-scale trends in drill cores (especially if there is deeper penetration of the volcanic sequence, e.g., ≥200 m) can help us sort out the origin of the different components.

The recent identification in Pb isotopic space of zoned plumes containing more than two distinct chemical zones—Galápagos (Hoernle et al., 2000), Samoa (Jackson et al., 2014), and TGW (Class et al., 2014, 2015)—provide an opportunity to further refine our understanding of the dynamic process of source sampling by plumes. For Samoa, the mixing relationship between He and Pb isotopic data is best explained by an LLSVP-sourced, high-$^{3}He/^{4}He$ plume matrix that hosts and mixes with several distinct low $^{3}He/^{4}He$ end-members representing subducted slabs that overlie the LLSVP (Jackson et al., 2014). In the case of the TGW, Discovery, and Shona plumes in the South Atlantic, the Gough composition, the main compositional type in all three hotspots, has been attributed to the LLSVP, whereas the Tristan and Southern Discovery components could reflect a heterogeneous ambient mantle outside of the LLSVP and/or heterogeneity within the LLSVP (consisting of primarily Gough but also more enriched pockets in Southern Discovery). Unlike Samoa, the Gough compositional domain in the hotspot tracks does not generally appear to serve as a matrix for the other components such as Southern Discovery and only in a very limited fashion for the TGW composition. Galápagos (Hoernle et al., 2000; Werner et al., 2003), Samoa (Jackson et al., 2014), Discovery (Schwindrofska et al., 2016), and the unpublished data for the TGW system (Class et al., 2014, 2015) suggested that plume zonation could be considerably more complex than models simply explaining dual chemical tracts. To gain further insights as to whether the TGW hotspot consists primarily of two compositionally and geographically distinct compositional fields or it instead consists of multiple distinct binary mixing arrays, we need samples from stratigraphic sequences at separate locations to see whether each such sequence forms a distinct binary array and/or whether the data fall in distinct compositional fields for a given geographic location or zone. Using additional isotope systems, if appropriate material is recovered, could also shed further light on plume zonation.

O'Connor and Jokat (2015b) proposed that the north side of Walvis Ridge, including the Tristan track of the morphological split, was formed by plume-ridge interaction, whereas the Center track and Gough track were formed by intraplate plume volcanism. Radiogenic isotope signatures of plume-ridge interaction, as inferred from ridge segments close to Tristan and Gough islands and characterized by an intermediate enriched mid-ocean-ridge basalt (MORB)-like composition, are only found in dredge samples from the Tristan track (Figure **F13**, yellow circles) (C. Class, unpubl. data) but not in the rest of Walvis Ridge (Figure **F13**). The drill sites at Valdivia Bank (U1576 and U1577) and Frio Ridge (Site U1575) can further test the model of plume-ridge interaction. Because it samples all three prongs (on- and off-ridge seamounts), the transect of proposed drill sites across the Guyot Province split will clarify the role of plume-ridge interaction and the end-member compositions from the plume contributing to each of the three seamount trails.

Recently, samples from seamounts in the TGW chain, interpreted by O'Connor and Jokat (2015b) to represent the Tristan-Gough plume track, were found to have a distinct composition from the TGW basement (Homrighausen et al., 2018, 2019). The eastern TGW basement generally has a flat top with some graben structures cutting it, and younger seamount volcanoes are located on top of the flat-topped ridge. This deformation has been related to plume-ridge interaction (O'Connor and Jokat, 2015b), but it must postdate the erosion of Walvis Ridge, placing plume-ridge interaction for the cause of this deformation into question. The EMI (Gough and Tristan)-type basement shows an excellent age progression of about 30 mm/y (Figure **F6**). In contrast to the EMI-type compositions of the Walvis Ridge basement, the younger seamounts, which also show an age progression but with ~30 My younger ages on average than the EMI basement at a given location, have compositions extending from end-member St. Helena HIMU to enriched MORB–type mantle (Homrighausen et al., 2018, 2019). An important question that might be addressed

through drilling is to find a stratigraphic sequence with HIMU-type lavas overlying EMI-type lavas or the presence of HIMU dikes/sills within the EMI basement sequence.

Previous scientific drilling has demonstrated that fresh olivine-bearing volcanic rocks and glass are commonly recovered. Olivines and volcanic glass are highly susceptible to alteration by seawater contact, and thus dredging rarely retrieves such samples, in particular fresh olivine. Fresh glass can provide the liquid composition and preserve accurate abundances of volatile elements, such as $H_2O$, S, F, and Cl. Fresh olivines can be used for a variety of analytical purposes, including analyses of He isotopes to test for high $^3He/^4He$ and thus a lower mantle origin of the material, and to constrain further the degassing history of the Earth (Class and Goldstein, 2005; Tolstikhin and Hofmann, 2005; Jackson and Carlson, 2011). Thus far, high $^3He/^4He$ ratios above MORB values (>10 R/Ra) have not been found along the submarine Tristan-Gough hotspot track. In contrast to the other major plumes that show bilateral zonation (Hawaii, Galápagos, and Samoa), no high $^3He/^4He$ signature has been identified for the TGW chain. High $^3He/^4He$ isotope ratios, however, have been found in samples with Gough-type Sr-Nd-Pb isotopic compositions where the Discovery and Shona hotspots are interacting with the Mid-Atlantic Ridge (Sarda et al., 2000). If high He isotopic ratios are found in olivines from drill samples along the TGW hotspot track, they could help unravel which components may be derived from the LLSVP. Olivine can also provide important information about the contents of primitive (early and deeply trapped) volatile elements in melt inclusions and of the composition of primitive and, in some cases, possibly primary melts. They can be used to determine O isotopes to evaluate the involvement of continental material in the source of the magmas, which has been postulated for the EMI signature found in Walvis Ridge lavas. Finally, olivine chemistry can help determine the source lithology, constraining the relative role of pyroxenite versus peridotite in the source of oceanic basalts. This will allow for the assessment of the role of recycled oceanic crust in plume sources and thus provide insights into the geodynamic evolution of Earth's mantle (Sobolev et al., 2005).

It has been proposed that Valdivia Bank and Rio Grande Rise Massif are continental fragments (van der Linden, 1980; Santos et al., 2019). Continental rocks and zircons have been found in other large volcanic provinces, such as Kerguelen Plateau and Broken Ridge (Frey et al., 2002; Ingle et al., 2002), Iceland (Torsvik et al., 2015), and Mauritius (Torsvik et al., 2013). This relationship is uncertain but may reflect the transport of continental slivers into ocean basins during continental rifting (Torsvik et al., 2015). Although gravity fabric within Valdivia Bank implies that its formation is related to the Mid-Atlantic Ridge (Sager et al., 2021), the continental fragment hypothesis can be tested by coring Valdivia Bank to see if lavas show geochemical signals of continental lithosphere assimilation during fractional crystallization.

During Expedition 391, we drilled the Center track to confirm or dismiss the triple-zoned plume model versus a mixed center zone model (Site U1578). Core samples from Valdivia Bank (Sites U1576 and U1577) and Frio Ridge (Site U1575) will test the lack of zonation in the older Walvis Ridge and a possible continental fragment at Valdivia Bank. All sites can potentially provide samples with which we can test the role of lower mantle as the source of the various components, as well as the geochemical fingerprints of plume-ridge interactions. In addition, the cores will be used to test for temporal changes in composition during the formation of the TGW hotspot track, whether they are on the scale of a single hole or whether they occur during the longer term history of the hotspot. Finally, detailed major and trace element data combined with isotope geochemistry can be used to evaluate magma system dynamics during the growth of individual volcanic structures in the Guyot Province and the eastern Walvis Ridge, and volcanological studies can be used to evaluate the detailed growth of parts of these structures through time and magma-water interactions.

## 2.4. Prior drilling results from Walvis Ridge

A small number of sites were drilled on Walvis Ridge, and most only cored the sedimentary section. During DSDP Leg 39, Site 359 was drilled atop one of the Walvis Ridge Guyot Province seamounts (The Shipboard Scientific Party, 1977), and during DSDP Leg 40, Sites 362 and 363 were cored on Frio Ridge near the continental margin (The Shipboard Scientific Party, 1978). Coring at Site 359 penetrated only 107 meters below seafloor (mbsf) and ended in Eocene volcaniclastic

sediments and breccia (The Shipboard Scientific Party, 1977), whereas coring at Sites 362 and 363 penetrated 1081 and 715 mbsf, respectively, and ended in Eocene and Aptian limestone, respectively.

During DSDP Leg 74, five sites (525–529) were drilled across Walvis Ridge between 2° and 3°E. All sites recovered Cenozoic to Late Cretaceous carbonate sediments, and three penetrated into igneous crust (Site 525 = 103 m; Site 527 = 43 m; Site 528 = 80 m) (Moore et al., 1984). At these three sites, basement recovery was high (average = 62%), and basalt flows with intercalated sediments were recovered. Radiometric dates at the sites range 68–72 Ma, with one exception that was too young (Rohde et al., 2013b; O'Connor and Jokat, 2015b). During DSDP Leg 75, Sites 530 and 532 were drilled on or near Frio Ridge, not far from the continental margin (Shipboard Scientific Party, 1984a). Coring at Site 530, which is located in the Angola Basin immediately north of Frio Ridge, penetrated 1121 m of the sedimentary section, recovering Late Albian sediments atop basalt flows (Shipboard Scientific Party, 1984a). Coring at Site 532, located atop Frio Ridge at 10.5°E, penetrated 291 m of sediments, the oldest of which is Miocene (Shipboard Scientific Party, 1984a). ODP Leg 208 revisited the Leg 74 transect but cored only the sedimentary section for paleoceanographic studies (Sites 1262–1267) (Shipboard Scientific Party, 2004).

Away from the continental margin, most cored sediments are open ocean carbonates. These rest atop shallow-water carbonate sediments and basalt at the base of the section. Both Legs 74 and 208 recovered Cenozoic nannofossil or foraminifera ooze grading to ooze and chalk at 200–300 mbsf (The Shipboard Scientific Party, 1978; Shipboard Scientific Party, 2004). This sedimentary section is often 300–500 m thick, ranging from Paleocene–Eocene to Neogene. Distinct basal sediments atop igneous basement have only been cored at a few sites; volcanic breccia were recovered at Site 359 (The Shipboard Scientific Party, 1977), and volcanogenic turbidites and carbonate sand were recovered at Sites 526, 528, and 529 (Moore et al., 1984). Cores from Sites 359 and 526, which are both located on guyot tops, suggest the possibility of volcaniclastic sections on seamount summits. At Site 359, shipboard scientists conjectured a volcaniclastic layer ~40 m thick based on a single core and a poor-quality seismic profile (The Shipboard Scientific Party, 1977). At Site 526, coring penetrated 114 m of Eocene carbonate sands and sandstone that contain 20%–40% volcanic debris (Shipboard Scientific Party, 1984b). Summarizing these prior results, drilling on low-slope seamount flanks should encounter a thin cover of open ocean calcareous ooze and chalk overlying basalt flows. On seamount summits, open-ocean carbonates may be underlain by a basal layer of shallow water carbonates and volcaniclastics.

# 3. Site survey data and site selection

## 3.1. Site selection

The proposal for Expedition 391 was based initially on four modern multichannel seismic profiles collected by German scientists on the research vessels (R/Vs) *Meteor* and *Polarstern*. This data paucity is a result of years of underfunding of seismic investigations in the Southern Ocean. Nevertheless, we were lucky to have these data. Without them, the Walvis Ridge proposal would not have passed evaluation by the Environmental Protection and Safety Panel (EPSP). Although the initial lines had no seismic cross-lines, which are normally done for IODP site surveys, sites were approved on the recognition that seamount flanks have a relatively simple structure, with gently sloping flanks consisting of lava flows covered with a thin layer of sediment. It is possible to infer the flank slopes and direction, and there are no known safety hazards. The primary sites proposed from these initial data were Sites CT-4A, GT-4A, TT-1A, VB-1B, VB-4B, and FR-1B. These six primary sites and an additional eight alternate sites were approved at the September 2018 EPSP meeting.

Subsequently, a site survey proposal was funded by the US National Science Foundation to collect seismic data over Walvis Ridge. This survey (R/V *Thomas G. Thompson* Cruise TN373) was carried out in late 2019. New seismic lines were run across the three previously targeted guyots and Valdivia Bank. These lines also crossed most of the previously proposed sites. An additional 14 new sites were proposed and accepted by the EPSP at the February 2020 meeting. Three of the

previously approved sites were replaced with new sites. Proposed Site TT-4A, on the lower flank of the TT guyot, replaced proposed Site TT-1A because of the latter's proximity to a summit cone, revealed by the new seismic data, that may represent later volcanism. Proposed Site VB-12A, on the east flank of Valdivia Bank, replaced proposed Site VB-1B to provide a site on the east flank of the plateau. Proposed Site VB-14A replaced proposed Site VB-4B on the west flank of Valdivia Bank. The new seismic line shows rough basement and diffractions near the old site that may represent a fault zone. The new site is upslope on basement that appears less fractured. Aside from the 6 primary sites, the remaining 22 sites were retained as alternates so that if problems arose at a primary site, there would be alternates nearby.

Of the four sites cored on Expedition 391, two were alternate sites. As planned, Site U1575 was cored at proposed primary Site FR-1B and Site U1576 was cored at proposed primary Site VB-14A. Owing to severe time constraints in the revised plan, Site U1577 was cored at alternate Site VB-13A and Site U1578 was cored at alternate Site CT-5A. In both cases, the alternate was chosen because it had less sediment cover, which meant less time was devoted to coring sediments. Limited time also characterized the drilling done during Expedition 397T, so two sites were chosen for shallow depths and thin sedimentary cover. For Site U1584, a new proposed site (GT-6A) was picked near the previously proposed Site GT-4A, about 1 km farther upslope where sediment thickness was about half as much. Although alternate Site TT-3A was initially targeted for Expedition 397T, instead, the original Expedition 391 primary Site TT-4A was drilled as Site U1585.

## 3.2. Seismic data from the *Meteor* and *Polarstern* cruises

The four initial seismic lines are GeoB01-25, GeoB01-29, AWI-20060650, and AWI-20060660. The GeoB profiles were collected from *Meteor* during Cruise 49 Leg 1, which was completed in 2001. Seismic data collected during this cruise were used as site survey data for ODP Leg 208. The two AWI profiles were obtained from *Polarstern* during Expedition ANT-XXIII Leg 5 in 2006. Both cruises used GPS for positioning. The *Polarstern* cruise collected bathymetry data with a Krupp-Atlas Hydrosweep multibeam echosounder. The multibeam on *Meteor* was not working at the time of the survey.

The *Meteor* seismic data were collected with a 48-channel streamer, 600 m in length, which was kept at the desired depth by 10 DigiCourse depth controllers (birds). The source had three components: two generator-injector (GI) air guns and a water gun. The GI guns had generator and injector volumes of 0.41 L (a reduced-volume source) and 1.7 L and were towed at a depth of 1.4 m. The water gun volume was 0.16 L, and it was towed at a 0.5 m depth. Shots were fired at ~10 s intervals, producing shot intervals of ~30–35 m, but the GI guns were alternated.

The *Polarstern* seismic data were collected as a part of a larger effort that included seismic refraction. The seismic source was therefore large: four air guns with 8.5 L volume operated at 190 bar pressure. The streamer had a total length of 800 m, with an active section 600 m in length, containing 96 channels with 6.25 m hydrophone group spacing. The shooting interval was 15 s, producing shot intervals of ~35 m. The streamer was towed at a depth of 10 m, whereas the air guns were towed at a depth of 5 m.

The processing of the seismic data from these two cruises was as follows. As a first step, each profile was binned to a common midpoint (CMP) interval of 15 m, resulting in a fold of up to 14 and 18 in GeoB and AWI lines, respectively. The sampling rate of GeoB profiles was reduced to 0.5 ms to match the frequency content of the source signal (20–250 Hz). After removing corrupt traces/channels and adding a recording delay of up to 5 s, a 2-D spike removal within individual channels was performed. Data were then corrected for normal moveout (NMO) with a velocity of 1500 m/s. A static correction was applied to eliminate wave motion effects, and spike removal within shot gathers was performed before stacking. CMP stacked data then underwent frequency filtering: a Butterworth filter of 10/25/550/860 Hz and an adjustable notch filter around 47/49/51/53 Hz were applied. Trace interpolation was used to fill missing CMP locations. White noise reduction preceded the final step, which was finite difference time migration (1500 m/s, 1 ms tau step, and a filtered 45°–65° solution). Processing of AWI lines followed a similar sequence. Data manipulation included an initial debias step. Static corrections were not performed. Rather

than frequency filtering, an F-K filter was applied to CMP-stacked data to remove noise stripes within the signal frequency range. Because of the lower data sampling rate, time migration was carried out with an 8 tau step.

### 3.3. Site survey data from the *Thomas G. Thompson* cruise

New site survey data were collected during *Thomas G. Thompson* Cruise TN373 in November–December 2019. A total of ~3015 km of 2-D multichannel seismic profiles were collected with the Scripps Institution of Oceanography multichannel seismic system, which consists of a 96-channel Geometrics GeoEel streamer and two Sercel 45–105 $in^3$ (0.16–0.37 L) GI air guns as a source. Swath bathymetry data were obtained with a 30 kHz Kongsberg EM302 multibeam system. Sub-bottom profiles were recorded with a Knudsen Model 3260 CHIRP sonar operating at 3.5 kHz frequency.

The multichannel system was towed at a speed of 4.5–5.0 kt (8.3–9.3 km/h), and shots were fired on distance at 25 m intervals. Because the GeoEel streamer has a group spacing of 6.25 m, this speed provided 12-fold coverage, with a CMP spacing of 3.125 m. Data were digitized at an interval of 1 ms and recorded in SEGD format shot files. The seismic streamer was towed at a depth of 4 m, and depth was maintained by four birds. Electronic compasses in the birds were used to calculate the geometry and position of the streamer so that accurate CMP positions could be calculated. The source air guns were towed at a depth of 3 m.

Processing was done with GeoEast software from BGP. Preprocessing included removing duplicate shot records, fixing incorrect shot locations, and removing malfunctioning receiver records. For statics correction, the source delay was fixed by adding a constant 50 m shift to the data. Swell, linear, and wild noise attenuation were applied to lessen swell, linear, and high-amplitude noise, respectively. Deghosting was done to reduce the signal reflected from the ocean surface. For debubbling, a matching filter was determined from the source wavelet, and this signal was removed from the data. Surface multiples were predicted and attenuated using the SRME module in GeoEast. Root mean square velocity profiles were determined with semblance analysis, typically done every 300 CMP but sometimes more often in areas with complex structure. Prior to stacking, NMO was removed along with stretch muting and 8–200 Hz bandpass filtering. For poststack migration, root mean square velocities were converted to interval velocity and finite-difference migration was carried out in the x-t domain.

## 4. Scientific objectives

Expedition 391 addresses the geodynamic implications of the TGW hotspot track, the most prominent in the Atlantic, to improve our understanding of the global spectrum of hotspot volcanism. Primary questions include the following:

- Is Walvis Ridge split into two or three geochemically distinct seamount chains, and is isotopic zonation consistent with involvement of two, as proposed for bilaterally zoned Pacific hotspots, or three distinct plume sources at the LLSVP edge?
- Is the chain strictly age progressive, or were multiple plume pulses, microplates, or continental fragments involved?
- What do potentially large shifts in paleolatitude reveal about the fixity and geodynamics of the hotspot?

The R/V *JOIDES Resolution* cored sediments and basaltic lava flows at six sites, coring ~100 m of lava flows at five sites (U1575–U1577, U1584, and U1585) and ~300 m at one site (U1578). Basalt samples will be analyzed to document the geochemical and isotopic evolution of the TGW hotspot, testing the hypothesis of geochemical division into two or three distinct geographic geochemical zones beginning at ~70 Ma. Research on samples from Sites U1578, U1584, and U1585 will test whether a third geochemical reservoir was involved in the formation of the younger hotspot track. High-precision geochronology from igneous samples will test models of ridge-hotspot interaction, including a microplate model; examine the duration of volcanism at individ-

ual sites; and further document the age progression. Paleomagnetic measurements on igneous samples will constrain paleolatitude changes of the hotspot track, allowing for more rigorous testing of models of hotspot motion and TPW.

## 4.1. Scientific questions and answer strategy

### 4.1.1. What is the basement age progression at Valdivia Bank?

Many hotspot models assume that Valdivia Bank is an age-progressive segment of Walvis Ridge that becomes younger to the south (e.g., Doubrovine et al., 2012). Others suggest that this edifice formed along the Mid-Atlantic Ridge crest (O'Connor and Jokat, 2015b), perhaps because of interaction with a microplate (Thoram et al., 2019; Sager et al., 2021), which implies that the entire edifice is nearly the same age. Although there is considerable overlap in ages, when the samples are divided based on geochemistry the EMI- and HIMU-type samples form distinct age-progressive trends, suggesting that some of the complications may result from late-stage volcanism covering much of the older Valdivia Bank structure (Homrighausen et al., 2018, 2019, 2020). High-precision geochronology data will test whether there is an age progression in the basement lavas along Valdivia Bank, as expected from the plume model, or whether it formed synchronously over a large area, as implied by the plume-ridge or microplate models. High-precision geochemical data will elucidate the genetic relationship between Valdivia Bank, Rio Grande Rise, and the Mid-Atlantic Ridge.

### 4.1.2. Does Valdivia Bank contain a continental fragment?

Although no longer widely accepted, it has been proposed that Valdivia Bank is a continental fragment (van der Linden, 1980). Evidence of continental material has been found in other oceanic plateaus: Kerguelen Plateau (Frey et al., 2002; Ingle et al., 2002), Mauritius (Torsvik et al., 2013), and Iceland (Torsvik et al., 2015). Furthermore, the same has been suggested for Rio Grande Rise (Santos et al., 2019), so the idea cannot yet be dismissed. Coring on Valdivia Bank can help test this idea, either through direct drilling of continental rocks or by showing continental crustal contamination in the geochemistry of the recovered rocks or as xenocrysts (e.g., quartz or zircon) or xenoliths of continental crust. If continental material is found, it will indicate that the continental fragment hypothesis is correct, although lack of such evidence is unlikely to disprove the hypothesis because it can be argued that such evidence was simply missed by limited coring.

### 4.1.3. Is Valdivia Bank a product of ridge volcanism?

Recent magnetic studies of Shatsky Rise found linear magnetic anomalies covering the entire plateau, leading to the conclusion that the plateau was formed by seafloor spreading (Huang et al., 2018; Sager et al., 2019). Geochemical studies indicated that Shatsky Rise rocks have compositions of enriched MORB (Sano et al., 2012) and formed with higher percentages (15%–23%) of partial melt than MORB (Husen et al., 2013; Heydolph et al., 2014). Plate reconstructions imply that Ontong Java Plateau also formed at or near a spreading ridge (Mahoney and Spencer, 1991; Taylor, 2006) with high degrees of partial melting (30%) (Fitton and Godard, 2004). Magnetic anomalies over Valdivia Bank imply that it also formed by spreading at the Mid-Atlantic Ridge (Thoram et al., 2019; Sager et al., 2021). Evidence for the involvement of MORB in the EMI-type basement lavas, however, is not obvious (Figure **F13**). Thus, geochemical studies of Valdivia Bank lavas can provide improved knowledge of the process by which oceanic plateaus form in conjunction with spreading ridges. Olivines can be used as geothermometers to infer the temperature of melting. Major and trace elements can be used to infer percentages of partial melting involved in forming the basalts.

### 4.1.4. Does Walvis Ridge split into three distinct isotopic signatures?

Studies of isotope ratios show that Walvis Ridge splits into two distinct isotopic signatures near the location where the chain splits into two or three separate seamount chains, at an age of ~65 Ma (Rohde et al., 2013a; Hoernle et al., 2015). Preliminary isotopic studies suggest that the middle seamount chain may have a different signature and that the younger part of the TGW hotspot track possibly displays three distinct geochemical zones (Class et al., 2015). Because isotopic zoning is thought to arise from heterogeneities at the base of a mantle plume (Farnetani and Samuel, 2005; Farnetani and Hofmann, 2009; Farnetani et al., 2012; Lohmann et al., 2009), perhaps at the

LLSVP edge (Rohde et al., 2013a; Hoernle et al., 2015; Schwindrofska et al., 2016), the answer to this question has important implications for mantle geodynamics.

#### 4.1.5. Is the isotopic split related to the morphological split into separate seamount chains?

The northernmost seamount chain (Tristan track) appears to have formed by hotspot interaction with the Mid-Atlantic Ridge, whereas the other one or two seamount chains (Center track and Gough track) formed from one or more hotspots beneath the African plate (O'Connor and Jokat, 2015a). Can the isotopic differences be explained by on-ridge versus off-ridge formation? This question can be answered by comparing geochemical and isotopic data from cored igneous rocks on the Tristan track to samples from the possible Center and Gough tracks.

#### 4.1.6. What is the paleolatitude motion of the hotspot?

Basaltic rocks are excellent magnetic field recorders and have been used to measure the paleolatitude of other hotspots: Hawaii (Tarduno et al., 2003) and Louisville (Koppers et al., 2012). Coring targeted Walvis Ridge igneous basement with the objective of collecting enough samples to calculate a precise paleolatitude for the mid-Late Cretaceous (Valdivia Bank; ~84–103 Ma) and Late Cretaceous to early Cenozoic (guyots; 55–65 Ma). In addition, coring penetrated a sedimentary section that may contain lithified carbonate sediments that can also be used to estimate paleolatitude. These paleolatitude data can record changes that can be compared with geodynamic models of hotspot motion and TPW.

### 4.2. Drilling and coring strategy

The plan for Expeditions 391 and 397T included coring at six primary sites on Walvis Ridge in two groups of three. Sites U1575–U1577 cross Valdivia Bank from west to east and north to south (Figure **F1**) to test age and formation models for that oceanic plateau. The general approach was to drill as much igneous rock as possible in the time allowed. The Guyot Province sites (U1578, U1584, and U1585) form a transect across three seamount chains that define the morphologic split of the TGW track (Figure **F1**). These sites are positioned to record differences in geochemical and isotopic characteristics from the seamount sources.

The plan was to use the rotary core barrel (RCB) system at each site to maximize the time spent coring igneous rock. This system is designed for coring hard formations, so it often does a poor job of coring poorly lithified sediments. To obtain minimally disturbed sediments, cores are usually obtained with the advanced piston corer (APC) and extended core barrel (XCB) systems, but they require a different bit assembly. Typically, use of the RCB system results in moderate to severe disturbance of unlithified carbonate oozes. In contrast, it often produces good samples from more lithified chalk and limestone.

Initially, four proposed sites were planned to be single-bit holes (VB-12A, VB-14A, TT-4A, and GT-4A), meaning that coring proceeds into basement until the bit fails or allotted time expires. From past drilling of seamount lavas, it was estimated that this would penetrate ~80–100 m into igneous rock. Three of the four sites drilled during Expedition 391 and both sites drilled during Expedition 397T were single-bit holes. Penetration was less than expected at Site U1577 because massive lava flows encountered led to slow penetration rates coupled with reduced time for operations. Penetration at Site U1584 was also less than planned because indurated volcaniclastics were encountered, so time was saved for future operations by terminating drilling early. Two proposed sites were planned to establish two-bit holes (FR-1B and CT-4A), meaning that the hole would be cored first with one bit and that bit replaced when it wears out. Owing to lack of time, only one two-bit hole (Site U1578) was drilled.

Changing the bit for drilling a two-bit hole requires raising and taking apart the drill string, which requires ~8 h, depending on water depth. After the bit is replaced on the bottom-hole assembly (BHA), it is lowered to the seafloor by reassembling the drill string, which takes about the same amount of time as raising it. Hole reentry is possible with a reentry cone on the seafloor. The cone is located with the aid of sonar and a subsea camera, and the ship's crew positions the ship above the cone so that the drill string can be lowered into the hole. Reentry was accomplished using a

free-fall funnel as the seafloor cone because this device is usually the most economical in terms of time. This funnel is assembled around the drill string and then dropped to the seafloor.

### 4.3. Wireline logging strategy

The wireline logging plan for Expedition 391 aimed to provide continuous stratigraphic coverage of in situ formation properties at all proposed sites. Two tool string configurations were planned for each site. Unfortunately, the logging plan was a casualty of severe time limitations caused by lost time addressing the COVID-19 outbreak on board *JOIDES Resolution*. All available operations time during Expedition 397T was directed toward coring.

## 5. Site summaries

### 5.1. Site U1575

#### 5.1.1. Background and objectives

Site U1575 (proposed Site FR-1B) is located within a low saddle on the northeastern end of Walvis Ridge between the higher Frio Ridge (near the continental margin) and Valdivia Bank, a large ocean plateau edifice (Figure **F1**). Its location is on Seismic Line GeoB-029 where sediments are relatively thin and the basement reflector is clear (Figures **F14**, **F15**). The drill site was chosen as the eastern (older) end of the Expedition 391 transect because it represented an opportunity to sample a part of the ridge that cannot be sampled by dredging due to sediment cover. It also represents the hotspot trail shortly after it passed from the African continental margin to oceanic crust. Trace element and isotopic geochemistry can provide insights into the transition from the plume head to plume tail stage of hotspots, specifically whether both high-$TiO_2$ (Gough-type) and

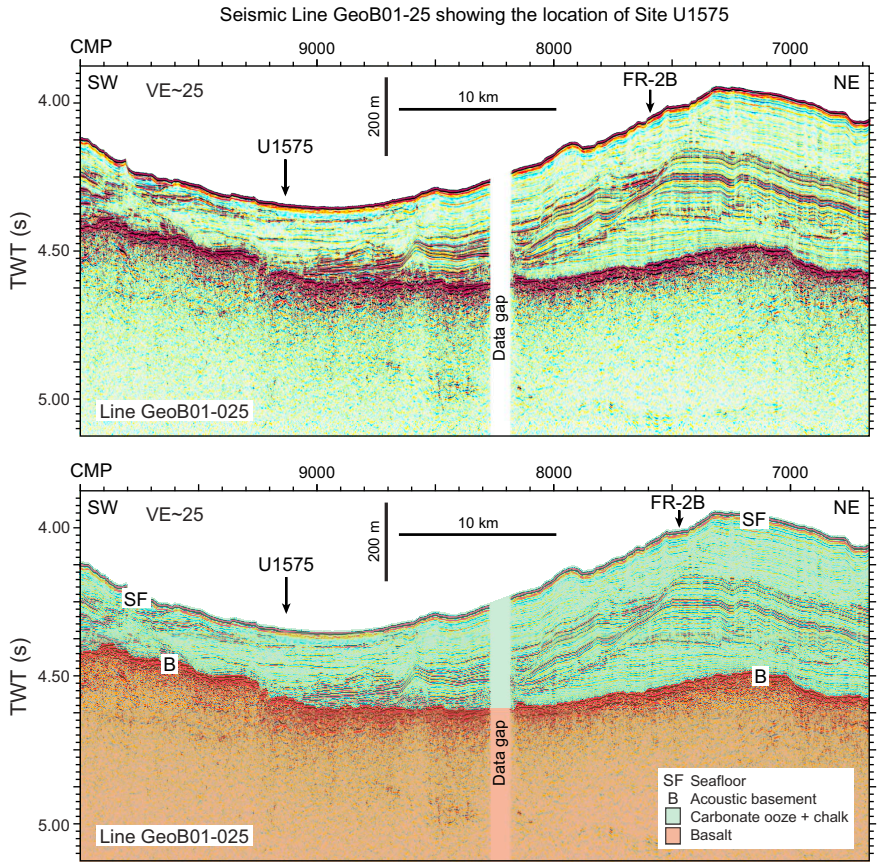


**Figure F14.** Seismic Line GeoB01-25. Top: seismic profile. Bottom: seismic line interpretation. TWT = two-way traveltime, VE = vertical exaggeration.

low-$TiO_2$ (Doros-type) basalts are present in the plume tail, as has been found in the Etendeka (and Paraná) flood basalts (plume head stage) (Zhou et al., 2020). Furthermore, does the Tristan signature, which is found in the younger chain (seamount chain going from Walvis Ridge DSDP Site 527 to Tristan da Cunha Islands), appear in the older portion of the ridge, extending the geochemical zonation of the hotspot track further back in time? The drill cores provided samples that show the eruption age of the main TGW hotspot track in an area that is often overprinted with late-stage volcanism. Furthermore, Site U1575 provided paleomagnetic samples for a time when the hotspot is predicted to have been ~5° north of its current paleolatitude and when the paleolatitude was rapidly changing. The site also recovered sediments deposited near the Benguela Current in a regime that is transitional from continental margin siliciclastic to open-ocean pelagic carbonate deposition, which could reveal past marine environmental conditions.

### 5.1.2. Operations

A single hole was cored at Site U1575 (Table **T1**). Hole U1575A is located at 21°51.9659′S, 6°35.4369′E at a water depth of 3231.3 m as obtained from the precision depth recorder (PDR). In Hole U1575A, we used the RCB coring system to advance from the seafloor to a final depth of 332.3 mbsf and recovered 185.2 m (56%) of sediment and igneous rock. Hole U1575A penetrated 122.4 m of igneous basement. Coring was terminated to meet the remaining major objectives of the expedition. The total time spent on Hole U1575A was 137.0 h, or 5.7 days.

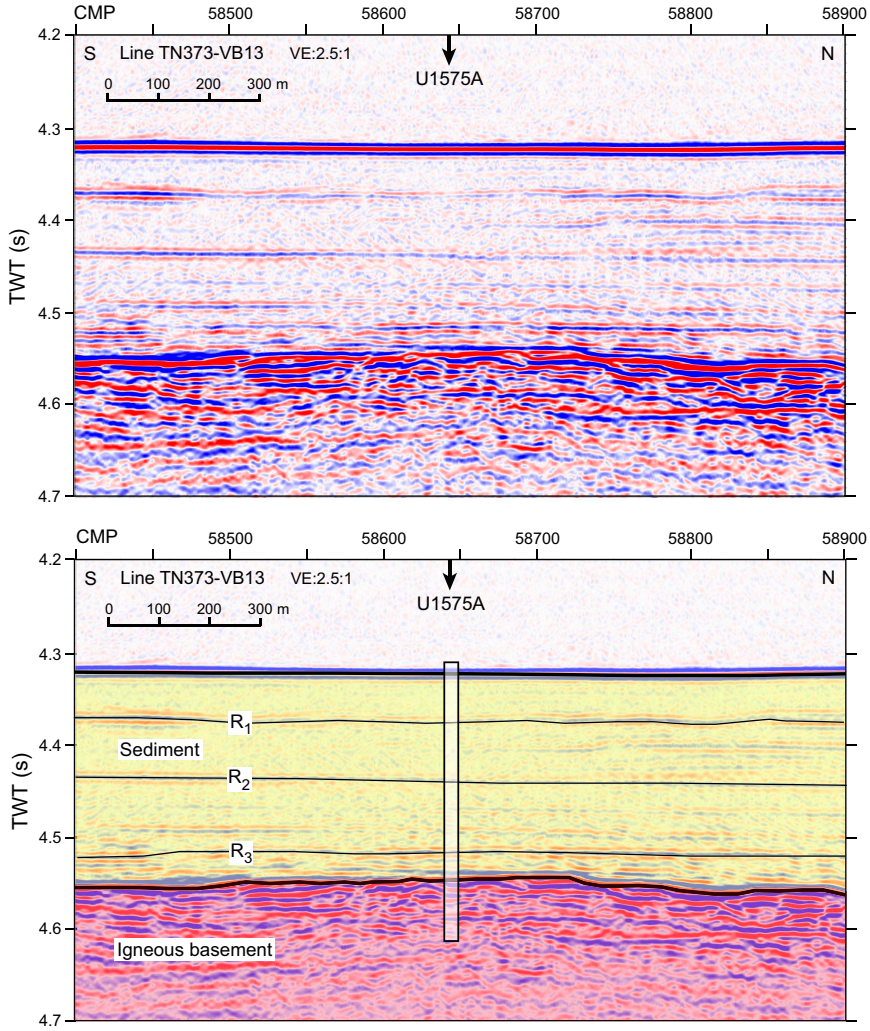


**Figure F15.** Detail of Seismic Line TN373-VB13 illustrating the section cored at Site U1575. Top: uninterpreted data. Bottom: interpretation of layering in seismic section. TWT = two-way traveltime, VE = vertical exaggeration.

## 5.1.3. Principal results

### 5.1.3.1. Sedimentology

The sedimentary cover at Site U1575 includes three lithostratigraphic units that consist of a thick Pleistocene to late Miocene succession of unconsolidated calcareous nannofossil-foraminifera ooze (Lithostratigraphic Unit I; 0–194.10 mbsf) and a much shorter Miocene to Upper Cretaceous succession of poorly lithified nannofossil-foraminifera chalk with clay (Units II and III) to the bottom of the sedimentary succession above the igneous basement (Unit IV) at 209.92 mbsf (Figure F16). It was not clear whether the contact between the sedimentary cover and the uppermost lava in the basement (Igneous Unit 1) was recovered, but sedimentologic observations and preliminary shipboard biostratigraphic and paleomagnetic data do not suggest the existence of a significant time gap between the deposition of the lavas and the overlying sedimentary sequence. Consistent

**Table T1.** Hole summary, Expedition 391. mbsl = meters below sea level. **Download table in CSV format.**

| Hole | Latitude | Longitude | Water depth (mbsl) | Total penetration (m) | Drilled interval (m) | Cored interval (m) | Core recovered (m) | Recovery (%) | Total cores (*N*) | RCB cores (*N*) | Start date (2022) | Start time UTC (h) | End date (2022) | End time UTC (h) | Time on hole (h) | Time on site (days) |
|---|---|---|---|---|---|---|---|---|---|---|---|---|---|---|---|---|
| U1575A | 21°51.9659′S | 6°35.4369′E | 3231.31 | 332.3 | 0 | 332.3 | 185.15 | 55.7 | 41 | 41 | 1 Jan | 1940 | 7 Jan | 1245 | 137.04 | 5.71 |
| | | Site U1575 totals: | | 332.3 | 0 | 332.3 | 185.15 | 55.7 | 41 | 41 | | | | | | 5.71 |
| U1576A | 24°35.7520′S | 5°7.3163′E | 3032.23 | 398.1 | 0 | 398.1 | 309.32 | 77.7 | 42 | 42 | 8 Jan | 0612 | 11 Jan | 1030 | 76.32 | 3.18 |
| U1576B | 24°35.7711′S | 5°7.5513′E | 3027.18 | 450.3 | 365.0 | 85.3 | 66.33 | 77.8 | 16 | 16 | 11 Jan | 1030 | 14 Jan | 1715 | 78.72 | 3.28 |
| | | Site U1576 totals: | | 848.4 | 365.0 | 483.4 | 375.65 | 77.7 | 58 | 58 | | | | | | 6.46 |
| U1577A | 25°12.1439′S | 7°29.8140′E | 3940.16 | 193.9 | 0 | 193.9 | 152.9 | 78.9 | 26 | 26 | 15 Jan | 0615 | 19 Jan | 1950 | 109.68 | 4.57 |
| | | Site U1577 totals: | | 193.9 | 0 | 193.9 | 152.9 | 78.9 | 26 | 26 | | | | | | 4.57 |
| U1578A | 32°19.6836′S | 0°38.5876′W | 3793.81 | 486.4 | 0 | 486.4 | 239.87 | 49.3 | 65 | 65 | 22 Jan | 0502 | 1 Feb | 0900 | 244.08 | 10.17 |
| | | Site U1578 totals: | | 486.4 | 0 | 486.4 | 239.87 | 49.3 | 65 | 65 | | | | | | 10.17 |
| | | Expedition 391 totals: | | 1861.0 | 365.0 | 1496.0 | 953.57 | 63.7 | 190 | 190 | 1 Jan | 1940 | 1 Feb | 0900 | 645.84 | 26.91 |

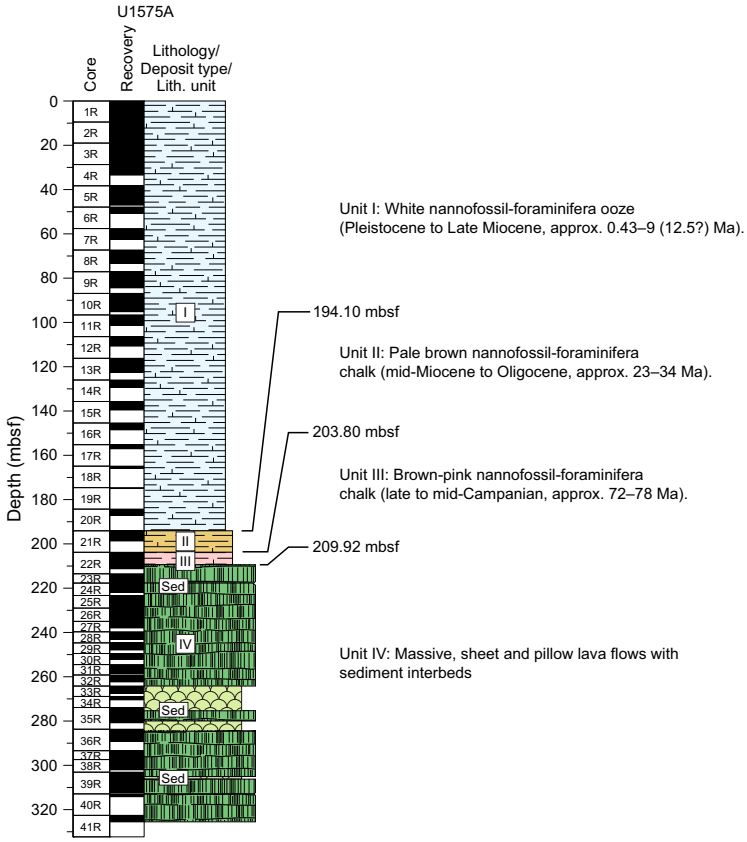


**Figure F16.** Lithostratigraphic summary, Hole U1575A.

with an increase in sediment consolidation downhole, core recovery increases from ~52% in Lithostratigraphic Unit I to ~73% in Unit III.

Unit I consists of a ~195 m thick succession of white nannofossil-foraminifera ooze with minor radiolarians that represents Pleistocene to Pliocene pelagic sedimentation. Subtle gray and, more rarely, white to green centimeter-sized banding occurs throughout due to accumulations of pyrite framboids and possibly Fe-Mn-rich particles. The succession becomes pale brown in the lowermost 10 m of the unit, reflecting a minor increase in the clay content.

Unit II is a much thinner (<10 m) late Miocene to early Oligocene succession (194.10–198.56 mbsf) consisting of a brown nannofossil-foraminifera chalk with minor radiolarians and clays. The chalk is commonly bioturbated and includes subtle white to pale brown color changes controlled by the relative abundance of calcareous (mostly biogenic) components and clays at the centimeter to subcentimeter scale. Rare microscopic particles of palagonite and volcanic minerals of unknown provenance were also observed. Concentrated foraminifera bands and parallel to cross-bedded laminae in the chalk likely indicate local winnowing and reworking by bottom currents.

Unit III represents a ~10 m thick Campanian sequence (198.56–209.92 mbsf) of predominantly consolidated brown to pink nannofossil-foraminifera chalk with rare to minor radiolarians and clays. Bioturbated chalk intervals are interrupted by winnowed bioclastic sand with parallel to cross-bedded laminae and more rarely normal to inverse grading. Volcaniclastic deposits are rare and consist of altered volcanic glass, ferromagnesian and Fe oxide minerals, and feldspars. These clasts are mixed with a dominant bioclastic fraction composed of foraminifera and fragments of inoceramid shells. Rare fragments of red algae were encountered, which suggests deposition of the sequence at <300 mbsf and/or sediment reworking from a nearby shoal. These observations support pelagic sedimentation under the influence of bottom currents and, possibly, low-density turbidity currents.

Few structural features were observed in the sedimentary succession above the igneous basement of Unit IV. Several intervals of tilted bedding occur in Units II and III, which might represent primary sedimentary features or could be due to drilling disturbance effects. The apparent dips of the tilted beds in Unit II are around 11°, whereas those in Unit III are higher, averaging around 39°. Two thick intervals (~30 cm) of sedimentary dikes formed above the tilted beds in Unit III, where sediments are strongly disturbed and mixed with coarse angular grains.

Sedimentary deposits are also present intercalated with the lava succession in the igneous basement (Unit IV). In the upper part of the basement, the sedimentary deposits consist of white azoic to nannofossil-bearing micrite that occurs in layered infills of cavities and cracks between and within the lavas. Farther downhole, below the lower pillow lava package, similar thin intercalations were deposited during hiatuses in volcanic activity.

#### 5.1.3.2. Igneous petrology and volcanology

Hole U1575A penetrated 122.4 m of igneous basement, recovering 71.6 m of rock (58.5%). This basement was divided into 10 igneous units, beginning with a succession of four massive submarine flows (Figure **F17**). Overall, the eruptive style comprises an alternating sequence of submarine lavas involving massive flows (up to 21 m thick), individual sheet flows, and stacks of pillow and lobate lavas (Figure **F17**). All of these units consist of aphanitic to intersertal to holocrystalline basalt with phenocrysts and glomerocrysts of plagioclase (3%–15%) and clinopyroxene (1%–5%). Olivine is sparse and only intermittently present (0%–3%) and is completely altered in ~50% of the lavas. The igneous units show significant overlap in mineralogy but may be summarized as follows: massive flow Igneous Subunits 1a and 1b (8.04 m thick) and 2a and 2b (18.08 m thick) consist of pairs of highly plagioclase-pyroxene ± olivine phyric, holocrystalline basaltic lava flows separated by a glassy margin. Subunits 3a–3d present a change of eruptive behavior and consist of 12.87 m of intercalated succession of sheet flows, lobate flows, and pillow lava (i.e., pillow lava stack). Modal compositions vary from sparsely to highly plagioclase-pyroxene-olivine phyric. Basaltic glass and altered aphanitic material are found in pillow rims and flow boundaries. Unit 4 comprises two massive basalt flows (2.16 and 6.22 m thick) with sparse to moderate plagioclase and pyroxene phenocryst abundance, including sparse olivine. Underlying these massive flows is Unit 5, a thick (15.00 m) succession of pillow lavas that shows numerous glassy margins. Phe-

nocrysts consist of plagioclase and pyroxene with trace amounts of olivine, and the groundmass ranges from glassy to aphanitic to holocrystalline. Units 6–9 range from massive flows (Unit 6 = 4.01 m; Unit 8 = 21.08 m) to thinner underlying pillow lavas (Unit 7 = 4.05 m; Unit 9 = 1.92 m). Mineralogy varies from sparsely to moderately plagioclase-pyroxene phyric, lacking olivine. This sequence erupted onto a nannofossil-foraminifera chalk substrate that is partially preserved at its base and in pillow lobe interstices as disturbed and deformed material. At the bottom of Hole U1575A, Subunits 10a (5.06 m) and 10b (13.31 m) consist of one massive flow each, separated by chilled margins. They are moderately phyric and consist of variable proportions of plagioclase, pyroxene, and olivine with glomerophyric and holocrystalline textures. Alteration in the igneous basement is due to ambient low-temperature seafloor processes. Oxidative alteration likely occurred shortly after eruption as cooling lava units were subjected to seawater ingress, aided by the development of cooling fractures in the brittle outer flow crust, leading to calcite precipitation in fractures. Alteration intensity is slight to occasionally moderate throughout, with centers of thicker flows presenting near-fresh primary minerals (except for olivine). Low-temperature alteration is also reflected by carbonate vein networks, which vary in thickness and orientation. These veins are frequently observed in the uppermost 20 m of the volcanic succession of Unit IV and decrease in abundance downhole. Throughout the igneous basement, the degree of overall alteration correlates positively with the abundance of carbonate veins.

### 5.1.3.3. Biostratigraphy

Detailed calcareous nannofossil and planktonic foraminifera biostratigraphy was performed on core catcher samples recovered from Hole U1575A. Microfossil examination provided a preliminary chronostratigraphic framework for sediments at Site U1575. First occurrence (FO) and last occurrence (LO) datums were largely based on Gradstein et al. (2020).

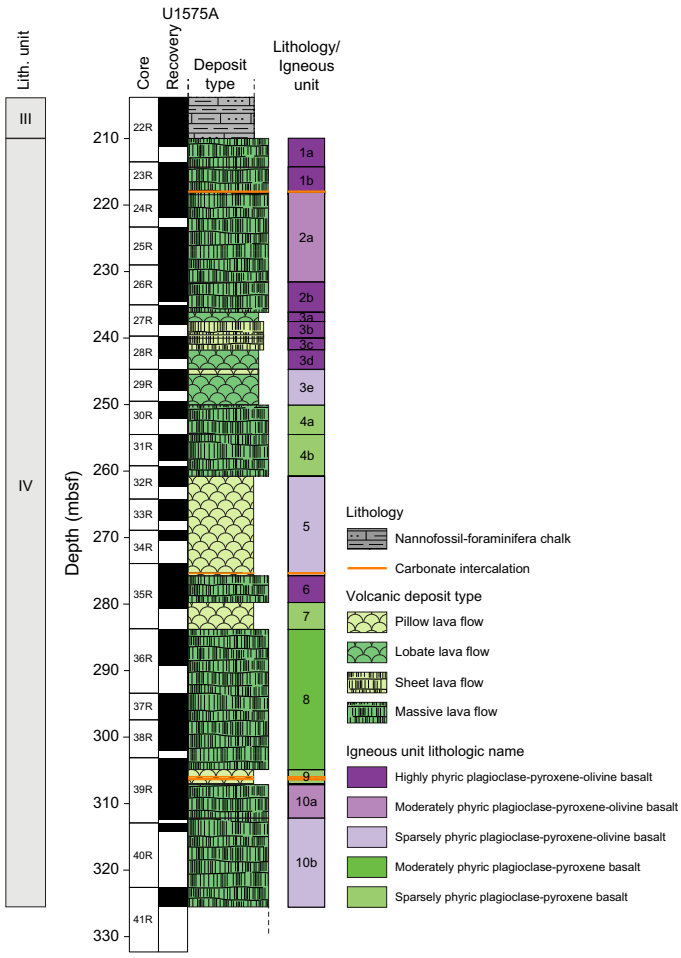


**Figure F17.** Stratigraphic column for the volcanic succession in Lithostratigraphic Unit IV, Hole U1575A.

The sediment succession at Site U1575 spans the Pleistocene to Upper Cretaceous (upper Campanian) time interval (0.43–78 Ma). An almost continuous Pleistocene to Pliocene pelagic sediment succession was recorded in Lithostratigraphic Unit I, ranging 0.43–4.50 Ma (possibly excluding the earliest Pliocene [Zanclean]). Key taxa for this time interval for calcareous nannofossils are *Pseudoemiliania lacunosa*, *Helicosphaera sellii*, *Discoaster tamalis*, and *Amaurolithus primus*. Key taxa of planktonic foraminifera for this interval are *Globorotalia hessi*, *Globorotalia crassaformis*, and *Globorotalia margaritae*. Uncertainties in the assignment of the Pliocene/Miocene boundary were noted based on shipboard examination, and higher resolution studies will be required to verify this boundary. The interpretation of the Miocene interval in Unit II was more complex due to possible hiatuses, poor recovery, and the presence of mixed assemblages. A tentative biostratigraphic framework places this part of the sequence in the upper Miocene, and further postexpedition investigation is required. In Sections 391-U1575A-20R-CC through 21R-CC, Unit II shows a time gap and extends to the lowest Oligocene (Rupelian), as detected by the occurrence of calcareous nannofossil *Reticulofenestra umbilicus* in Section 21R-CC. Farther downhole, a major unconformity separates early Oligocene and late Campanian flora and fauna recorded in Units II and III, respectively; the latter is the lowermost part of the cored sedimentary succession. The maximum age detected is ~78 Ma (Section 20R-CC) based on the occurrence of nannofossil species *Eiffellithus eximius* and *Uniplanarius sissinghii* along with the absence of *Uniplanarius trifidus*. Samples were taken from thin sediment layers interbedded with lava flows within the igneous basement (Unit IV), but preliminary age determination will require postexpedition analysis.

#### 5.1.3.4. Paleomagnetism

Sediments recovered at Site U1575 are weakly magnetic (ranging $10^{-6}$ to $10^{-3}$ A/m) in Cores 391-U1575A-1R through 20R (0–194.1 mbsf). As such, both the superconducting rock magnetometer (SRM) and the JR-6A spinner magnetometer failed to produce reliable directions, and no magnetostratigraphy could be determined for this interval. Lithified basal sediments from Cores 21R and 22R had stronger magnetizations (ranging $10^{-3}$ to $10^{1}$ A/m). Several intervals within the basal sediments, however, exhibited pervasive tilting, precluding determination of a robust magnetostratigraphy for Cores 21R and 22R. Nevertheless, we interpret Sections 22R-4 and 22R-5 to represent reversed polarity Chron 32r.

Igneous rocks recovered at Site U1575 are characterized by low unblocking temperatures (~150°–450°C) and median destructive field values ranging ~5–125 mT. These unusually high coercivity values are likely caused by the presence of dendritic iron oxides (most likely titanomagnetite or titanomaghemite), which can exhibit strong magnetic anisotropy. These phases were observed in thin sections of Hole U1575A igneous rocks. Thermal demagnetization of some discrete samples showed evidence of possible partial self-reversal of magnetization. All samples subjected to alternating field (AF) demagnetization displayed a drill string overprint that was typically removed by 20 mT before revealing a unidirectional origin-trending component. Magnetic inclinations obtained using principal component analysis from discrete samples agree well with inclinations associated with the 20 mT AF demagnetization step in SRM data acquired from archive-half section at corresponding depths. Nearly all measurements are of normal polarity, consistent with basement formation during the Cretaceous Normal Superchron (C34n).

#### 5.1.3.5. Geochemistry

At Site U1575, interstitial water (IW) samples were analyzed for pH, alkalinity, major cation and anion concentrations, and trace element concentrations. An alkalinity maximum is identified at 12 mbsf. Slightly below this depth, at 25–30 mbsf, maxima for pH, calcium, potassium, strontium, and silicon and minima for magnesium and lithium concentrations are observed. These features are attributable to diageneses of biogenic carbonates and silica in Lithostratigraphic Unit I. A manganese reduction interval is found at 1.5–10 mbsf, followed by a sulfate reduction interval at 10–50 mbsf. The peaks of phosphate and ammonium located at 1.5 and 50 mbsf, respectively, are consistent with the manganese and sulfate reduction zone. Because of the hiatus between Lithostratigraphic Units I and II, no signs of interaction between basaltic basement and Unit I are observed, and profiles of many elemental concentrations remain uniform between 50 and 200 mbsf. Sediment samples were also analyzed to determine the content of $CaCO_3$, total carbon, and total organic carbon. In Unit I (dominantly nannofossil-foraminifera ooze), the $CaCO_3$ content ranges 93–98 wt%. In Units II and III (dominantly nannofossil-foraminifera chalk), the $CaCO_3$

content declines to 85 and 74 wt%, respectively. Methane concentrations measured from the headspace gas are at the atmospheric background level (lower than 2.0 µL/L).

Representative samples obtained from the igneous basement were analyzed using inductively coupled plasma–atomic emission spectroscopy (ICP-AES) and portable X-ray fluorescence (pXRF) on both rock powders (n = 33) and surfaces of archive-half section rock pieces (n = 128). Overall, comparison of the ICP-AES and pXRF results from the same samples displays excellent to good correlation. The loss on ignition (LOI), a common indicator for the degree of alteration, is relatively low for such old submarine rocks (<3 wt%). Nevertheless, K and Sr enrichment due to seawater interaction and olivine alteration affect the composition of the analyzed lavas to variable degrees, which has also been documented by petrographic investigations. All igneous rock samples are basalts and have Ti/V values similar to MORBs and ridge-centered ocean island basalts. Downhole geochemical variations display an overall increase in MgO, possibly reflecting increasing differentiation of the magma reservoir with decreasing age. The most striking geochemical variability is observed at ~274 mbsf. In the upper portions of the recovered interval, the $TiO_2$ content is relatively constant and sharply drops at 274 mbsf at the bottom of Igneous Unit 5. Thereafter, the $TiO_2$ value remains constant throughout Units 5–8 and slowly increases from Unit 9 to Unit 10 again to a concentration similar to the upper part of the volcanic sequence (Units 1–5). This Ti evolution correlates with similar patterns for Sr, Y, and Zr. Another geochemical anomaly was identified around 255 mbsf in the lower part of Subunit 4a, which shows an enrichment of $TiO_2$, Ni, and Cu.

#### 5.1.3.6. Physical properties

Physical properties measurements were made on recovered whole-round and section half cores as well as discrete cube and wedge samples, indicating three distinct units that correspond to the established lithostratigraphic units: (1) calcareous ooze, (2) chalk, and (3) basalt. Within the sedimentary succession, natural gamma radiation (NGR) and magnetic susceptibility (MS) peaks at ~194 mbsf correlate to the calcareous ooze/chalk contact; mean NGR values increase from 3.3 to 16.0 counts/s and average MS increases from 1.0 to 38.1 SI × $10^{-5}$. The transition from the sedimentary overburden to igneous basement is imaged at ~210 mbsf by gamma ray attenuation (GRA) bulk density, moisture and density (MAD) bulk density, and NGR average values. Bulk density increases from 1.73 to 2.59 g/cm$^3$ (GRA) and from 1.89 to 2.85 g/cm$^3$ (MAD), and NGR decreases from 8.68 to 3.20 counts/s across the sediment/basement interface. Intervals of low MS and point magnetic susceptibility (MSP) values appear to correlate with intervals of highly fragmented basalt, and higher values (~1000 to ~3000 SI × $10^{-5}$ for both instruments) appear to be associated with intervals of coherent (length >20 cm) basalt core pieces. These trends are consistent with GRA bulk density and NGR measurements from the same intervals. However, anomalously high MS/MSP and NGR values in a rubbly zone appear to correspond to a shift from high to low $TiO_2$ concentrations in the volcanic sequence at ~270 mbsf.

## 5.2. Site U1576

### 5.2.1. Background and objectives

Site U1576 (proposed Site VB-14A) is located on the middle west flank of Valdivia Bank, the broad oceanic plateau that is part of Walvis Ridge (Figures **F1**, **F18**). The site was chosen to obtain samples from midflank igneous basement, buried by several hundred meters of sediment, in a location that can only be sampled by drilling (Figures **F19**, **F20**). Valdivia Bank represents a poorly understood edifice of Walvis Ridge that may have formed by interaction of a mantle plume with the Mid-Atlantic Ridge or a microplate formed by a plate boundary reorganization. Radiometric age dating is planned to determine the age of the igneous basement at this site. Along with other drill site sampling of Valdivia Bank, age dating will enable us to test whether there is a north–south age progression, as predicted by hotspot models, or an east–west age progression, as predicted by plume-ridge interaction models. The petrology and geochemistry of the basement basalt samples should elucidate the petrogenesis and mantle sources of these magmas, including whether the isotopic zonation observed at the DSDP Leg 74 transect, a few hundred kilometers to the southwest, continues to Valdivia Bank. Paleomagnetic data from sediment and basalt samples will help determine the paleolatitude of the hotspot during the Late Cretaceous. Sediments recovered at Site

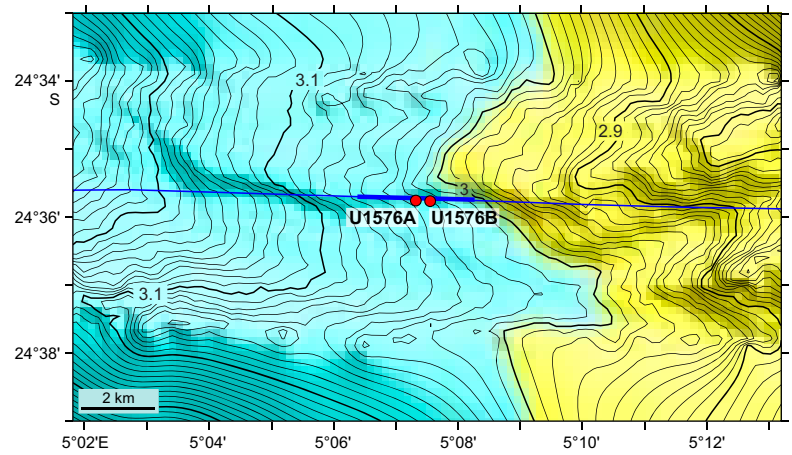


**Figure F18.** Bathymetry of Site U1576 and environs. Detailed multibeam bathymetry around Seismic Line TN373-VB08 is merged with the SRTM15+ bathymetry grid (Tozer et al., 2019). Contours are plotted at 10 m intervals and labeled in kilometers. Blue line represents Seismic Line TN373-VB08. Heavy blue line shows the portion of the line shown by Figure F19.

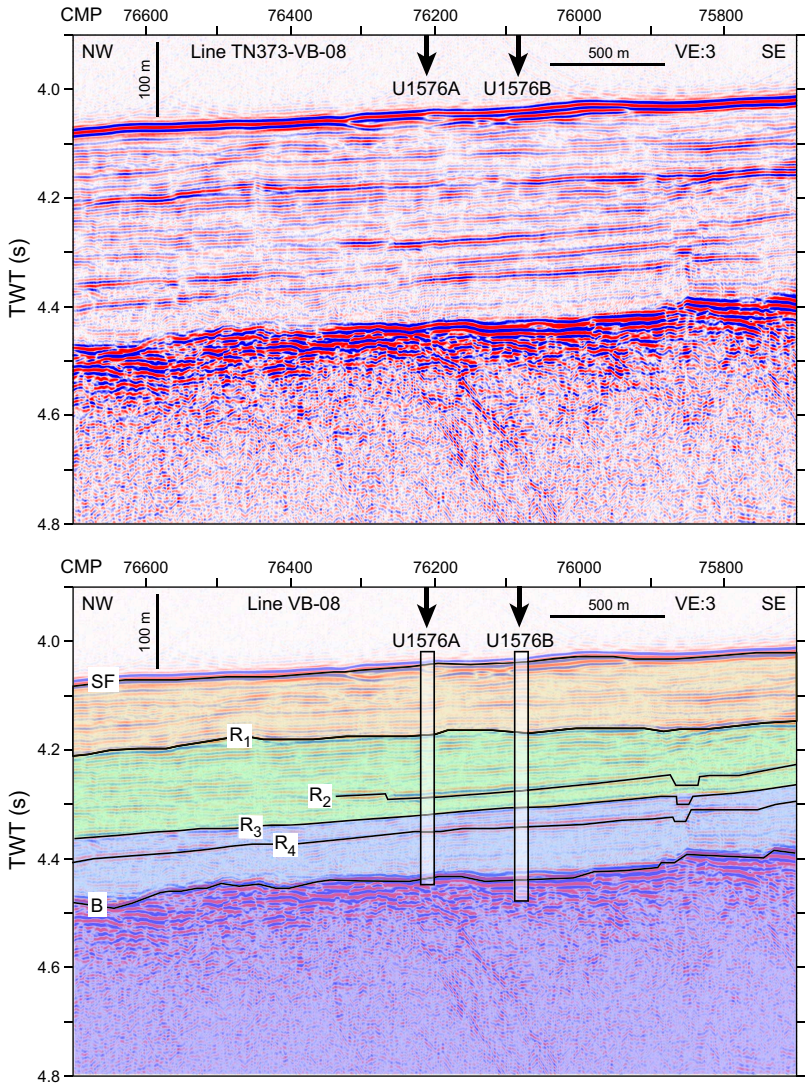


**Figure F19.** Detail of Seismic Line TN373-VB08 and locations of Holes U1576A and U1576B. Top: uninterpreted seismic data. Bottom: seismic line interpretation. SF = seafloor reflector, B = basement reflector. R1, R2, etc., = seismic reflectors. TWT = two-way traveltime, VE = vertical exaggeration.

U1576 will help constrain the age and evolution of the plateau and provide insights into the paleoenvironmental trends of the midwater column of the South Atlantic.

### 5.2.2. Operations

Two holes were drilled at Site U1576 (Table **T1**). Hole U1576A is located at 24°35.7520′S, 5°7.3163′E at a water depth of 3032.3 m as obtained from the PDR. In Hole U1576A, we used the RCB coring system to advance from the seafloor to a final depth of 398.1 mbsf and recovered 309.3 m (78%) of sediment and igneous rock. After attempts to clear a plug in the outer core barrel and bit at the bottom of the hole failed, it was decided to abandon Hole U1576A and offset the drilling 400 m along the site survey seismic line at an orientation of 95° (Figure **F19**) to start a new hole (U1576B). The total time spent on Hole U1576A was 76.25 h, or 3.2 days. In Hole U1576B, located at 24°35.7711′S, 5°7.5513′E at a water depth of 3027.2 m as obtained from the PDR, we first drilled without recovery from the seafloor to 365.0 mbsf. The RCB coring system was then deployed to advance from 365.0 mbsf to a final depth of 450.3 mbsf with a recovery of 66.3 m (78%) of sedimentary and igneous rock. Coring was terminated early to complete the remaining major objectives of the expedition. In total, Holes U1576A and U1576B penetrated 17.9 m and 64.9 m of igneous basement, respectively. The total time spent on Hole U1576B was 78.75 h, or 3.3 days. Overall, we spent 155.0 h, or 6.5 days, at Site U1576.

### 5.2.3. Principal results

#### 5.2.3.1. Sedimentology

The sedimentary succession at Site U1576 is divided into four lithostratigraphic units. It consists of a ~380 m thick succession of ooze and chalk on top of a volcanic basement (Figure **F21**) and six intercalations of chalk in the volcanic basement for an additional cumulated sediment thickness of ~40 m (Figure **F22**). Two holes were drilled at Site U1576. Hole U1576A recovered the sedimentary cover from 0 to 380.18 mbsf. Hole U1576B recovered the lower ~20 m of this sedimentary cover from 365.00 to 380.18 mbsf and then six sedimentary intervals in the volcanic basement to 441.36 mbsf (Figure **F22**). Excellent lithostratigraphic correlation was found in the lower ~20 m of the sedimentary cover retrieved in the two holes. The sedimentary cover is divided into four main lithostratigraphic units of ooze (Lithostratigraphic Unit I) and chalk (Units II–IV) that were deposited on top of the volcanic basement between the Pleistocene and early Campanian. Drilling disturbance is present throughout the ooze of Unit I but is commonly restricted to the outermost edges of the cores with uparching of the bedding (i.e., beds form an inverted U). Increased consolidation in the chalk of Units II–IV allowed better preservation of sedimentary detail with only local biscuiting and minor uparching of the bedding. Core recovery ranges from ~75% in Unit I (0–96.83 mbsf) to ~89% in Unit II (96.83–124.71 mbsf) and Unit III (124.71–322.19 mbsf) and ~52% in Unit IV (Hole U1576A = 322.19–380.18 mbsf; Hole U1576B = 365.00–385.28 mbsf).

Unit I is a 96.83 m thick sequence of unconsolidated nannofossil-foraminifera ooze and nannofossil ooze with foraminifera, locally with clay and minor radiolarians, that records pelagic sedi-

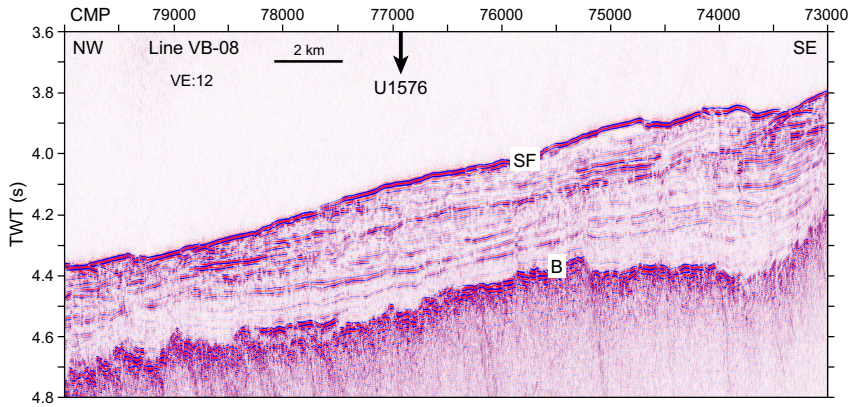


**Figure F20.** Regional section of Seismic Line TN373-VB08. TWT = two-way traveltime, VE = vertical exaggeration, SF = seafloor reflector, B = igneous basement reflector.

mentation between the Pleistocene and middle Miocene. Three subunits were defined in Unit I based on a distinct brownish color correlated with minor changes in clay content. The lower boundary of the unit is marked by a sharp contact with brown-pink calcareous ooze/chalk with clay in Unit II.

Unit II represents a ~28 m thick sequence of unconsolidated to consolidated pale brown to brown foraminifera-nannofossil ooze/chalk with clay and minor radiolarians that records pelagic sedimentation during the Paleocene. The base of the unit corresponds to the occurrence of a distinctive ferromanganese crust at the top of Unit III, which likely represents a significant reduction or pause in ooze accumulation very close to or at the Cretaceous/Paleogene (K/Pg) boundary. Unit II is almost exclusively composed of layered, slightly to heavily burrowed foraminifera-nannofossil ooze/chalk with clay with regular color changes that form approximately 10–50 cm thick cycles with more prominent burrowing in the darker intervals. A minor fraction (volume = <1%) of the unit consists of partly disaggregated layers and beds of well-sorted foraminifera to volcanic sand, of which the nature and origin(s) remain poorly constrained due to drilling disturbance. These beds could represent winnowing of the ooze by bottom currents as well as volcaniclastic deposition by turbidites and/or tephra fallout.

Unit III consists of a ~197 m thick sedimentary succession predominantly composed of well-defined cyclical white and reddish brown or greenish gray foraminifera-nannofossil chalk with clay that records pelagic sedimentation between the Maastrichtian and the Campanian. Two subunits (IIIA and IIIB) were defined in Unit III based on progressive attenuation of reddish brown coloring of the chalk and its replacement by a greenish gray color, which may correspond to a transition from predominantly oxidative to predominantly reducing conditions on the seafloor starting at ~275 mbsf (approximately middle Campanian). The base of the unit is marked by almost complete attenuation/replacement of the reddish brown color downhole and the first

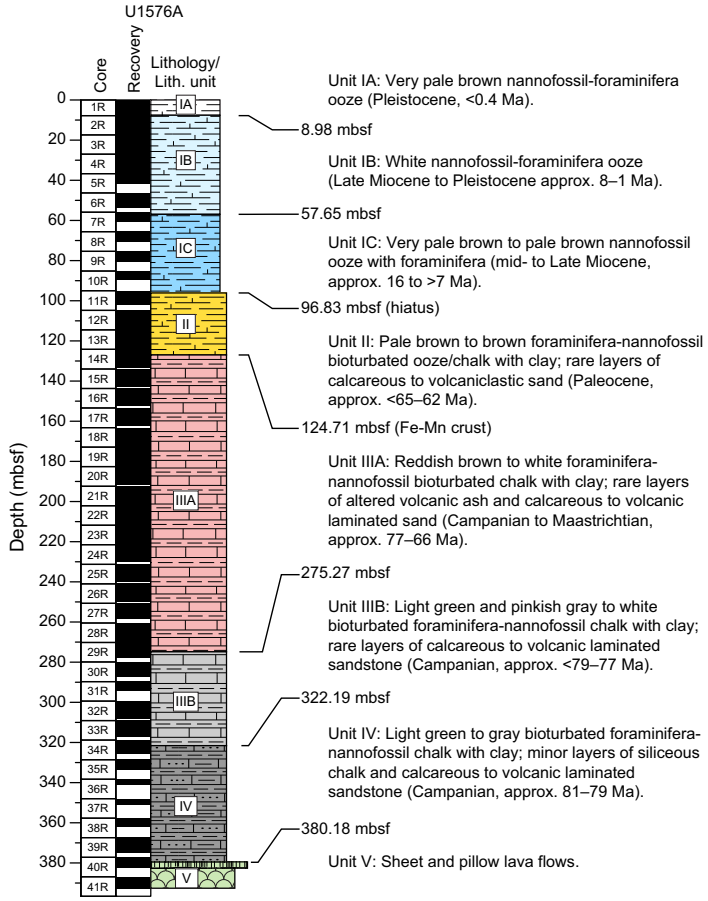


**Figure F21.** Lithostratigraphic summary, Hole U1576A.

appearance of thin centimeter-sized bands of dark green siliceous chalk in Unit IV. Similar to Unit II, the chalk of Unit III is interbedded or mingled with sparse volcanic to calcareous sand. These are commonly laminated and normally graded and are considered to represent infrequent bottom and/or turbidity currents. Unit III is also characterized by sparse, thin layers of altered ash that are interpreted as distal tephra deposits preserved during periods of low sedimentation and/or bioturbation in the pelagic sediment.

Unit IV is a ~20 m (Hole U1576B; 365.00–385.28 mbsf) to ~58 m (Hole U1576A; 322.19–380.18 mbsf) thick sedimentary sequence that is predominantly composed of light green to darker gray foraminifera-nannofossil chalk with clay and locally faint nuances of pinkish gray intervals. Similar to Subunit IIIB, the chalk represents pelagic sedimentation in anoxic conditions during the early Campanian, possibly reflecting cyclical sedimentation. Calcareous and volcanic sandy deposits similar to those observed in Units II and III become slightly more important in Unit IV, forming 5% of the recovered sediment. The lower boundary of Unit IV corresponds to the inferred (i.e., not recovered) contact with the underlying igneous succession (Unit V) in Holes U1576A and U1576B. The correlation of Unit IV between Holes U1576A and U1576B is further established by the occurrence of a ~1.61 m thick matrix-supported calcareous conglomeratic deposit that defines a clear stratigraphic marker ~18.2 and 16.0 m above the igneous basement in Holes U1576A and U1576B, respectively. This lithology and other calcareous clastic deposits record a turbidite-rich interval in Unit IV. Tilted beds observed in Unit IV usually show low apparent dip angles of less than 10°. Apparent angles of up to ~55° are occasionally present close to the sediment/basement contact.

Seven sedimentary interbeds (S1–S7) of variable thickness (~0.8–11.7 m) recovered as intercalations within the volcanic basement in Hole U1576B are a downhole continuation of the litho-

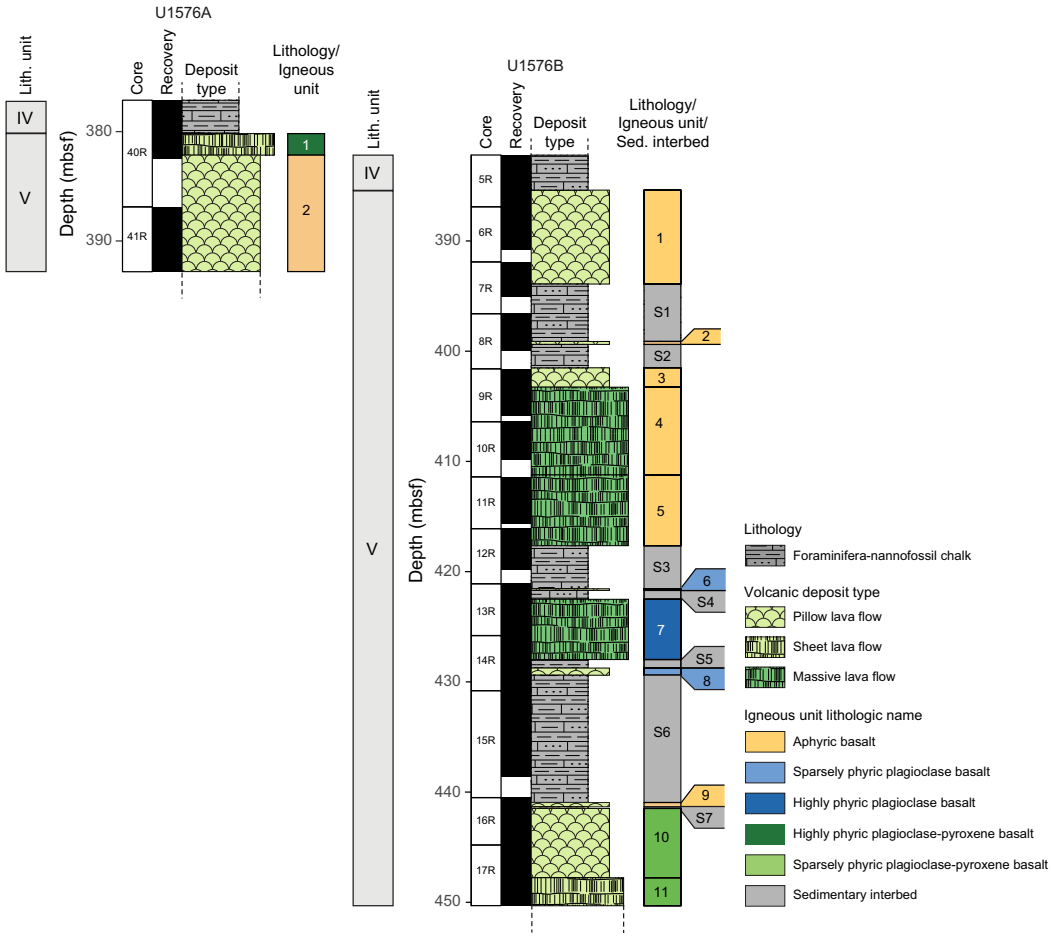


**Figure F22.** Igneous stratigraphic column, Holes U1576A and U1576B. Sed = sedimentary.

logies retrieved in the lower sedimentary cover above the uppermost basalt lava (Unit IV). Sedimentation is similarly dominated by pelagic deposition of gray bioturbated foraminifera-nannofossil chalk with clay with thin interbeds of calcareous to volcaniclastic turbidites. Locally, lava-sediment interaction led to formation of peperites and hydrothermal alteration of both basalt and sediment. A submeter interval of metalliferous sedimentation occurs at ~420 mbsf between lavas, which similarly suggests nearby synvolcanic hydrothermal activity on the seafloor. Intervals of significant deformation were found in two sediment interbeds. Healed fractures and tilted beddings show various dipping angles. Both normal and reversed faults occur. Deformation structures include conjugate normal faults as well as en echelon and downward splaying normal faults.

#### 5.2.3.2. Igneous petrology and volcanology

Igneous rocks were recovered from Holes U1576A and U1576B. The igneous basement at Site U1576 represents Lithostratigraphic Unit V in the overall subseafloor succession, and the two holes are stratigraphically correlated (Figure **F22**). Hole U1576A penetrated 12.62 m of igneous basement, recovering 7.56 m (~60%), and consists entirely of basalt. Two igneous units are identified in Hole U1576A (Figure **F22**). The first unit is a sheet flow (1.97 m), and the second unit consists of pillow basalt, in which the hole terminates at 10.65 m cored thickness. The lavas range from glassy and aphanitic to holocrystalline and intersertal. Fresh glass is present in the pillow sequence and on the tops of some sheet flows. The lavas are slightly vesicular with small (~1 mm) round vesicles and range from aphyric to highly phyric (plagioclase = 9%–12%; clinopyroxene = 6%–8%). Hole U1576B penetrated 64.9 m of igneous basement, recovering 51.48 m (~79%), consisting of 32.79 m of basalt and 18.69 m of intercalated chalk and turbidite horizons (Figure **F22**). Hole U1576B terminates within a sheet flow with a minimum thickness of 2.56 m. A total of 11 igneous units were identified in Hole U1576B, comprising pillow, sheet, and massive lava flows, with cumulative total drilled thicknesses of 18.16, 2.56, and 20.02 m, respectively (Figure **F22**). The top basaltic unit consists of completely altered pillow basalt lava flows that correlate to the pillow basalts at the base of Hole U1576A. Igneous Units 1–3 (pillow lava flows) and 4–5 (massive lava flows) represent aphyric basalts with plagioclase microphenocrysts occurring occasionally. Units 6–11 (one massive flow, one sheet flow, and several pillow basalt flows) are sparsely plagioclase ± clinopyroxene phyric (2%–4% total phenocrysts). Massive and sheet flows contain both plagioclase and clinopyroxene glomerocrysts and phenocrysts in an intersertal groundmass, showing higher phenocryst abundances (8%) in the center of the flows. Seriate textures are common in massive lava interiors, whereas clear porphyritic textures are found closer to flow boundaries. Pillow lavas contain plagioclase and clinopyroxene microlites and small glomerocrysts in their glassy rims. Olivine occurs infrequently (<1%) and is completely altered. Fresh glass is present at some flow margins, but it is mostly altered and replaced by clay minerals. The lavas are dominantly nonvesicular to slightly vesicular, except for the pillow lavas of Unit 2, which are moderately to highly vesicular with vesicles filled by secondary minerals. Alteration in the basalt lava successions in both holes at Site U1576 is significant and pervasive at the tops and bottoms of lava flows and throughout the interiors of small flows; only the larger massive flow cores contain near-fresh igneous minerals. Chemically reduced hydrothermal fluids dominated alteration processes, which caused a pale green discoloration and formation of secondary pyrite in vesicles and in the groundmass. This alteration is distinctive from the pale reddish tan color associated with the oxidative alteration at Site U1575. Alteration-derived veins that crosscut each other are common within the recovered volcanic sequence, indicating multiple phases of hydrothermal fluid percolation.

#### 5.2.3.3. Biostratigraphy

Detailed calcareous nannofossil and planktonic foraminifera biostratigraphy was performed on 39 and 16 core catcher samples, respectively, from the continuous sediment successions of Holes U1576A and U1576B. Five additional core catchers were analyzed for calcareous nannofossils from the interbedded sediments recovered from Hole U1576B. Core catcher samples were analyzed for FO and LO datums, which were based on Gradstein et al. (2012, 2020). Nannofossil and foraminifera datums showed good agreement throughout the cored sediment sequence. Biostratigraphic analysis revealed a succession of Pleistocene through lower Miocene (Lithostratigraphic Subunits IA–IC) sediments that is likely incomplete. Additional analysis of these units is required to determine where and how much time is encompassed within the potential hiatuses. A large

hiatus/unconformity is observed between the oldest Miocene sediments (Langhian) in Section 391-U1576A-10R-CC and lower Paleocene (Danian) sediments in Section 11R-CC, suggesting that the Lithostratigraphic Unit I/II boundary corresponds to a major, ~45 My hiatus in the upper part of the Hole U1576A sediment succession, with both the Oligocene and Eocene missing from retrieved cores. Sediments recovered below the unconformity revealed an apparent continuous section from the lower Paleocene (Danian) through the Upper Cretaceous (Maastrichtian/Campanian). This succession likely contains the K/Pg boundary and will be closely analyzed post-expedition to determine its exact placement within the cored sequence. The lower part of the sediments provided a maximum early Campanian basement age of approximately 79.00–81.38 Ma. Interbedded sediments recovered from Hole U1576B revealed only Campanian ages. These interbeds likely represent an older continued succession of the basement interval recovered from Hole U1576A, with most samples assigned to lower Campanian biozones.

#### 5.2.3.4. Paleomagnetism

Cores 391-U1576A-1R through 10R are primarily composed of weakly magnetic (ranging $10^{-6}$ to $10^{-3}$ A/m) unconsolidated calcareous nannofossil ooze. As such, both the SRM and JR-6A spinner magnetometer failed to produce reliable directions, and no magnetostratigraphy could be determined for this interval. Lithified sediments were recovered from Cores 391-U1576A-11R through 39R and Sections 391-U1576B-2R-1 through 5R-3. These lithified sediments have stronger magnetizations (ranging $10^{-5}$ to $10^{-3}$ A/m) and produced higher quality magnetic measurements, which permitted development of a robust magnetostratigraphy for these intervals. Demagnetizations carried out on discrete samples agree well with section-half measurements and suggest that magnetization is carried by a mixture of magnetite and hematite. For Hole U1576A, we identified 14 polarity chrons that span from the Danian (Chron 26r in Core 11R) to the early Campanian (Chron 33r near the contact with igneous basement). We assigned polarity chrons for sedimentary cores from Hole U1576B that were consistent with polarity chrons from Hole U1576A. Sections 391-U1576B-2R-1 through 4R-2 are of normal polarity and are consistent with normal Chron 33n. These are underlain by sedimentary Sections 5R-1 through 5R-3, which make contact with the basement and exhibit reversed polarity consistent with Chron 33r. No major gaps were identified in the magnetostratigraphy in the Paleocene and older sediments.

Igneous rocks recovered from Site U1576 span Cores 391-U1576A-40R through 41R and 391-U1576B-5R through 17R. These cores consist of basalts with interbedded chalk between flows. Some of the basalts are considerably altered, particularly close to contacts with sediment interbeds, changing their magnetic characteristics. Magnetic intensities range $10^{-5}$ to $10^{-2}$ A/m in the sediment interbeds and heavily altered basalt and 1–10 A/m in the mostly unaltered basaltic sections. Nearly all igneous cores display a reversed polarity magnetization after AF cleaning to 20 mT, which is compatible with the reversed polarity chron assignment of Chron 33r observed at the top of the igneous basement. Most of the igneous rocks are characterized by unblocking temperatures between 200° and 550°C and median destructive field values around 20 mT. The large range of magnetization unblocking temperatures is most likely related to the presence of titanomagnetite with varying Ti concentrations.

#### 5.2.3.5. Geochemistry

At Site U1576, IW samples from Hole U1576A were analyzed for pH, alkalinity, and concentrations of major cations, anions, and trace elements. Both alkalinity and pH peak at 230–250 mbsf in Lithostratigraphic Subunit IIIA. Across the entire sedimentary succession, we observe linear increases in calcium and lithium concentrations and linear decreases in magnesium and potassium concentrations. Two maxima of silicon concentration, near the top of the sediment and at the bottom of the sediment succession, are attributable to dissolution of biogenic silica and volcanic sands, respectively. A broad manganese peak found in Unit I through the upper part of Subunit IIIA indicates the presence of a manganese reduction interval in the upper part of the sediment succession. A sulfate reduction interval is also observed in Unit I through the upper part of Subunit IIIA. We observe the phosphate maximum at 1.8 mbsf with a narrow peak in Subunits IA and IB. The ammonium concentration is consistent across the entire sediment depth. In general, IW geochemistry at Site U1576 is affected by diagenetic processes of calcite, silica, and organic matter, as well as interactions of interstitial waters with volcanic basement and volcanic sands. Sediment samples were also analyzed for $CaCO_3$, total carbon, and total organic carbon contents. $CaCO_3$

content remains high across Subunits IA–IIIA and declines in Subunit IIIB and Unit IV as the content of clay increases. Methane concentrations measured from the headspace gas are lower than the atmospheric background level of 2.0 µL/L.

At Site U1576, 2 samples from Hole U1576A and 10 samples from Hole U1576B were analyzed using ICP-AES on powders and pXRF on 59 archive-half section pieces of the recovered cores for the determination of major and trace elements. Even though the least altered recovered sections of the distinct lithologies were analyzed, several samples were affected by varying degrees of alteration, as demonstrated by scattered concentration data of fluid-mobile elements (e.g., K). The analyzed rocks are all subalkaline and range from basalt to basaltic andesite. The Ti-V composition of all samples from Site U1576 is similar to MORBs and ridge-centered ocean island basalts. Interestingly, V and $TiO_2$ are well correlated at Sites U1575 and U1576, but the trend is shifted, and Site U1576 has a slightly lower V concentration at a given Ti content. On bivariate diagrams with MgO versus the other major oxides and trace elements, the Site U1576 rocks generally lie within the compositional array of the previously reported dredge and DSDP site samples from Walvis Ridge. Two igneous units are distinguished in Hole U1576A, and 11 are distinguished in Hole U1576B. Based on the lithology and geochemical composition, the second unit of Hole U1576A and first unit of Hole U1576B appear to be indistinguishable; they most likely represent the same pillow lava flow stack. Therefore, 12 distinct igneous units are present within the combined volcanic succession at Site U1576. Geochemical downhole variation using pXRF and ICP-AES analysis shows that all lavas in both holes at Site U1576 have high $TiO_2$ concentration, unlike Site U1575, which contains lavas with both high and low $TiO_2$ contents.

#### 5.2.3.6. Physical properties

Physical properties measurements were made on 93 cores from Holes U1576A and U1576B. NGR, MS/MSP, GRA bulk density, *P*-wave velocity, porosity, and thermal conductivity measurements reveal a relatively simple succession of sedimentary and volcanic units in Hole U1576A: calcareous ooze grading into more cohesive chalk and limestone from the seafloor to ~380 mbsf and relatively altered basalt flows and pillows to the bottom of the hole at ~392 mbsf. In Hole U1576B, the same suite of measurements recorded a more complex sequence of interbedded sediment and basalt units below the initial sediment/basement contact at ~385 mbsf to the bottom of the hole at ~451 mbsf. Localized features within the sedimentary and volcanic intervals of both holes are also reflected by physical properties data sets, specifically NGR and MS/MSP. In Hole U1576A, the highest MS ($325 \times 10^{-5}$ SI) recorded in the sediment interval correlates to a ~4 cm thick volcaniclastic deposit at ~135 mbsf (Section 15R-1), and at the same depth, NGR abruptly increases to 22.2 counts/s from a background range of ~6–8.5 counts/s. Other MS and NGR peaks within the sediment interval each correlate to a ~2 cm volcaniclastic layer at ~98 mbsf (MS = $150 \times 10^{-5}$ SI; NGR = 10.1 counts/s; Section 11R-3) and ~123 mbsf (MS = $145 \times 10^{-5}$ SI; NGR = 18.8 counts/s; Section 13R-6). In Hole U1576A, peaks in NGR, MS, and Section Half Multisensor Logger (SHMSL) logs align with discrete turbidite or altered tuff layers from ~95 to 280 mbsf, and all three data sets display a broad cyclical trend over the same interval. In Hole U1576B, MS values are uniformly low in the upper chalk layer and interbedded limestones, with an overall mean value of $15.8 \pm 24.8 \times 10^{-5}$ SI, but NGR counts in interbedded chalk and limestone below the uppermost sediment/basalt contact increase with depth from 4.31 counts/s at 387 mbsf to 30.2 counts/s at 441 mbsf. Basalt layers in Hole U1576B show an increase in MS to an overall mean of $986 \pm 171 \times 10^{-5}$ SI. Relatively high NGR and MS/MSP values in Hole U1576B may be related to pervasive alteration in interbedded sedimentary and basalt units. Similar trends in MS and GRA bulk density values at ~371 mbsf (MS = $8.55 \times 10^{-5}$ SI; NGR = 18.5 counts/s) in Hole U1576A and at ~374 mbsf (MS = $8.84 \times 10^{-5}$ SI; NGR = 18.8 counts/s) in Hole U1576B correlate to a volcaniclastic deposit at the same depth in each hole. This correlation suggests that Holes U1576A and U1576B may sample a common stratigraphic sequence from the seafloor to ~451 mbsf.

## 5.3. Site U1577

### 5.3.1. Background and objectives

Site U1577 (proposed Site VB-13A) is located on the extreme eastern flank of Valdivia Bank as a complement to Sites U1575 and U1576 on the western and northern sides of the edifice, respec-

tively (Figures **F1**, **F23**). The site was selected to recover igneous basement samples from a buried part of the plateau to understand its geologic and geochemical evolution in a location that can only be sampled by drilling (Figure **F24**). Samples from Site U1577 will help determine whether the isotopic zonation, observed several hundred kilometers farther southwest in the TGW hotspot track, is found at Valdivia Bank. Geochronology studies of basalts from Site U1577, along with those from other Valdivia Bank sites, will constrain the temporal evolution of the plateau. Specifically, is there a north–south age progression, as predicted by hotspot models, or is the progression east–west, as predicted by plume-ridge interaction? Paleomagnetic studies of Site U1577 basalts will add to those from other sites to examine the paleolatitude of the hotspot during the Late Cretaceous. Studies of the sedimentary overburden will add to those from previous sites to understand the sedimentary and paleoenvironmental history of Valdivia Bank.

## 5.3.2. Operations

A single hole was drilled at Site U1577 (Table **T1**). Hole U1577A is located at 25°12.1439′S, 7°29.8140′E, at a water depth of 3940.2 m as obtained from the PDR. In Hole U1577A, we used the RCB coring system to advance from the seafloor to a final depth of 193.9 mbsf and recovered 152.9 m (79%) of sediment and igneous rock. In total, Hole U1577A penetrated 39.1 m of igneous basement. Coring was terminated early to complete the remaining major objectives of the expedition. The total time spent on Hole U1577A was 109.5 h, or 4.6 days.

## 5.3.3. Principal results

### 5.3.3.1. Sedimentology

The sedimentary deposits at Site U1577 are divided into three lithostratigraphic units that range in age from the Paleocene (Thanetian) to Upper Cretaceous (latest Santonian). The sediments consist of a ~155 m thick succession of nannofossil ooze and chalk with variable contents of clay and volcanic tephra (Figure **F25**). This sedimentary succession overlies the igneous basement, which consists of three massive lava flows (4, 12, and 19 m thick) devoid of sedimentary intercalation or infillings (Figure **F26**). The lithostratigraphic division was defined based on macroscopic and microscopic lithologic observations supplemented with changes in NGR and biostratigraphic data. Three units of pelagic sediment with a minor component of tephra layers were defined (Lithostratigraphic Units I–III) (Figure **F25**). Sediment consolidation increases gradually downhole, with ooze dominant in Unit I and chalk dominant in Units II and III. Drilling disturbance occurs throughout the ooze of Unit I where the cores commonly display uparching of the bedding

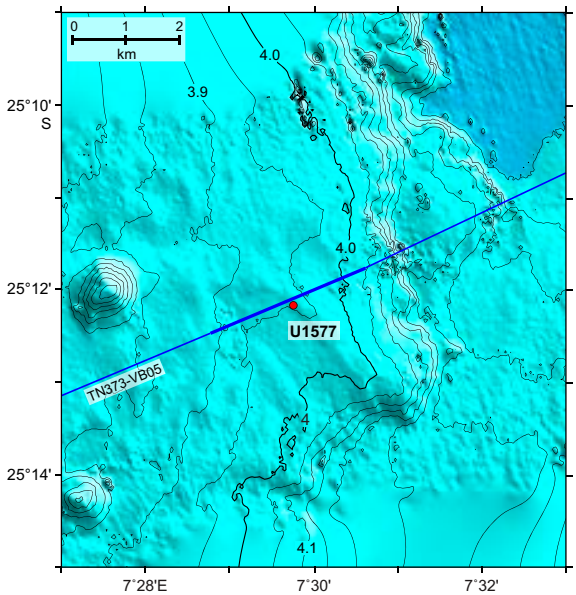


**Figure F23.** Bathymetry of Site U1577 and environs. Detailed multibeam bathymetry around Seismic Line TN373-VB05 is merged with the SRTM15+ bathymetry grid (Tozer et al., 2019). Contours are plotted at 50 m intervals and labeled in kilometers. Blue line = Seismic Line TN373-VB05, heavy blue line = portion of the seismic line shown in Figure F24.

(i.e., beds form an inverted U). The increased consolidation in the sediment deeper in the hole offers better preservation of sedimentary detail, with disturbance limited to less consolidated intervals where localized biscuiting and minor uparching of the bedding occur. Consistent with the increase in sediment consolidation downhole, core recovery is ~69% in Unit I (0–46.90 mbsf), ~90% in Unit II (46.90–70.72 mbsf), and ~82% in Unit III (70.72–154.80 mbsf).

Unit I is a 46.90 m thick Paleocene succession of unconsolidated pale brown to white bioturbated nannofossil ooze with clay. It is irregularly interbedded with minor, brown, altered volcanic ash layers containing sparse crystals of feldspar, biotite, and amphibole. A marked decrease in clay content and tephra abundance occurs between ~11 and 24 mbsf, producing an interval of distinctively lighter sediment. The more clayey ooze intervals at the top and bottom of the unit display light brown to brown 10–50 cm thick cycles, and the lowest 3 to 4 m have an increasingly pink hue and show ferromanganese layers disaggregated by drilling. Because tephra changes reflect phases of increased volcanic input rather than changes in background pelagic sedimentation, they were not used for stratigraphic division. Instead, the lower boundary of the unit was based on paleontological data supporting a transition to Upper Cretaceous microfossil assemblages in the underlying units.

Unit II is a ~23.82 m thick (46.90–70.72 mbsf) Upper Cretaceous (Maastrichtian) succession of slightly to heavily burrowed pinkish brown to pale brown clayey nannofossil ooze to chalk with minor interbeds of brown to gray ash to tuff, both of which are commonly altered. The K/Pg

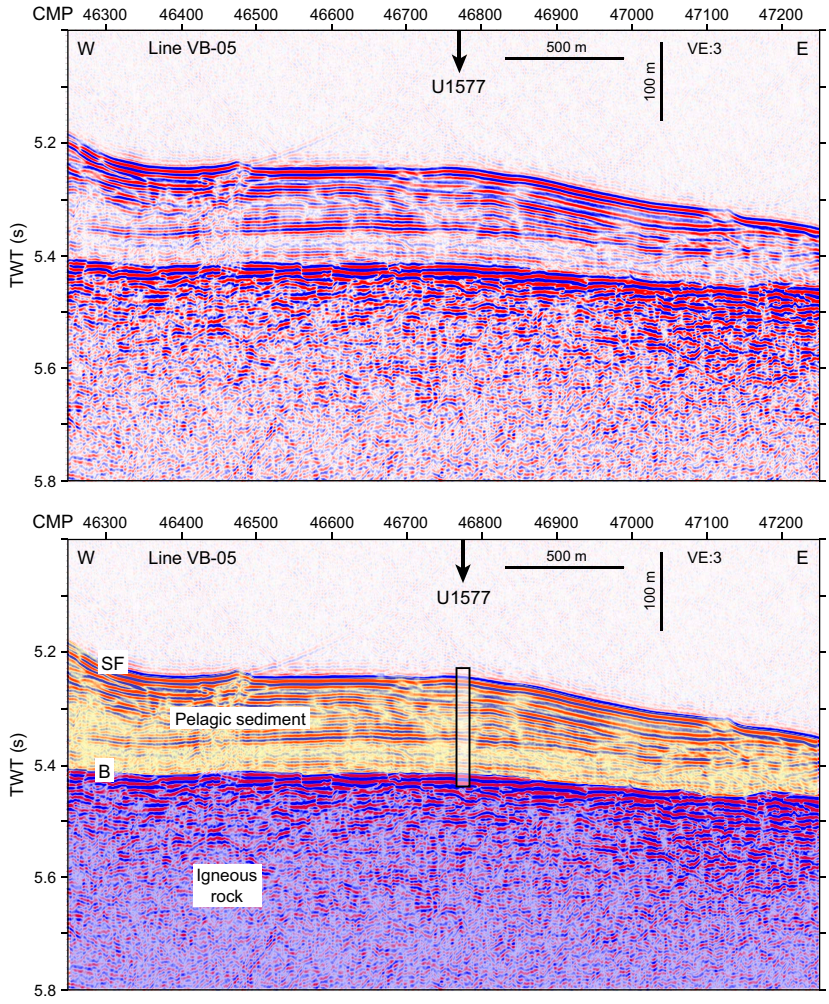


**Figure F24.** Seismic Line TN373-VB05 over Site U1577. Top: uninterpreted seismic data. Bottom: seismic line interpretation. Box = location and approximate depth of Site U1577. Seismic line location shown in Figure F23. TWT = two-way traveltime, VE = vertical exaggeration.

boundary, which is assumed to form the boundary between Units I and II, was not recovered. Unit II differs from Unit I in that clay content (i.e., brown color) remains high throughout. In addition, Unit II lacks the black ferromanganese layers seen in the lower part of Unit I, and it records the first appearance of inoceramid shell fragments downhole. The pelagic sediment of Unit II is characterized by cyclical changes in color at a 10–60 cm scale that most likely correspond to fluctuation in the relative abundance of clays and Fe oxides relative to carbonates. At least 20 layers of typically well-defined, brown to dark brown, graded and/or bioturbated tephra occur throughout. The lower boundary of Unit II is taken as the base of the lowermost graded tephra layer, below which both biostratigraphic and paleomagnetic data suggest a stratigraphic gap or period of reduced sedimentation of ~3 My.

Unit III represents over half (84.08 m) of the sedimentary cover (70.72–154.80 mbsf). It is a Campanian to possibly latest Santonian succession of bioturbated clayey nannofossil chalk with intermittent, commonly burrowed graded tephra interbeds. Overall, Unit III represents a long duration of seafloor pelagic sedimentation interspersed with tephra input of differing types. Changes in color at a 10–60 cm scale, similar to those observed in Unit II, are locally recognized in Unit III, but these are more commonly obscured by irregular occurrences of slightly to extensively bioturbated tephra layers. Unit III is further divided into three subunits (IIIA–IIIC) based on color variation (pinkish to green) that reflects clear variations in the overall preserved oxidation state in the chalk and also based on attendant changes in the abundance and type of tephra deposits. Subunit IIIA is a 22 m thick succession (70.72–92.23 mbsf) dominated by pinkish brown chalk with minor gray tephra layers typically <5 cm thick. Subunit IIIB is a ~41 m thick succession (92.23–133.53 mbsf) dominated by greenish gray chalk with slightly more abundant black tephra layers (~5–15 cm thick). Finally, Subunit IIIB is a 21 m thick succession (133.53–154.80 mbsf) dominated by pinkish brown chalk with fewer intervals of gray, brown, and black tephra layers (also ~5–15 cm thick). Rare <15 cm thick layers of hyaloclastite appear toward the base of the unit closer to the contact with underlying volcanic basement. This contact is marked by the top of a massive lava overlain by a 0.5 cm thick layer of altered hyaloclastite and bioturbated clayey nannofossil chalk.

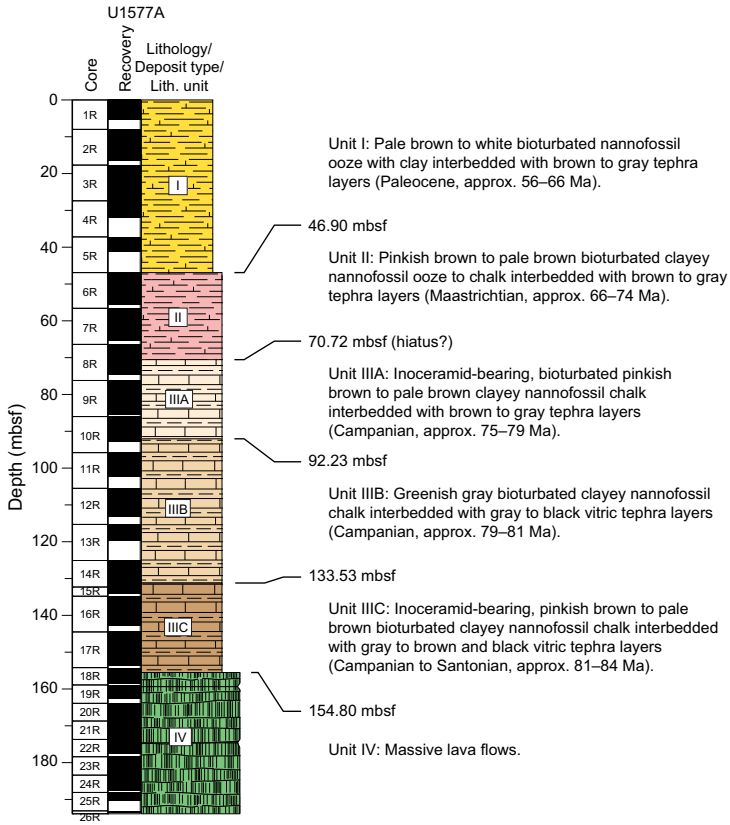


**Figure F25.** Lithostratigraphic summary, Site U1577.

As previously observed in the sedimentary cover at Site U1576, Unit III at Site U1577 preserves a detailed record of changes in paleoenvironment at Valdivia Bank (e.g., either cyclical patterns and possible anoxic versus oxic seafloor conditions or depositional diagenesis) for the Campanian and Maastrichtian.

### 5.3.3.2. Igneous petrology and volcanology

Hole U1577A penetrated 39.1 m of igneous basement, recovering 28.0 m of igneous rocks (80%) representing Lithostratigraphic Unit IV in the overall subseafloor succession (Figure **F26**). Hole U1577A terminates within a massive basalt flow with a minimum thickness of 19.07 m. Igneous basement was intersected in Sections 391-U1577A-18R-1 through 26R-1. The volcanic succession consists of a single unit (Igneous Unit 1) made up of highly phyric basalt that is divided into three subunits (i.e., massive lava flows) based on features which identify flow boundaries (Figure **F26**). All igneous subunits are porphyritic; the groundmass texture grades to aphanitic adjacent to flow boundaries. The uppermost subunit contains a glassy rim in contact with the overlying pelagic sediment. The phenocryst concentrations are ~18% in the massive flows, with ~15% plagioclase, 2%–5% pyroxene, and 0%–3% olivine. The lavas are slightly vesicular and contain round vesicles that are 1–2 mm in diameter and filled with at least one secondary mineral (e.g., clay, calcite, and/or zeolite). The groundmass in flow interiors consists of fine- to medium-grained clinopyroxene and plagioclase in subophitic textures, often showing late-stage crystallization after olivine and plagioclase. In flow interiors, the groundmass has a seriate texture and coarse crystal size distribution that approaches that of the phenocrysts. Mesostasis (quenched melt) forms irregular globules that consist of microcrystalline plagioclase, clinopyroxene, and Fe-Ti oxides. The flow margins consist of plagioclase-clinopyroxene-olivine phyric basalt. Plagioclase is still the dominant phenocryst phase in the form of similarly blocky or tabular glomerocrysts (up to 2.4 mm in size) but with much lower abundance than in flow interiors (~5%). Olivine (typically altered to

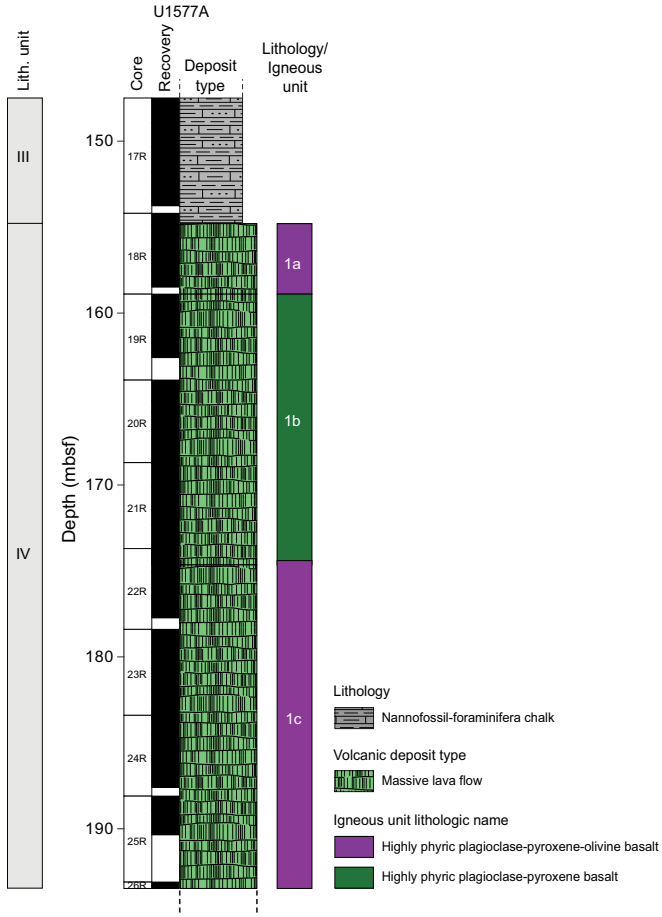


**Figure F26.** Stratigraphic column for igneous basement, Hole U1577A.

saponite) and clinopyroxene are less common and form small anhedral grains (up to 0.6 mm). The groundmass in samples from flow margins is markedly distinct from flow interiors; plagioclase, clinopyroxene, and Fe-Ti-oxides are very fine grained, showing intergranular textures. Plagioclase forms small needle-like skeletal crystals (<0.4 mm), whereas clinopyroxene (<0.08 mm) forms small blocky crystals. There is no seriate gradation in size, as seen in the flow interiors. Mesostasis forms distinct regions with microcrystalline textures. Secondary minerals are relatively scarce, but those that do occur are disseminated as limited peripheral alteration or oxidative films around crystals, and these changes impart minor color variations from the unaltered blue-gray flow interiors to a light brown hue. Oxidative changes also occur as discolored halos extending 2–4 cm away from calcite- and Fe oxyhydroxide–filled fractures and veins.

#### 5.3.3.3. Biostratigraphy

Calcareous nannofossil and planktonic foraminifera biostratigraphy were performed on core catcher sections from Hole U1577A. Nannofossil analysis included 15 core catcher samples and two toothpick samples, and foraminifera analysis included seven core catcher samples. Foraminifera sample processing was difficult, limiting the number of samples analyzed in the time available for this hole. Planktonic foraminifera and calcareous nannofossil ages show good agreement throughout the hole.

Notably, Section 391-U1577A-1R-CC recovered sediments that were late Paleocene (Thanetian; ~58.0 Ma). Therefore, the shallowest possible sample (i.e., the mudline) was examined to determine whether this age also corresponds to the top of the sequence or a thin layer of younger sediment was present. Investigation of the mudline revealed sediments with a maximum age of latest Pleistocene, indicating present-day sedimentation is not below the carbonate compensation depth. This likely indicates a long persistent erosional surface at this site; thus, a major unconformity exists between sediments younger than ~0.43 Ma and the latest Paleocene-aged sediments recovered in Core 1R. Additional samples from this core will be analyzed postexpedition to identify the precise location of this unconformity. A nearly continuous succession of upper Paleocene (Thanetian) to Upper Cretaceous (Campanian) sediment was recovered in Sections 1R-CC through 17R-CC. An apparent unconformity was discovered between Sections 7R-CC and 8R-CC, spanning the Maastrichtian/Campanian boundary and encompassing a time gap of about 5.6 My between ~69.0 and 74.6 Ma. This observation is corroborated by NGR data measured on whole-round sections and magnetostratigraphic data. Higher resolution sampling through Core 8R is required to identify the true range of missing time due to this unconformity.

The age of the oldest sediment in Hole U1577A is unclear. Foraminifera and calcareous nannofossils do not record Santonian (Upper Cretaceous) marker taxa. However, paleomagnetic data indicate that the interval of the Cretaceous Normal Superchron was intersected (possibly in Section 17R-3), which is considered to be the boundary between the Campanian and Santonian stages of the Upper Cretaceous. In Section 17R-CC, foraminifera and nannofossils agree on an early Campanian age from ~79.00 to 81.38 Ma. However, the poor preservation of planktonic foraminifera limited the complete evaluation of the assemblage. A toothpick sample was taken from just above the sediment/basement contact, but confident Santonian markers were not observed. Last occurrences of foraminifera markers *Dicarinella asymetrica*, *Dicarinella concavata*, and *Sigalia deflaensis* coincide with the Santonian/Campanian boundary (83.64 Ma) (Gradstein et al., 2012).

#### 5.3.3.4. Paleomagnetism

Sedimentary Cores 391-U1577A-1R through 18R are mostly made up of partially to fully consolidated clay and chalk. Archive-half sections and discrete samples were analyzed using the SRM and JR-6A spinner magnetometer, respectively. Natural remanent magnetization (NRM) values for sediments range $10^{-3}$ to $10^{-1}$ A/m. Most sediments have median destructive fields ranging 10–30 mT. Thermal demagnetization spectra of sediment specimens often revealed slow unblocking of magnetization in the 200°–400°C range, with a sharper drop in magnetic moment close to 580°C (the Curie temperature of magnetite). This demagnetization behavior suggests that the dominant magnetization carriers in sediments from Hole U1577A are likely a mixture of titanomagnetite with varying Ti concentrations and magnetite. A total of eight polarity chrons were identified in these sections that cover the Thanetian (late Paleocene; Chron C26n in Core 1R) to the early Santonian (Late Cretaceous; Chron C34n near the contact with basement). The three major breaks in

the magnetostratigraphy are probably due to poor core recovery or unconformities: (1) between Cores 4R and 5R, where sediment ages jump from Chron C26r to Chron C28n; (2) between Cores 5R and 6R, where sediment ages jump from Chron C28n to Chron C30n; and (3) in Section 8R-3, where sediment ages jump from Chron C31r to Chron C33r. All of these gaps are consistent with the available biostratigraphic markers for these cores.

Igneous rocks recovered from Site U1577 span Cores 391-U1577A-18R through 26R. Their NRM values range from slightly below 1 to slightly above 10 A/m. Nearly all igneous cores displayed a positive polarity magnetization after AF cleaning to 20 mT, which is compatible with the assignment of polarity Chron C34n (Cretaceous Normal Superchron) observed in the sediments above the sediment/basalt contact. Occasionally, basalts from sections with large hydrothermal veins exhibited reversed polarity, which likely reflects secondary remagnetization due to alteration. Most of the igneous rocks had median destructive field values between 5 and 25 mT and exhibited a range of thermal demagnetization behaviors. Some igneous specimens exhibited lower maximum unblocking temperatures around 200°C, whereas others showed higher unblocking temperatures near the magnetite Curie temperature of 580°C. The remainder of specimens progressively lost their magnetization between 100° and 350°C. This wide range of thermal demagnetization behaviors implies the coexistence of several magnetic phases, including pseudo-single domain to multidomain magnetite and titanomagnetite with a large range of Ti concentrations.

#### 5.3.3.5. Geochemistry

At Site U1577, IW samples were analyzed for pH, alkalinity, and concentrations of major cations, anions, and trace elements. Both alkalinity and pH show narrow ranges except for low alkalinity and high pH anomalies observed within Lithostratigraphic Subunit IIIB. Across the entire sedimentary succession, overall nonlinear increases of calcium and decreases in magnesium are observed with low concentration anomalies within Subunit IIIB. A broad peak of potassium concentration is also found in Subunit IIIB, whereas the potassium concentration is uniform in Unit I through Subunit IIIA. Similar to Site U1576, two maxima of silicon concentration are found at the top and bottom of the sediment succession, indicating dissolution of biogenic silica and volcanic matters, respectively. A broad manganese peak is identified in Subunit IIIB, coinciding with alkalinity, pH, calcium, magnesium, and potassium anomalies. We observe an overall decrease of sulfate concentration throughout the entire sediment succession. A narrow phosphate peak is found in the upper part of Unit I with a linear increase below this depth. Compared to previous sites, ammonium and phosphate concentrations are significantly lower at Site U1577 with a molar ratio of 1:1. In summary, IW geochemistry at Site U1577 indicates slower diageneses of calcite, silica, and organic matter than at the other Valdivia Bank sites (U1575 and U1576). Sediment samples were also analyzed for the $CaCO_3$, total carbon, and total organic carbon content. $CaCO_3$ content declines in Unit III, whereas organic carbon content is relatively consistent in the overall sedimentary sequence. Methane concentrations measured from the headspace gas are lower than the atmospheric background level of 2.0 µL/L.

Three igneous subunits of massive lava flows consisting of highly phyric basalt were recovered at Site U1577. Seven samples were analyzed for major and trace elements using ICP-AES. Additionally, 50 measurements were conducted on archive-half section pieces using pXRF spectrometry. The analyzed samples show a low LOI of <1.35 wt%, indicating relatively fresh submarine rocks. Overall, Site U1577 samples are extremely homogeneous, showing limited geochemical variation downhole that is less variable in composition than the other Valdivia Bank sites (U1575 and U1576). Based on the low LOI and homogeneous composition, we conclude that the brownish discoloration of some samples reflects minor oxidation without significant element mobilization. All samples from Site U1577 are classified as basalts and have a tholeiitic composition. The Ti-V composition of the basalts is similar to the other Valdivia Bank sites and is comparable to MORBs and ridge-centered ocean island basalts. On bivariate diagrams of Mg# versus the other major and trace elements, Site U1577 samples form tight clusters that overlap with previous dredge and DSDP drill site samples from Walvis Ridge. Consistent with the absence of olivine, olivine-free Igneous Subunit 1b is slightly lower in MgO, Mg#, Ni, and Cr relative to Subunits 1a and 1c.

#### 5.3.3.6. Physical properties

Physical properties measurements were made on whole-round cores, section halves, and discrete samples from 26 cores recovered from Hole U1577A. A suite of measurements, including NGR, MS/MSP, bulk density, *P*-wave velocity, porosity, and thermal conductivity record two lithostratigraphic breaks: (1) a boundary between calcareous ooze/chalk units at ~70 mbsf and (2) the sediment/basalt contact at ~155 mbsf. The first lithostratigraphic boundary, between Lithostratigraphic Unit II and Subunit IIIA, is defined by an abrupt shift from relatively high, wide-ranging NGR values to a narrower and lower range of values (~10 to ~16 counts/s) at ~70 mbsf. At the same depth, NGR observations are correlated to paleomagnetic measurements: remanent magnetism indicates a shift from Chron C31n to Chron C33r and suggests that part of the sedimentary record is missing. The sediment/basalt contact is clearly imaged at ~155 mbsf as an increase in MS/MSP and bulk density (up to 2709 × $10^{-5}$ SI and 2.95 g/cm$^3$, respectively) and an accompanying decrease in porosity and NGR counts (as low as 2.73 vol% and 4.98 counts/s, respectively). Sediments above the basalt contact have comparably lower MS/MSP and bulk density (up to 647 × $10^{-5}$ SI and 2.12 g/cm$^3$, respectively) and higher NGR and porosity (up to 31.3 counts/s and 73.2 vol%, respectively). Bulk density, MS/MSP, and NGR values indicate a continuous package of relatively unaltered basalt with no interbedded sediments from ~155 mbsf to the bottom of Hole U1577A at 193.4 mbsf. Physical properties measurements also record lithologic variations within the sediment interval that align with observations from previous sites. As in Holes U1576A and U1576B, higher MS/MSP values (e.g., 647 × $10^{-5}$ SI in Section 391-U1577A-8R-3; ~71 mbsf) are associated with volcaniclastic deposits within the sediment interval. Additionally, sediments between ~80 and ~90 mbsf appear to display cyclic variations in NGR that are similar to cycles observed in Hole U1576A.

## 5.4. Site U1578

### 5.4.1. Background and objectives

Site U1578 (proposed Site CT-5A) is the westernmost drilling location for Expedition 391 (Figure **F1**), and it is the youngest, with an expected age either in the latest Cretaceous or earliest Paleocene (Figure **F5**). It is the only Expedition 391 site in the morphologically distinct Guyot Province. It is located on the lower flanks of a Center track guyot where sediments are thin (Figures **F27**, **F28**, **F29**). With >300 m of igneous basement cored, it is also the deepest basement penetration site of Expedition 391. The site was chosen because the erupted lavas are either likely to be a mixture of Tristan- and Gough-type components or to constitute a distinct third isotopic signature. A major objective for this site was to measure the geochemical composition of samples from a deep downhole section of lava flows. The geochemistry should offer clues to the magma source and evolution of the Center track ridge. Although there are already many radiometric dates for Walvis Ridge seamounts, samples from Site U1578 help fill gaps in prior sampling. The expected age for Site U1578 basement is a propitious time for understanding the paleolatitude changes of the TGW hotspot because global paleomagnetic data sets suggest that the paleolatitude for the latest Cretaceous and earliest Paleocene TGW hotspot location was south of its current latitude, implying northward motion. In contrast, hotspot drift models imply the opposite sense of motion. Moreover, the sense of motion may be opposite to the Hawaiian hotspot, which would confirm TPW. Although the location of Site U1578 was selected to minimize sediment cover, the sedimentary sequence is expected to provide insights into paleoceanographic conditions at Walvis Ridge during the Cenozoic.

### 5.4.2. Operations

A single hole was drilled at Site U1578 (Table **T1**). Hole U1578A is located at 32°19.6836′S, 0°38.5876′W at a water depth of 3793.8 m as obtained from the driller's tag depth. In Hole U1578A, we used the RCB coring system to advance from the seafloor to a final depth of 486.4 mbsf and recovered 239.9 m (49%) of sediment and igneous rock. The total advance in Hole U1578A required the deployment of two RCB coring bits through a bit change and reentry into the hole. In total, Hole U1578A penetrated 302.1 m of igneous basement. The total time spent on Hole U1578A was 244.0 h, or 10.2 days.

## 5.4.3. Principal results

### 5.4.3.1. Sedimentology

A ~184 m thick succession of calcareous pelagic sediment interbedded with volcaniclastic layers lies on top of the volcanic basement (Figure **F30**). Two main lithostratigraphic units, the second divided into two subunits, were recognized based on macroscopic and microscopic (smear slide, thin section, and scanning electron microscopy) lithologic observations along with changes in MS, NGR, and biostratigraphic data. These overlie the igneous succession, which consists of lava stacks intercalated with 10 sedimentary interbeds.

Unit I forms the uppermost 27 m of the sedimentary cover (Figure **F30**). It consists of Pleistocene to Pliocene white to pale brown foraminifera-nannofossil ooze with clay. Significant drilling disturbance occurs throughout due to poor consolidation of this pelagic sediment, but almost complete (99%) recovery was achieved. A mass transport deposit occurs toward the boundary with Unit II in Section 391-U1578A-3R-6. The boundary itself is marked by the appearance of tephra and a gradual clay increase in the calcareous ooze/chalk downhole, which correlates with an increase in MS and NGR values and the occurrence of Eocene–Paleocene foraminifera and nannofossil assemblages, indicating a significant stratigraphic gap.

Unit II is a ~157 m thick succession of mostly Paleocene calcareous pelagic sediment with rare volcaniclastic deposits that becomes progressively more consolidated with depth (Figure **F30**). Relatively limited (<40%) recovery in this unit probably occurred due to significant heave during drilling. Two subunits (IIA and IIB) were defined based on changes in clay content and NGR values. Subunit IIA is early Eocene to Paleocene in age (27.00–135.20 mbsf). It consists of white to

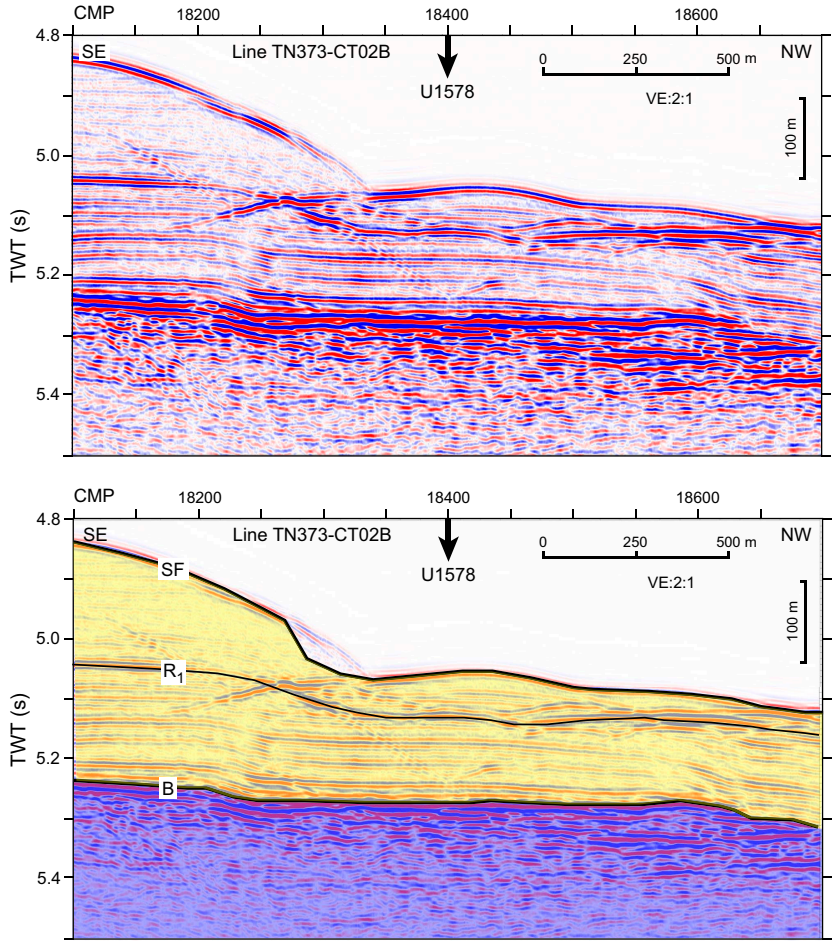


**Figure F27.** Seismic Line TN373-CT2B over Site U1578. Top: uninterpreted seismic profile. Arrow = location of Site U1578. Bottom: seismic line interpretation. TWT = two-way traveltime, VE = vertical exaggeration.

pale pinkish brown nannofossil ooze to chalk with clay and rare radiolarians, siliceous sponge spicules, and small foraminifera. The unit also includes minor (commonly disturbed) interbeds of light to dark gray tephra with colorless to light brown highly vesicular volcanic glass and pumices. Subunit IIB is Paleocene in age (135.20–184.26 mbsf) and continues to the top of the underlying volcanic succession. It consists of light gray to greenish gray clayey nannofossil chalk with rare radiolarians, siliceous sponge spicules, and small foraminifera. The chalk lithology is darker and more clayey than that of Subunit IIA, consistent with a gradual increase in NGR in the lower part of the sedimentary cover. Subunit IIB also includes minor interbeds of dark greenish gray to black vitric sandstone/tuff with normal grading that increase in abundance toward the top of the volcanic basement. Volcanic glass shards in the dark sandstone/tuff are fresh to altered with highly vesicular to pumiceous textures, but they are distinctively browner than the glass shards of Sub-

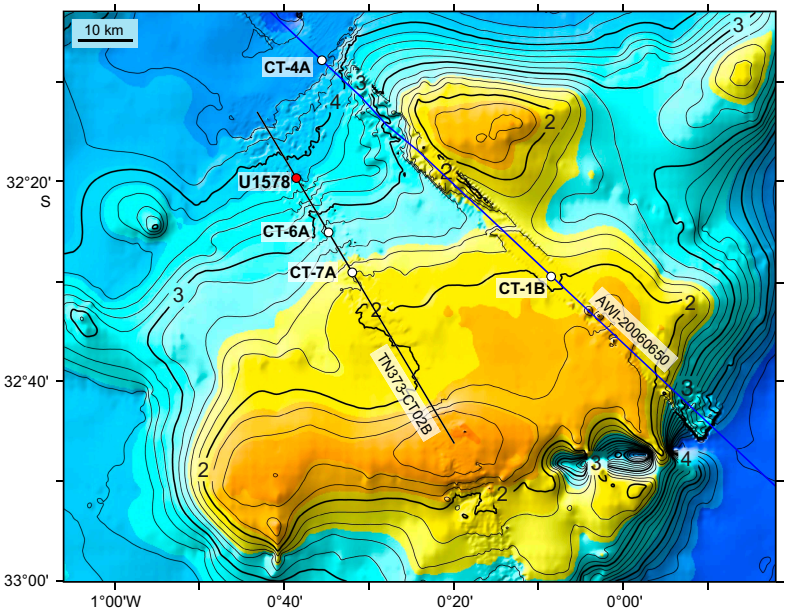


**Figure F28.** Bathymetry map of Site U1578 and environs. Detailed multibeam bathymetry around Seismic Line TN373-CT2B is merged with the SRTM15+ bathymetry grid (Tozer et al., 2019). Contours are plotted at 50 m intervals and labeled in kilometers.

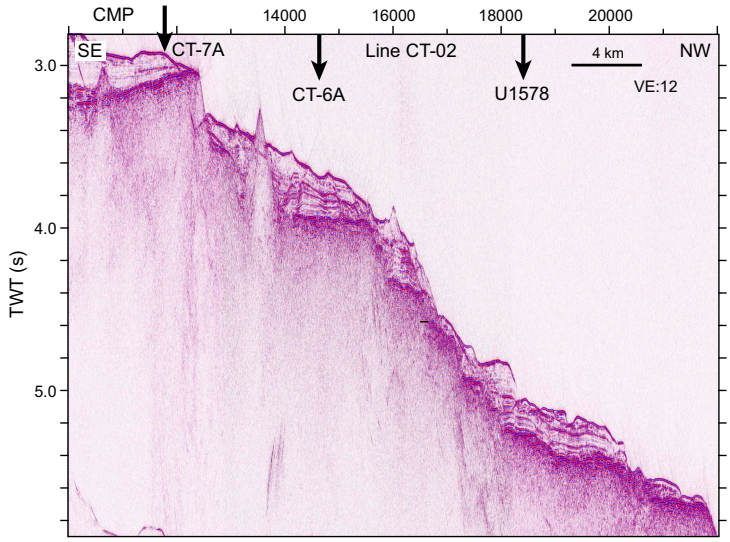


**Figure F29.** Section of Seismic Line TN373-CT2B showing the northwest flank of the Center track guyot. Arrows = locations of Site U1578 and proposed alternate Sites CT-6A and CT-7A. VE = vertical exaggeration.

unit IIA. The texture of the tephra and sedimentary structures of volcaniclastic beds suggest shallow marine and possibly subaerial volcanism with synvolcanic deposition during pelagic fallout and/or syn- to postvolcanic reworking by turbidity and/or bottom currents.

This sedimentary succession overlies the igneous basement, which consists of 12 igneous units. These units consist of massive flows alternating with thick pillow lava stacks, with rare peperitic intervals and 10 sedimentary interbeds (Figure **F31**). These interbeds vary in thickness between approximately >0.5 and >10 m and occur down to 416.87 mbsf. They are lithologically similar to the lowermost sedimentary cover and are composed of clayey nannofossil chalk with volcaniclastic layers. The volcaniclastic deposits typically consist of turbidites with variably altered vitric clasts. The glass shards are highly vesicular in the uppermost six sedimentary intervals and become less vesicular in the lower part of the hole.

### 5.4.3.2. Igneous petrology and volcanology

Hole U1578A penetrated 302.12 m of igneous basement (interval 391-U1578A-20R-1, 46 cm, through 65R-3, 45 cm) with 181.26 m (59.9%) recovery. The igneous basement at Site U1578 represents Lithostratigraphic Unit III in the overall subseafloor succession (Figure **F31**). Hole U1578A terminates in a pillow lava unit with a minimum thickness of 67 m. Twelve igneous units were identified in Hole U1578A (Figure **F31**). They comprise pillow and lobate lava flows, sheet flows, and massive flows with interbedded sediments. The changing eruptive style, changes in chemistry, and pelagic sediment interbeds suggest episodic volcanic activity. The uppermost 96 m of the succession consists largely of sheet and massive flows intercalated with volcanic sands and silts; pillow lava flows are present in thin sequences. One massive flow is distinguished by a zone of olivine accumulation in the lowermost 1 m, with up to 25% modal olivine. Below that, the dominant unit comprises 96 m of continuous pillow basalt followed by 109 m of pillow lava with two massive flows and one 6.3 m thick sediment horizon. Glass rims are preserved on many pillow margins. The massive flows can be quite voluminous; one massive basalt unit is at least 14.9 m thick. The lavas range from highly phyric (~8%–15% plagioclase, 0%–4% olivine, and 1%–3%

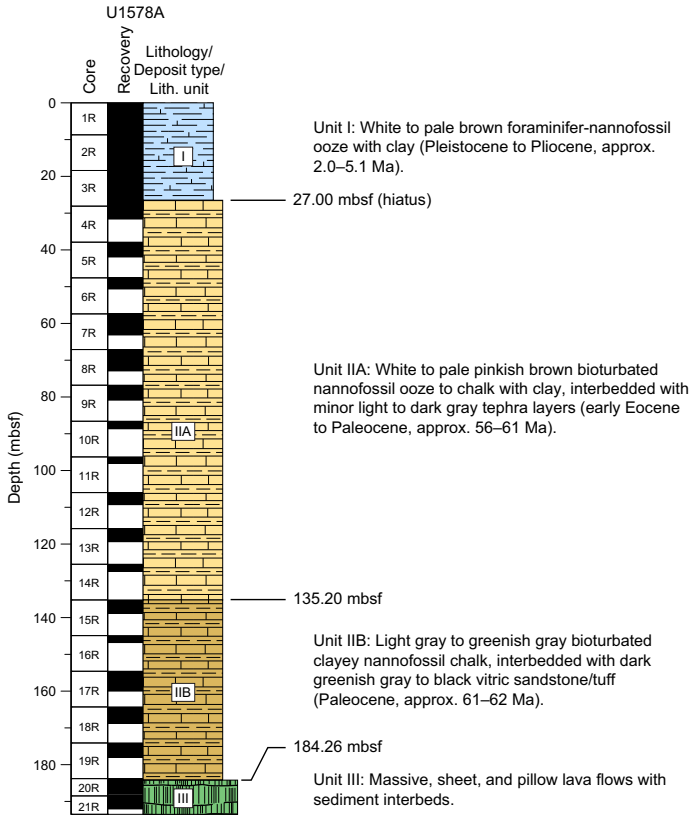


**Figure F30.** Lithostratigraphic summary, Hole U1578A.

pyroxene) to sparsely phyric or aphyric basalts. In highly phyric lavas, plagioclase phenocrysts and glomerocrysts can be up to 15 mm in diameter; pyroxene and olivine are generally much smaller (1–3 mm). Thicker massive units present relatively fresh rock, and pillow units are pervasively altered except for very fine-grained pillows, which preserve primary modal compositions in their interior. The vesicular and fractured nature of pillow lava stacks lends themselves to mineralization in the form of vesicle infilling and veins in fractures. The nature of this alteration changes downhole through the succession with carbonate and calcite, together with Fe oxyhydroxide dominating the upper igneous units and pyrite (marcasite), and associated Cu-bearing coatings and zeolite infillings, becoming more common downhole. Farther within the volcanic sequence there is distinctive epidote mineralization along fractures and within pillow lava vesicles.

### 5.4.3.3. Biostratigraphy

Preliminary calcareous nannofossil and planktonic foraminifera biostratigraphy was conducted on core catcher sections from Hole U1578A. A preliminary chronostratigraphic framework for sediments in this hole was obtained from the stratigraphic distribution of the investigated microfossil groups, referring to biozonations based on Gradstein et al. (2012, 2020). Calcareous nannofossil analysis was conducted on 18 core catcher sections and on 10 toothpick samples taken from within core sections. Planktonic foraminifera were analyzed in a total of 10 core catcher samples to provide additional key age controls. Foraminifera sample preparation required the use of hydrogen peroxide (30%) to disaggregate lithified sediments, which limited the time available for shipboard analysis. Overall, calcareous nannofossils and planktonic foraminifera are in good agreement at Site U1578.

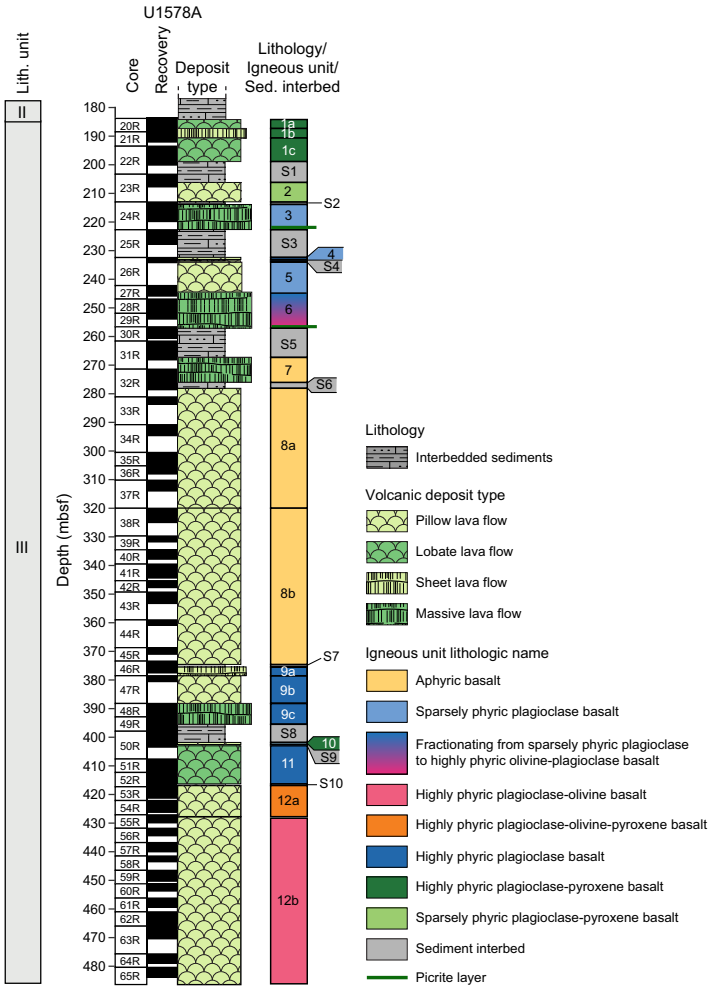


**Figure F31.** Stratigraphic column for igneous basement, Hole U1578A.

Calcareous nannofossils show good preservation and high abundances throughout Hole U1578A. Planktonic foraminifera are well preserved and abundant in the upper part of the stratigraphic sequence (Sections 1R-CC and 2R-CC; Lithostratigraphic Unit I). Conversely, foraminifera abundances decrease downhole (Sections 3R-CC through 18R-CC) where an increase in radiolarians was noted. Moreover, planktonic foraminifera show a decrease in test size in the same time interval, which possibly indicates a response to environmental stress. Sections 1R-CC and 2R-CC record late Pliocene (Piacenzian) to Pleistocene (<0.43 Ma) sediments. Toothpick samples for calcareous nannofossil analysis were taken from Section 2R-5 to investigate a lithologic change that was thought to be an additional age horizon. The examined samples revealed the presence of Oligocene and Eocene flora mixed with Gelasian (early Pleistocene) assemblages. The occurrence of older taxa within the Pleistocene deposits may be indicative of sediment remobilization (e.g., slump/landslide). The existence of a major unconformity between early Pliocene (Zanclean) and Paleogene deposits at ~27.0 mbsf was confirmed by both calcareous nannofossil and planktonic foraminifera data. A shift in MS and magnetic remanence values was also observed from the same depth interval, supporting the presence of the unconformity. Sections 3R-CC through 18R-CC recovered a continuous Paleogene stratigraphic sequence. Uncertainties in the placement of the Eocene/Paleocene boundary derived from the analysis of calcareous nannofossil and planktonic foraminifera assemblages. Planktonic foraminifera data indicate a mix of early Eocene (Ypresian) and late Paleocene (Thanetian) taxa in Section 3R-CC. Calcareous nannofossils suggest a possible early Eocene age for the same sample because the late Paleocene marker *Ericsonia robusta* (56.78 Ma) is not observed until Section 5R-CC. The bottommost section (18R-CC), at the sediment/basement contact, is dated between 61.98 and 62.07 Ma based on calcareous nannofossils. Planktonic foraminifera suggest a possibly older age (62.2–63.5 Ma), but this date is considered unreliable due to the scarce abundance of foraminifera specimens in the section.

Interbedded sediments within the basement section were investigated using calcareous nannofossils. Preliminary shipboard analyses indicate a possible age of ~63.25–64.81 Ma. However, high-resolution postexpedition examination is required to better evaluate the age of the intercalated sediments. Preliminary biostratigraphic data from the chalk units of the uppermost five interbeds indicate a Paleocene (Danian) age of deposition.

#### 5.4.3.4. Paleomagnetism

Sediment Cores 391-U1578A-1R through 19R consist of ooze to chalk with varying clay content. Archive halves and discrete samples were analyzed using the SRM and JR-6A spinner magnetometer, respectively. Sediment NRM values range $10^{-4}$ to $10^{-1}$ A/m. Most sediments have median destructive fields ranging 30–50 mT. Thermal demagnetization spectra of sediment specimens often revealed slow unblocking of magnetization starting from 200°C and sometimes persisting to 600°C. This demagnetization behavior suggests that the dominant magnetization carriers in sediments from Hole U1578A are likely a mixture of titanomagnetite with varying Ti concentrations, magnetite, and hematite. We did not assign polarity chrons to Cores 1R–3R because there was high dispersion in magnetic inclination values for those cores. However, we were able to assemble a magnetostratigraphy spanning six polarity chrons starting with Chron C24r in Core 4R through the top of Chron C27n in Core 19R, which is located just above the contact with the basement.

Igneous rocks recovered from Site U1578 span Cores 391-U1578A-19R through 65R and primarily consist of basalt. Occasionally, layers of sedimentary rocks or hyaloclastites were observed between basalt flows. The igneous rocks typically have NRM values ranging 1–10 A/m. After AF cleaning to 20 mT, igneous rocks from Cores 20R–45R dominantly displayed a negative inclination magnetization consistent with them having formed during a normal polarity interval. A brief reversed polarity chron in Core 23R could possibly represent Chron C27r (63.5–62.5 Ma), but it could also be attributable to secondary chemical remagnetization or unsuccessful removal of drill string overprints during partial AF demagnetization. Demagnetization of discrete samples from Cores 38R–44R had an unusually high failure rate. Cores 46R–65R dominantly displayed a positive inclination magnetization consistent with formation during a reversed polarity interval. This suggests that at least one geomagnetic reversal is recorded in the eruptive sequence at Site U1578. Most of the igneous rocks have median destructive field values between 5 and 25 mT and exhibit a range of thermal demagnetization behaviors, with maximum unblocking temperatures ranging ~200°–580°C (the Curie temperature of magnetite). This wide range of thermal demagnetization

behaviors implies the coexistence of several magnetic phases, such as magnetite and titanomagnetite with a large range of Ti content.

#### 5.4.3.5. Geochemistry

At Site U1578, IW samples were analyzed for pH, alkalinity, and concentrations of major cations, anions, and trace elements. Both alkalinity and pH show relatively narrow ranges compared to previous sites. Calcium concentration increases downhole to 30 mbsf in Lithostratigraphic Unit I and slowly decreases below this unit, whereas magnesium concentration shows a decreasing trend throughout the sediment succession that is the reverse of the depth trend of potassium concentration. Silicon concentration increases from the top of the sediment to 50 mbsf and maintains high concentrations throughout the lower sediment succession. Lithium concentration decreases within the top 50 m of the sediment succession and remains at the low concentration below ~50 mbsf, showing a trend generally opposite to silicon. We observe a narrow peak of manganese near the top of the sediment in Unit I and a broad peak near the bottom of the sediment in Subunit IIA where iron concentrations are lower than the instrumental detection limit. A nonlinear decrease of sulfate concentration is broadly found in Subunit IIA. Shallow phosphate and ammonium peaks are found at the top of the sediment (2.96 m), and below this depth phosphate and ammonium concentrations are nearly constant. Ammonium and phosphate concentrations at Site U1578 are significantly lower than at Sites U1575 and U1576 but are comparable to Site U1577 with a molar ratio of 0.5:1. In summary, IW geochemistry at Site U1578 is affected by diagenesis of biogenic carbonates at shallow depths and diagenesis of biogenic silica at deep depths. Sediment samples were also analyzed for $CaCO_3$, total carbon, and total organic carbon contents. $CaCO_3$ content declines in Unit II, and organic carbon content is consistently low in the entire sedimentary sequence. Methane concentrations measured from the headspace gas are lower than the atmospheric background level of 2.0 µL/L.

Site U1578 recovered 12 igneous lithologic units of aphyric and phyric basalt lava flows. Sixteen samples from the first eight units were analyzed for major and trace elements using ICP-AES. Additionally, 253 measurements were conducted on archive-half section pieces along the entire igneous section using pXRF. LOI represents an indicator for the degree of alteration, and the analyzed samples show LOI <3 wt%, which is relatively fresh, given that they represent old submarine rocks. All samples from Site U1578 are classified as basalts, except one hawaiite sample, and have an alkalic composition. In contrast to the previously drilled Expedition 391 sites, the Ti-V compositions are comparable to the ocean island basalt array and similar to other alkaline intraplate lavas previously reported from the TGW hotspot track. Based on the $TiO_2$ content, the samples are divided into high-Ti rocks ($TiO_2$ = 3.4–3.9 wt%) and very high–Ti rocks ($TiO_2$ >3.9 wt%). In bivariate diagrams, the major and trace element trends of the high-Ti rocks are generally consistent with olivine, Cr-spinel, and pyroxene fractionation. The very high–Ti rocks are offset relative to the high-Ti rocks to overall higher $TiO_2$, $Fe_2O_3$, MnO, Sc, V, Co, Zn, and Y values, but they have lower $SiO_2$, $Al_2O_3$, and $K_2O$ contents for a given Mg#. Site U1578 represents the longest basement interval drilled during Expedition 391, and significant downhole geochemical variations are observed. The $TiO_2$ content, for example, is relatively low (2.5–3.3 wt%) in the upper part of the recovered igneous succession. In Igneous Unit 8, the rocks are characterized by very high $TiO_2$ values (4.0–4.5 wt%) that decrease to values averaging 3.6 wt% in Unit 9 and then gradually decrease downhole to Units 11 and 12, where $TiO_2$ is comparable to the upper part of the basement succession.

#### 5.4.3.6. Physical properties

Three general lithostratigraphic intervals are identified in Hole U1578A based on physical properties measurements, including NGR, MS, MSP, bulk density, thermal conductivity, *P*-wave velocity, and porosity. The first interval, consisting of calcareous ooze, clay, and chalk, may be divided into upper and lower units based on NGR and MS/MSP values. At ~30 mbsf, a pronounced increase in mean MS/MSP (a shift from $7.39 \times 10^{-5}$ to $17.4 \times 10^{-5}$ SI) and mean NGR (a shift from 3.32 to 6.17 counts/s) defines the boundary between Lithostratigraphic Unit I and Subunit IIA. Below the ~184 mbsf calcareous sediment/basalt contact, basalt units and volcaniclastic interbeds are distinguished by porosity (34.1 and 58.4 vol% in volcaniclastic interbeds versus 4.20 and 15.1 vol% in basalts) and thermal conductivity (1.05 to 1.33 W/[m·K] in volcaniclastic interbeds versus 1.66 to 1.77 W/[m·K] in basalts). Increases in MS/MSP, *P*-wave velocity, and GRA/MAD bulk density also

accompany the transition from volcaniclastic interbeds to basalt units. Physical properties measurements also appear to image mineralogical and compositional trends. Olivine-phyric lava flows correlate to higher (>3000 × $10^{-5}$ SI) MS/MSP at ~218 and ~253 mbsf, and an anomalously high NGR count at ~270 mbsf appears to correlate to a high-potassium aphyric basalt at the same depth.

# References


Abouchami, W., Hofmann, A.W., Galer, S.J.G., Frey, F.A., Eisele, J., and Feigenson, M., 2005. Lead isotopes reveal bilateral asymmetry and vertical continuity in the Hawaiian mantle plume. Nature, 434(7035):851–856. **https://doi.org/10.1038/nature03402**

Anderson, D.L., 2005. Scoring hotspots: the plume and plate paradigms. In Foulger, G.R., Natland, J.H., Presnall, D.C., and Anderson, D.L. (Eds.), Plates, Plumes and Paradigms. Special Paper - Geological Society of America, 388. **https://doi.org/10.1130/0-8137-2388-4.31**

Anderson, D.L., and Natland, J.H., 2014. Mantle updrafts and mechanisms of oceanic volcanism. Proceedings of the National Academy of Sciences of the United States of America, 111(41):E4298–E4304. **https://doi.org/10.1073/pnas.1410229111**

Besse, J., and Courtillot, V., 2002. Apparent and true polar wander and the geometry of the geomagnetic field over the last 200 Myr. Journal of Geophysical Research: Solid Earth, 107(B11):EPM6-1–EPM6-31. **https://doi.org/10.1029/2000JB000050**

Bird, R.T., Naar, D.F., Larson, R.L., Searle, R.C., and Scotese, C.R., 1998. Plate tectonic reconstructions of the Juan Fernandez microplate: transformation from internal shear to rigid rotation. Journal of Geophysical Research: Solid Earth, 103(B4):7049–7067. **https://doi.org/10.1029/97JB02133**

Butler, R.F., 1992. Paleomagnetism: Magnetic Domains to Geologic Terranes: Boston (Blackwell Science Publishing). **https://www.geo.arizona.edu/Paleomag/**

Camboa, L.A.P., and Rabinowitz, P.D., 1984. The evolution of the Rio Grande Rise in the southwest Atlantic Ocean. Marine Geology, 58(1–2):35–58. **https://doi.org/10.1016/0025-3227(84)90115-4**

Cande, S.C., Raymond, C.A., Stock, J., and Haxby, W.F., 1995. Geophysics of the Pitman Fracture Zone and Pacific-Antarctic plate motions during the Cenozoic. Science, 270(5238):947–953. **https://doi.org/10.1126/science.270.5238.947**

Chandler, M.T., Wessel, P., Taylor, B., Seton, M., Kim, S.-S., and Hyeong, K., 2012. Reconstructing Ontong Java Nui: implications for Pacific absolute plate motion, hotspot drift and true polar wander. Earth and Planetary Science Letters, 331–332:140–151. **https://doi.org/10.1016/j.epsl.2012.03.017**

Chave, A.D., 1984. Lower Paleocene-Upper Cretaceous magnetostratigraphy, Sites 525, 527, 528, and 529, Deep Sea Drilling Project Leg 74. In Moore, T.C., Jr., Rabinowitz, P.D., et al., Initial Reports of the Deep Sea Drilling Project, 74: Washington, DC (US Government Printing Office), 525–531. **https://doi.org/10.2973/dsdp.proc.74.110.1984**

Clague, D.A., and Dalrymple, G.B., 1989. Tectonics, geochronology, and origin of the Hawaiian-Emperor volcanic chain. In Kay, E.A., A Natural History of the Hawaiian Islands: Honolulu, HI (University of Hawaii Press), 5–40. **https://doi.org/10.1515/9780824844264-003**

Class, C., and Goldstein, S.L., 2005. Evolution of helium isotopes in the Earth's mantle. Nature, 436(7054):1107–1112. **https://doi.org/10.1038/nature03930**

Class, C., Koppers, A., Sager, W., and Schnur, S., 2015. Walvis Ridge-Tristan-Gough, South Atlantic—triple-zonation of a plume over 60 Ma and role of LLSVP. Presented at the Goldschmidt Conference Prague, Czech Republic, 16–21 August 2015. **https://goldschmidtabstracts.info/2015/568.pdf**

Class, C., Koppers, A.A.P., Sager, W.W., and Schnur, S., 2014. Diffuse volcanism at the young end of the Walvis Ridge-Tristan-Gough Seamount Province: geochemical sampling and constraints on plume dynamics. Presented at the American Geophysical Union Fall Meeting, San Francisco, CA, 15–19 December 2014. **https://agu.confex.com/agu/fm14/meetingapp.cgi/Paper/27669**

Contreras, E., García, P.J., Sager, W.W., Thoram, S., Hoernle, K., Sarralde, R., and Zhou, H., 2022. Bathymetry of Valdivia Bank, Walvis Ridge, South Atlantic Ocean: implications for structure and geologic history of a hot spot plateau. Geochemistry, Geophysics, Geosystems, 23(11):e2022GC010624. **https://doi.org/10.1029/2022GC010624**

Coupland, D.H., and Van der Voo, R., 1980. Long-term nondipole components in the geomagnetic field during the last 130 m.y. Journal of Geophysical Research: Solid Earth, 85(B7):3529–3548. **https://doi.org/10.1029/JB085iB07p03529**

Courtillot, V., Davaille, A., Besse, J., and Stock, J., 2003. Three distinct types of hotspots in the Earth's mantle. Earth and Planetary Science Letters, 205(3–4):295–308. **https://doi.org/10.1016/S0012-821X(02)01048-8**

Creveling, J.R., Mitrovica, J.X., Chan, N.H., Latychev, K., and Matsuyama, I., 2012. Mechanisms for oscillatory true polar wander. Nature, 491(7423):244–248. **https://doi.org/10.1038/nature11571**

Doubrovine, P.V., Steinberger, B., and Torsvik, T.H., 2012. Absolute plate motions in a reference frame defined by moving hot spots in the Pacific, Atlantic, and Indian oceans. Journal of Geophysical Research: Solid Earth, 117(B9):B09101. **https://doi.org/10.1029/2011JB009072**

Duncan, R.A., 1981. Hotspots in the Southern Oceans—an absolute frame of reference for motion of the Gondwana continents. Tectonophysics, 74(1–2):29–42. **https://doi.org/10.1016/0040-1951(81)90126-8**

Duncan, R.A., and Clague, D.A., 1985. Pacific plate motion recorded by linear volcanic chains. In Nairn, A.E.M., Stehli, F.G. and Uyeda, S., The Pacific Ocean. The Ocean Basins and Margins, 7A: New York (Plenum), 89–121. **https://doi.org/10.1007/978-1-4613-2351-8_3**

Ernesto, M., Pacca, I.G., Hiodo, F.Y., and Nardy, A.J.R., 1990. Palaeomagnetism of the Mesozoic Serra Geral Formation, southern Brazil. Physics of the Earth and Planetary Interiors, 64(2):153–175. **https://doi.org/10.1016/0031-9201(90)90035-V**

Ernesto, M., Raposo, M.I.B., Marques, L.S., Renne, P.R., Diogo, L.A., and de Min, A., 1999. Paleomagnetism, geochemistry and $^{40}Ar/^{39}Ar$ dating of the north-eastern Paraná Magmatic Province: tectonic implications. Journal of Geodynamics, 28(4):321–340. **https://doi.org/10.1016/S0264-3707(99)00013-7**

Expedition 324 Scientists, 2010. Expedition 324 summary. In Sager, W.W., Sano, T., Geldmacher, J., and the Expedition 324 Scientists, Proceedings of the Integrated Ocean Drilling Program. 324: Tokyo (Integrated Ocean Drilling Program Management International, Inc.). **https://doi.org/10.2204/iodp.proc.324.101.2010**

Fairhead, J.D., and Wilson, M., 2005. Plate tectonic processes in the South Atlantic Ocean: do we need deep mantle plumes? In Plates, Plumes and Paradigms. Special Paper - Geological Society of America, 388. **https://doi.org/10.1130/0-8137-2388-4.537**

Farnetani, C.G., and Hofmann, A.W., 2009. Dynamics and internal structure of a lower mantle plume conduit. Earth and Planetary Science Letters, 282(1–4):314–322. **https://doi.org/10.1016/j.epsl.2009.03.035**

Farnetani, C.G., Hofmann, A.W., and Class, C., 2012. How double volcanic chains sample geochemical anomalies from the lowermost mantle. Earth and Planetary Science Letters, 359–360:240–247. **https://doi.org/10.1016/j.epsl.2012.09.057**

Farnetani, C.G., and Samuel, H., 2005. Beyond the thermal plume paradigm. Geophysical Research Letters, 32(7):L07311. **https://doi.org/10.1029/2005GL022360**

Fitton, J.G., and Godard, M., 2004. Origin and evolution of magmas on the Ontong Java Plateau. In Fitton, J.G., Mahoney, J.J., Wallace, P.J., and Saunders, A.D. (Eds.), Origin and Evolution of the Ontong Java Plateau. Geological Society Special Publication, 229(1):151–178. **https://doi.org/10.1144/GSL.SP.2004.229.01.10**

Foulger, G.R., 2005. Mantle plumes: why the current skepticism? Chinese Science Bulletin, 50(15):1555–1560. **https://doi.org/10.1360/982005-919**

Foulger, G.R., 2007. The "plate" model for the genesis of melting anomalies. In Foulger, G.R., and Jurdy, D.M. (Eds.), Plates, Plumes and Planetary Processes. Special Paper - Geological Society of America 430. **https://doi.org/10.1130/2007.2430(01)**

Foulger, G.R., 2018. Origin of the South Atlantic igneous province. Journal of Volcanology and Geothermal Research, 355:2–20. **https://doi.org/10.1016/j.jvolgeores.2017.09.004**

French, S.W., and Romanowicz, B., 2015. Broad plumes rooted at the base of the Earth's mantle beneath major hotspots. Nature, 525(7567):95–99. **https://doi.org/10.1038/nature14876**

Frey, F.A., Weis, D., Borisova, A.Y., and Xu, G., 2002. Involvement of continental crust in the formation of the Cretaceous Kerguelen Plateau: new perspectives from ODP Leg 120 sites. Journal of Petrology, 43(7):1207–1239. **https://doi.org/10.1093/petrology/43.7.1207**

Gold, T., 1955. Instability of the Earth's axis of rotation. Nature, 175(4456):526–529. **https://doi.org/10.1038/175526a0**

Goldreich, P., and Toomre, A., 1969. Some remarks on polar wandering. Journal of Geophysical Research, 74(10):2555–2567. **https://doi.org/10.1029/JB074i010p02555**

Gordon, R.G., 1982. Paleomagnetic test of the Emperor Fracture Zone Hypothesis. Geophysical Research Letters, 9(11):1283–1286. **https://doi.org/10.1029/GL009i011p01283**

Gordon, R.G., 1987. Polar wandering and paleomagnetism. Annual Review of Earth and Planetary Sciences, 15(1):567–593. **https://doi.org/10.1146/annurev.ea.15.050187.003031**

Gordon, R.G., and Cape, C.D., 1981. Cenozoic latitudinal shift of the Hawaiian hotspot and its implications for true polar wander. Earth and Planetary Science Letters, 55(1):37–47. **https://doi.org/10.1016/0012-821X(81)90084-4**

Gradstein, F.M., Ogg, J.G., Schmitz, M.D., and Ogg, G.M. (Eds.), 2012. The Geologic Time Scale 2012: Amsterdam (Elsevier). **https://doi.org/10.1016/C2011-1-08249-8**

Gradstein, F.M., Ogg, J.G., Schmitz, M.D., and Ogg, G.M. (Eds.), 2020. The Geologic Time Scale 2020: Amsterdam (Elsevier BV). **https://doi.org/10.1016/C2020-1-02369-3**

Harrison, L.N., Weis, D., and Garcia, M.O., 2017. The link between Hawaiian mantle plume composition, magmatic flux, and deep mantle geodynamics. Earth and Planetary Science Letters, 463:298–309. **https://doi.org/10.1016/j.epsl.2017.01.027**

Heydolph, K., Murphy, D.T., Geldmacher, J., Romanova, I.V., Greene, A., Hoernle, K., Weis, D., and Mahoney, J., 2014. Plume versus plate origin for the Shatsky Rise oceanic plateau (NW Pacific): insights from Nd, Pb and Hf isotopes. Lithos, 200–201:49–63. **https://doi.org/10.1016/j.lithos.2014.03.031**

Hoernle, K., Rohde, J., Hauff, F., Garbe-Schönberg, D., Homrighausen, S., Werner, R., and Morgan, J.P., 2015. How and when plume zonation appeared during the 132Myr evolution of the Tristan Hotspot. Nature Communications, 6(1):7799. **https://doi.org/10.1038/ncomms8799**

Hoernle, K., Schwindrofska, A., Werner, R., van den Bogaard, P., Hauff, F., Uenzelmann-Neben, G., and Garbe-Schönberg, D., 2016. Tectonic dissection and displacement of parts of Shona hotspot volcano 3500 km along the Agulhas-Falkland Fracture Zone. Geology, 44(4):263–266. **https://doi.org/10.1130/G37582.1**

Hoernle, K., Werner, R., Morgan, J.P., Garbe-Schönberg, D., Bryce, J., and Mrazek, J., 2000. Existence of complex spatial zonation in the Galápagos plume. Geology, 28(5):435–438. **https://doi.org/10.1130/0091-7613(2000)28<435:EOCSZI>2.0.CO;2**

Homrighausen, S., Hoernle, K., Geldmacher, J., Wartho, J.A., Hauff, F., Portnyagin, M., Werner, R., van den Bogaard, P., and Garbe-Schönberg, D., 2018. Unexpected HIMU-type late-stage volcanism on the Walvis Ridge. Earth and Planetary Science Letters, 492:251–263. **https://doi.org/10.1016/j.epsl.2018.03.049**

Homrighausen, S., Hoernle, K., Hauff, F., Wartho, J.A., van den Bogaard, P., and Garbe-Schönberg, D., 2019. New age and geochemical data from the Walvis Ridge: the temporal and spatial diversity of South Atlantic intraplate volcanism and its possible origin. Geochimica et Cosmochimica Acta, 245:16–34. **https://doi.org/10.1016/j.gca.2018.09.002**

Homrighausen, S., Hoernle, K., Zhou, H., Geldmacher, J., Wartho, J.-A., Hauff, F., Werner, R., Jung, S., and Morgan, J.P., 2020. Paired EMI-HIMU hotspots in the South Atlantic—starting plume heads trigger compositionally distinct secondary plumes? Science Advances, 6(28):eaba0282. **https://doi.org/10.1126/sciadv.aba0282**

Huang, Y., Sager, W.W., Tominaga, M., Greene, J.A., Zhang, J., and Nakanishi, M., 2018. Magnetic anomaly map of Ori Massif and its implications for oceanic plateau formation. Earth and Planetary Science Letters, 501:46–55. **https://doi.org/10.1016/j.epsl.2018.08.029**

Huang, Z., Zhao, D., and Wang, L., 2011. Seismic heterogeneity and anisotropy of the Honshu arc from the Japan Trench to the Japan Sea. Geophysical Journal International, 184(3):1428–1444. **https://doi.org/10.1111/j.1365-246X.2011.04934.x**

Husen, A., Almeev, R.R., Holtz, F., Koepke, J., Sano, T., and Mengel, K., 2013. Geothermobarometry of basaltic glasses from the Tamu Massif, Shatsky Rise oceanic plateau. Geochemistry, Geophysics, Geosystems, 14(10):3908–3928. **https://doi.org/10.1002/ggge.20231**

Ingle, S., Weis, D., and Frey, F.A., 2002. Indian continental crust recovered from Elan Bank, Kerguelen Plateau (ODP Leg 183, Site 1137). Journal of Petrology, 43(7):1241–1257. **https://doi.org/10.1093/petrology/43.7.1241**

Jackson, M.G., and Carlson, R.W., 2011. An ancient recipe for flood-basalt genesis. Nature, 476(7360):316–319. **https://doi.org/10.1038/nature10326**

Jackson, M.G., Hart, S.R., Konter, J.G., Kurz, M.D., Blusztajn, J., and Farley, K.A., 2014. Helium and lead isotopes reveal the geochemical geometry of the Samoan plume. Nature, 514(7522):355–358. **https://doi.org/10.1038/nature13794**

Jiménez García, P., 2017. Análisis morfo-sedimentario del Banco de Valdivia (sector central de la Dorsal de Walvis) Atlántico Sur [PhD dissertation]. Universidad Complutense de Madrid, Madrid, Spain.

Kerr, R.C., and Mériaux, C., 2004. Structure and dynamics of sheared mantle plumes. Geochemistry, Geophysics, Geosystems, 5(12):Q12009. **https://doi.org/10.1029/2004GC000749**

Kirschvink, J.L., Ripperdan, R.L., and Evans, D.A., 1997. Evidence for a large-scale reorganization of early Cambrian continental masses by inertial interchange true polar wander. Science, 277(5325):541–545. **https://doi.org/10.1126/science.277.5325.541**

Koivisto, E.A., Andrews, D.L., and Gordon, R.G., 2014. Tests of fixity of the Indo-Atlantic hot spots relative to Pacific hot spots. Journal of Geophysical Research: Solid Earth, 119(1):661–675. **https://doi.org/10.1002/2013JB010413**

Kono, M., 1980. Paleomagnetism of DSDP Leg 55 basalts and implications for the tectonics of the Pacific Plate. In Jackson, E.D., Koisumi, I., et al., Initial Reports of the Deep Sea Drilling Project, 55: Washington, DC (US Government Printing Office), 737–752. **https://doi.org/10.2973/dsdp.proc.55.135.1980**

Koppers, A.A.P., Becker, T.W., Jackson, M.G., Konrad, K., Müller, R.D., Romanowicz, B., Steinberger, B., and Whittaker, J.M., 2021. Mantle plumes and their role in Earth processes. Nature Reviews Earth & Environment, 2(6):382–401. **https://doi.org/10.1038/s43017-021-00168-6**

Koppers, A.A.P., Duncan, R.A., and Steinberger, B., 2004. Implications of a nonlinear $^{40}Ar/^{39}Ar$ age progression along the Louisville Seamount Trail for models of fixed and moving hot spots. Geochemistry, Geophysics, Geosystems, 5(6):21803–21824. **https://doi.org/10.1029/2003GC000671**

Koppers, A.A.P., Gowen, M.D., Colwell, L.E., Gee, J.S., Lonsdale, P.F., Mahoney, J.J., and Duncan, R.A., 2011. New $^{40}Ar/^{39}Ar$ age progression for the Louisville hot spot trail and implications for inter–hot spot motion. Geochemistry, Geophysics, Geosystems, 12(12):Q0AM02. **https://doi.org/10.1029/2011GC003804**

Koppers, A.A.P., Yamazaki, T., Geldmacher, J., Gee, J.S., Pressling, N., Hoshi, H., Anderson, L., Beier, C., Buchs, D.M., Chen, L.H., Cohen, B.E., Deschamps, M., Dorais, J., Ebuna, D., Ehmann, S., Fitton, J.G., Fulton, P.M., Ganbat, E., Hamelin, C., Hanyu, T., Kalnins, L., Kell, J., Machida, S., Mahoney, J.J., Moriya, K., Nichols, A.R.L., Rausch, S., Sano, S., Sylvan, J.B., and Williams, R., 2012. Limited latitudinal mantle plume motion for the Louisville Hotspot. Nature Geoscience, 5(12):911–917. **https://doi.org/10.1038/ngeo1638**

Krishna, K.S., Abraham, H., Sager, W.W., Pringle, M.S., Frey, F., Gopala Rao, D., and Levchenko, O.V., 2012. Tectonics of the Ninetyeast Ridge derived from spreading records in adjacent oceanic basins and age constraints of the ridge. Journal of Geophysical Research: Solid Earth, 117(B4):B04101. **https://doi.org/10.1029/2011JB008805**

Liu, H., and Leng, W., 2020. Plume-tree structure induced by low-viscosity layers in the upper mantle. Geophysical Research Letters, 47(1):e2019GL086508. **https://doi.org/10.1029/2019GL086508**

Livermore, R.A., Vine, F.J., and Smith, A.G., 1984. Plate motions and the geomagnetic field — II. Jurassic to Tertiary. Geophysical Journal International, 79(3):939–961. **https://doi.org/10.1111/j.1365-246X.1984.tb02878.x**

Lohmann, F.C., Hort, M., and Phipps Morgan, J., 2009. Flood basalts and ocean island basalts: a deep source or shallow entrainment? Earth and Planetary Science Letters, 284(3–4):553–563. **https://doi.org/10.1016/j.epsl.2009.05.025**

Mahoney, J.J., and Spencer, K.J., 1991. Isotopic evidence for the origin of the Manihiki and Ontong Java oceanic plateaus. Earth and Planetary Science Letters, 104(2–4):196–210. **https://doi.org/10.1016/0012-821X(91)90204-U**

McElhinny, M.W., McFadden, P.L., and Merrill, R.T., 1996. The time-averaged paleomagnetic field 0–5 Ma. Journal of Geophysical Research: Solid Earth, 101(B11):25007–25027. **https://doi.org/10.1029/96JB01911**

Mitchell, R.N., Thissen, C.J., Evans, D.A.D., Slotznick, S.P., Coccioni, R., Yamazaki, T., and Kirschvink, J.L., 2021. A Late Cretaceous true polar wander oscillation. Nature Communications, 12(1):3629. **https://doi.org/10.1038/s41467-021-23803-8**

Mohriak, W.U., Nóbrega, M., Odegard, M.E., Gomes, B.S., and Dickson, W.G., 2010. Geological and geophysical interpretation of the Rio Grande Rise, south-eastern Brazilian margin: extensional tectonics and rifting of continental and oceanic crusts. Petroleum Geoscience, 16(3):231–245. **https://doi.org/10.1144/1354-079309-910**

Montelli, R., Nolet, G., Dahlen, F.A., and Masters, G., 2006. A catalogue of deep mantle plumes: new results from finite-frequency tomography. Geochemistry, Geophysics, Geosystems, 7(11):Q11007. **https://doi.org/10.1029/2006GC001248**

Moore, T.C., Jr., Rabinowitz, P.D., Borella, P.E., Boersma, A., and Shackleton, N.J., 1984. Introduction and explanatory notes. In Moore, T.C., Jr., Rabinowitz, P. D., et al., Initial Reports of the Deep Sea Drilling Project, 74: Washington, DC (US Government Printing Office), 3–39. **https://doi.org/10.2973/dsdp.proc.74.101.1984**

Morgan, W.J., 1971. Convection plumes in the lower mantle. Nature, 230(5288):42–43. **https://doi.org/10.1038/230042a0**

Morgan, W.J., 1972. Deep mantle convection plumes and plate motions. AAPG Bulletin, 56(2):203–213. **https://doi.org/10.1306/819A3E50-16C5-11D7-8645000102C1865D**

Morgan, W.J., 1981. Hotspot tracks and the opening of the Atlantic and Indian Oceans. In Emiliani, C., The Sea. 7: New York (Wiley), 443–487. **https://adsabs.harvard.edu/full/1981LPICo.457....1M**

Müller, R.D., Royer, J.-Y., and Lawver, L.A., 1993. Revised plate motions relative to the hotspots from combined Atlantic and Indian Ocean hotspot tracks. Geology, 21(3):275–278. **https://doi.org/10.1130/0091-7613(1993)021<0275:RPMRTT>2.3.CO;2**

Müller, R.D., Sdrolias, M., Gaina, C., and Roest, W.R., 2008. Age, spreading rates, and spreading asymmetry of the world's ocean crust. Geochemistry, Geophysics, Geosystems, 9(4):Q04006. **https://doi.org/10.1029/2007GC001743**

Nakanishi, M., Nakamura, Y., Coffin, M.F., Hoernle, K., Werner, R., Neal, C.R., Sager, W.W., Sano, T., and Erba, E., 2015. Topographic expression of the Danger Islands Troughs and implications for the tectonic evolution of the Manihiki Plateau, western equatorial Pacific Ocean. In Neal, C.R., Sager, W.W., Sano, T., and Erba, E. (Eds.), The Origin, Evolution, and Environmental Impact of Oceanic Large Igneous Provinces. Special Paper - Geological Society of America, 511. **https://doi.org/10.1130/2015.2511(11)**

O'Connor, J.M., and Duncan, R.A., 1990. Evolution of the Walvis Ridge-Rio Grande Rise hot spot system: implications for African and South American plate motions over plumes. Journal of Geophysical Research: Solid Earth, 95(B11):17475–17502. **https://doi.org/10.1029/JB095iB11p17475**

O'Connor, J.M., and Jokat, W., 2015a. Age distribution of ocean drill sites across the Central Walvis Ridge indicates plate boundary control of plume volcanism in the South Atlantic. Earth and Planetary Science Letters, 424:179–190. **https://doi.org/10.1016/j.epsl.2015.05.021**

O'Connor, J.M., and Jokat, W., 2015b. Tracking the Tristan-Gough mantle plume using discrete chains of intraplate volcanic centers buried in the Walvis Ridge. Geology, 43(8):715–718. **https://doi.org/10.1130/G36767.1**

O'Connor, J.M., Jokat, W., le Roex, A.P., Class, C., Wijbrans, J.R., Keßling, S., Kuiper, K.F., and Nebel, O., 2012. Hotspot trails in the South Atlantic controlled by plume and plate tectonic processes. Nature Geoscience, 5(10):735–738. **https://doi.org/10.1038/ngeo1583**

O'Connor, J.M., and le Roex, A.P., 1992. South Atlantic hot spot-plume systems: 1. Distribution of volcanism in time and space. Earth and Planetary Science Letters, 113(3):343–364. **https://doi.org/10.1016/0012-821X(92)90138-L**

O'Connor, J.M., Stoffers, P., van den Bogaard, P., and McWilliams, M., 1999. First seamount age evidence for significantly slower African plate motion since 19 to 30 Ma. Earth and Planetary Science Letters, 171(4):575–589. **https://doi.org/10.1016/S0012-821X(99)00183-1**

Ogg, J.G., 2020. Geomagnetic Polarity Time Scale. In Gradstein, F.M., Ogg, J.G., Schmitz, M., and Ogg, G. (Eds.), Geologic Time Scale 2020. Amsterdam (Elsevier), 159–192.

O'Neill, C., Müller, D., and Steinberger, B., 2005. On the uncertainties in hot spot reconstructions and the significance of moving hot spot reference frames. Geochemistry, Geophysics, Geosystems, 6(4):Q04003. **https://doi.org/10.1029/2004GC000784**

Pietsch, R., and Uenzelmann-Neben, G., 2016. Paleocene Pacific Plate reorganization mirrored in formation of the Suvarov Trough, Manihiki Plateau. Journal of Geophysical Research: Solid Earth, 121(10):7013-7023. **https://doi.org/10.1002/2016JB013355**

Portnyagin, M., Savelyev, D., Hoernle, K., Hauff, F., and Garbe-Schönberg, D., 2008. Mid-Cretaceous Hawaiian tholeiites preserved in Kamchatka. Geology, 36(11):903–906. **https://doi.org/10.1130/G25171A.1**

Prévot, M., Mattern, E., Camps, P., and Daignières, M., 2000. Evidence for a 20° tilting of the Earth's rotation axis 110 million years ago. Earth and Planetary Science Letters, 179(3–4):517–528. **https://doi.org/10.1016/S0012-821X(00)00129-1**

Raymond, C.A., Stock, J.M., and Cande, S.C., 2000. Fast Paleogene motion of the Pacific hotspots from revised global plate circuit constraints. In Richards, M.A., Gordon, R.G., and Van Der Hilst, R.D. (Eds.), The History and Dynamics of Global Plate Motions. Geophysical Monograph, 121: 359–375. **https://doi.org/10.1029/GM121p0359**

Renne, P.R., Scott, G.R., Glen, J.M.G., and Feinberg, J.M., 2002. Oriented inclusions of magnetite in clinopyroxene: source of stable remanent magnetization in gabbros of the Messum Complex, Namibia. Geochemistry, Geophysics, Geosystems, 3(12):1–11. **https://doi.org/10.1029/2002GC000319**

Richards, M.A., Duncan, R.A., and Courtillot, V.E., 1989. Flood basalts and hot-spot tracks: plume heads and tails. Science, 246(4926):103–107. **https://doi.org/10.1126/science.246.4926.103**

Rohde, J., Hoernle, K., Hauff, F., Werner, R., O'Connor, J., Class, C., Garbe-Schönberg, D., and Jokat, W., 2013a. 70 Ma chemical zonation of the Tristan-Gough hotspot track. Geology, 41(3):335–338. **https://doi.org/10.1130/G33790.1**

Rohde, J.K., van den Bogaard, P., Hoernle, K., Hauff, F., and Werner, R., 2013b. Evidence for an age progression along the Tristan-Gough volcanic track from new $^{40}Ar/^{39}Ar$ ages on phenocryst phases. Tectonophysics, 604:60–71. **https://doi.org/10.1016/j.tecto.2012.08.026**

Sager, W., Hoernle, K., and Petronotis, K., 2020. Expedition 391 Scientific Prospectus: Walvis Ridge Hotspot. International Ocean Discovery Program. **https://doi.org/10.14379/iodp.sp.391.2020**

Sager, W.W., 2005. What built Shatsky Rise, a mantle plume or ridge tectonics? In Foulger, G.R., Natland, J.H., Presnall, D.C., and Anderson, D.L. (Eds.), Plates, Plumes and Paradigms. Special Paper - Geological Society of America, 388. **https://doi.org/10.1130/0-8137-2388-4.721**

Sager, W.W., Engfer, D., Thoram, S., Koppers, A.A.P., and Class, C., 2015. Seafloor tectonic fault fabric and the evolution of the Walvis Ridge-Rio Grande Rise hot spot twins in the South Atlantic. Presented at the American Geophysical Union Fall Meeting, San Francisco, CA, 14–18 December 2015. **https://abstractsearch.agu.org/meetings/2015/FM/V12A-08.html**

Sager, W.W., Huang, Y., Tominaga, M., Greene, J.A., Nakanishi, M., and Zhang, J., 2019. Oceanic plateau formation by seafloor spreading implied by Tamu Massif magnetic anomalies. Nature Geoscience, 12(8):661–666. **https://doi.org/10.1038/s41561-019-0390-y**

Sager, W.W., Kim, J., Klaus, A., Nakanishi, M., and Khankishieva, L.M., 1999. Bathymetry of Shatsky Rise, northwest Pacific Ocean: implications for ocean plateau development at a triple junction. Journal of Geophysical Research: Solid Earth, 104(B4):7557–7576. **https://doi.org/10.1029/1998JB900009**

Sager, W.W., Sano, T., and Geldmacher, J., 2016. Formation and evolution of Shatsky Rise oceanic plateau: insights from IODP Expedition 324 and recent geophysical cruises. Earth-Science Reviews, 159:306–336. **https://doi.org/10.1016/j.earscirev.2016.05.011**

Sager, W.W., Thoram, S., Engfer, D.W., Koppers, A.A.P., and Class, C., 2021. Late Cretaceous Ridge reorganization, microplate formation, and the evolution of the Rio Grande Rise – Walvis Ridge hot spot twins, South Atlantic Ocean. Geochemistry, Geophysics, Geosystems, 22(3):e2020GC009390. **https://doi.org/10.1029/2020GC009390**

Salters, V.J.M., and Sachi-Kocher, A., 2010. An ancient metasomatic source for the Walvis Ridge basalts. Chemical Geology, 273(3–4):151–167. **https://doi.org/10.1016/j.chemgeo.2010.02.010**

Sano, T., Shimizu, K., Ishikawa, A., Senda, R., Chang, Q., Kimura, J.-I., Widdowson, M., and Sager, W.W., 2012. Variety and origin of magmas on Shatsky Rise, Northwest Pacific Ocean. Geochemistry, Geophysics, Geosystems, 13(8):Q08010. **https://doi.org/10.1029/2012GC004235**

Santos, R.V., Ganade, C.E., Lacasse, C.M., Costa, I.S.L., Pessanha, I., Frazão, E.P., Dantas, E.L., and Cavalcante, J.A., 2019. Dating Gondwanan continental crust at the Rio Grande Rise, South Atlantic. Terra Nova, 31(5):424–429. **https://doi.org/10.1111/ter.12405**

Sarda, P., Moreira, M., Staudacher, T., Schilling, J.-G., and Allègre, C.J., 2000. Rare gas systematics on the southernmost Mid-Atlantic Ridge: constraints on the lower mantle and the Dupal source. Journal of Geophysical Research: Solid Earth, 105(B3):5973–5996. **https://doi.org/10.1029/1999JB900282**

Schlömer, A., Geissler, W.H., Jokat, W., and Jegen, M., 2017. Hunting for the Tristan mantle plume – an upper mantle tomography around the volcanic island of Tristan da Cunha. Earth and Planetary Science Letters, 462:122–131. **https://doi.org/10.1016/j.epsl.2016.12.028**

Schouten, H., Klitgord, K.D., and Gallo, D.G., 1993. Edge-driven microplate kinematics. Journal of Geophysical Research: Solid Earth, 98(B4):6689–6701. **https://doi.org/10.1029/92JB02749**

Schwindrofska, A., Hoernle, K., Hauff, F., van den Bogaard, P., Werner, R., and Garbe-Schönberg, D., 2016. Origin of enriched components in the South Atlantic: evidence from 40 Ma geochemical zonation of the Discovery Seamounts. Earth and Planetary Science Letters, 441:167–177. **https://doi.org/10.1016/j.epsl.2016.02.041**

Seton, M., Flament, N., Whittaker, J., Müller, R.D., Gurnis, M., and Bower, D.J., 2015. Ridge subduction sparked reorganization of the Pacific plate-mantle system 60–50 million years ago. Geophysical Research Letters, 42(6):1732–1740. **https://doi.org/10.1002/2015GL063057**

Shipboard Scientific Party, 1984a. Introduction and explanatory notes, Deep Sea Drilling Project Leg 75. In Hay, W.W., Sibuet, J.-C., et al., Initial Reports of the Deep Sea Drilling Project. 75: 3–25. **https://doi.org/10.2973/dsdp.proc.75.101.1984**

Shipboard Scientific Party, 1984b. Site 526. In Moore, T.C., Jr., Rabinowitz, P.D., et al., Initial Reports of the Deep Sea Drilling Project 74: Washington, DC (US Government Printing Office), 161–235. **https://doi.org/10.2973/dsdp.proc.74.103.1984**

Shipboard Scientific Party, 2004. Leg 208 summary. In Zachos, J.C., Kroon, D., Blum, P., et al., Proceedings of the Ocean Drilling Program, Initial Reports, 208: College Station, TX (Ocean Drilling Program). **https://doi.org/10.2973/odp.proc.ir.208.101.2004**

Smith, W.H.F., and Sandwell, D.T., 1994. Bathymetric prediction from dense satellite altimetry and sparse shipboard bathymetry. Journal of Geophysical Research: Solid Earth, 99(B11):21803–21824. **https://doi.org/10.1029/94JB00988**

Smith, W.H.F., and Sandwell, D.T., 1997. Global sea floor topography from satellite altimetry and ship depth soundings. Science, 277(5334):1956–1962. **https://doi.org/10.1126/science.277.5334.1956**

Sobolev, A.V., Hofmann, A.W., Sobolev, S.V., and Nikogosian, I.K., 2005. An olivine-free mantle source of Hawaiian shield basalts. Nature, 434(7033):590–597. **https://doi.org/10.1038/nature03411**

Steinberger, B., 2000. Plumes in a convecting mantle: models and observations for individual hotspots. Journal of Geophysical Research: Solid Earth, 105(B5):11127–11152. **https://doi.org/10.1029/1999JB900398**

Steinberger, B., and O'Connell, R.J., 1998. Advection of plumes in mantle flow: implications for hotspot motion, mantle viscosity and plume distribution. Geophysical Journal International, 132(2):412–434. **https://doi.org/10.1046/j.1365-246x.1998.00447.x**

Steinberger, B., and O'Connell, R.J., 2000. Effects of mantle flow on hotspot motion. In Richards, M.A., Gordon, R.G., and Van Der Hilst, R.D. (Eds.), The History and Dynamics of Global Plate Motions. Geophysical Monograph, 121: 377–398. **https://doi.org/10.1029/GM121p0377**

Steinberger, B., Sutherland, R., and O'Connell, R.J., 2004. Prediction of Emperor-Hawaii seamount locations from a revised model of global plate motion and mantle flow. Nature, 430(6996):167–173. **https://doi.org/10.1038/nature02660**

Stock, J., and Molnar, P., 1987. Revised history of early Tertiary plate motion in the south-west Pacific. Nature, 325(6104):495–499. **https://doi.org/10.1038/325495a0**

Tamaki, K., and Larson, R.L., 1988. The Mesozoic tectonic history of the Magellan microplate in the western central Pacific. Journal of Geophysical Research: Solid Earth, 93(B4):2857–2874. **https://doi.org/10.1029/JB093iB04p02857**

Tarduno, J., Bunge, H.-P., Sleep, N., and Hansen, U., 2009. The bent Hawaiian-Emperor hotspot track: inheriting the mantle wind. Science, 324(5923):50–53. **https://doi.org/10.1126/science.1161256**

Tarduno, J.A., and Cottrell, R.D., 1997. Paleomagnetic evidence for motion of the Hawaiian hotspot during formation of the Emperor seamounts. Earth and Planetary Science Letters, 153(3–4):171–180. **https://doi.org/10.1016/S0012-821X(97)00169-6**

Tarduno, J.A., Duncan, R.A., Scholl, D.W., Cottrell, R.D., Steinberger, B., Thordarson, T., Kerr, B.C., Neal, C.R., Frey, F.A., Torii, M., and Carvallo, C., 2003. The Emperor seamounts: southward motion of the Hawaiian hotspot plume in Earth's mantle. Science, 301(5636):1064–1069. **https://doi.org/10.1126/science.1086442**

Taylor, B., 2006. The single largest oceanic plateau: Ontong Java–Manihiki–Hikurangi. Earth and Planetary Science Letters, 241(3–4):372–380. **https://doi.org/10.1016/j.epsl.2005.11.049**

The Shipboard Scientific Party, 1977. Site 359: Walvis Ridge (seamount). In Supko, P.R., Perch-Nielsen, K., et al., Initial Reports of the Deep Sea Drilling Project. 39: Washington, DC (US Government Printing Office), 373–391. **https://doi.org/10.2973/dsdp.proc.39.108.1977**

The Shipboard Scientific Party, 1978. Walvis Ridge—Sites 362 and 363. In Bolli, H.M., Ryan, W.B.F., et al., Initial Reports of the Deep Sea Drilling Project. 40: Washington, DC (US Government Printing Office), 183–356. **https://doi.org/10.2973/dsdp.proc.40.103.1978**

Thoram, S., Sager, W.W., and Jokat, W., 2019. Implications of updated magnetic anomalies for the Late Cretaceous tectonic evolution of Walvis Ridge. Geophysical Research Letters, 46(16):9474–9482. **https://doi.org/10.1029/2019GL083467**

Tolstikhin, I., and Hofmann, A.W., 2005. Early crust on top of the Earth's core. Physics of the Earth and Planetary Interiors, 148(2–4):109–130. **https://doi.org/10.1016/j.pepi.2004.05.011**

Torsvik, T.H., Amundsen, H., Hartz, E.H., Corfu, F., Kusznir, N., Gaina, C., Doubrovine, P.V., Steinberger, B., Ashwal, L.D., and Jamtveit, B., 2013. A Precambrian microcontinent in the Indian Ocean. Nature Geoscience, 6(3):223–227. **https://doi.org/10.1038/ngeo1736**

Torsvik, T.H., Amundsen, H.E.F., Trønnes, R.G., Doubrovine, P.V., Gaina, C., Kusznir, N.J., Steinberger, B., Corfu, F., Ashwal, L.D., Griffin, W.L., Werner, S.C., and Jamtveit, B., 2015. Continental crust beneath southeast Iceland. Proceedings of the National Academy of Sciences of the United States of America, 112(15):E1818–E1827. **https://doi.org/10.1073/pnas.1423099112**

Torsvik, T.H., Müller, R.D., Van der Voo, R., Steinberger, B., and Gaina, C., 2008. Global plate motion frames: toward a unified model. Reviews of Geophysics, 46(3):RG3004. **https://doi.org/10.1029/2007RG000227**

Torsvik, T.H., Smethurst, M.A., Burke, K., and Steinberger, B., 2006. Large igneous provinces generated from the margins of the large low-velocity provinces in the deep mantle. Geophysical Journal International, 167(3):1447–1460. **https://doi.org/10.1111/j.1365-246X.2006.03158.x**

Tozer, B., Sandwell, D.T., Smith, W.H.F., Olson, C., Beale, J.R., and Wessel, P., 2019. Global bathymetry and topography at 15 arc sec: SRTM15+. Earth and Space Science, 6(10):1847–1864. **https://doi.org/10.1029/2019EA000658**

van der Linden, W.J.M., 1980. Walvis Ridge, a piece of Africa? Geology, 8(9):417–421. **https://doi.org/10.1130/0091-7613(1980)8<417:WRAPOA>2.0.CO;2**

Van Fossen, M.C., and Kent, D.V., 1992. Paleomagnetism of 122 Ma plutons in New England and the mid-Cretaceous paleomagnetic field in North America: true polar wander or large-scale differential mantle motion? Journal of Geophysical Research: Solid Earth, 97(B13):19651–19661. **https://doi.org/10.1029/92JB01466**

Verosub, K.L., 1977. Depositional and postdepositional processes in the magnetization of sediments. Reviews of Geophysics, 15(2):129–143. **https://doi.org/10.1029/RG015i002p00129**

Wang, C., Gordon, R.G., Zhang, T., and Zheng, L., 2019. Observational test of the global moving hot spot reference frame. Geophysical Research Letters, 46(14):8031–8038. **https://doi.org/10.1029/2019GL083663**

Weis, D., Garcia, M.O., Rhodes, J.M., Jellinek, M., and Scoates, J.S., 2011. Role of the deep mantle in generating the compositional asymmetry of the Hawaiian mantle plume. Nature Geoscience, 4(12):831–838. **https://doi.org/10.1038/ngeo1328**

Werner, R., Hoernle, K., Barckhausen, U., and Hauff, F., 2003. Geodynamic evolution of the Galápagos hot spot system (central East Pacific) over the past 20 m.y.: constraints from morphology, geochemistry, and magnetic anomalies. Geochemistry, Geophysics, Geosystems, 4(12):1108. **https://doi.org/10.1029/2003GC000576**

Wessel, P., and Müller, R.D., 2016. Ridge-spotting: a new test for Pacific absolute plate motion models. Geochemistry, Geophysics, Geosystems, 17(6):2408–2420. **https://doi.org/10.1002/2016GC006404**

Whittaker, J.M., Afonso, J.C., Masterton, S., Müller, R.D., Wessel, P., Williams, S.E., and Seton, M., 2015. Long-term interaction between mid-ocean ridges and mantle plumes. Nature Geoscience, 8(6):479–483. **https://doi.org/10.1038/ngeo2437**

Wilson, J.T., 1963. A possible origin of the Hawaiian Islands. Canadian Journal of Physics, 41(6):863–870. **https://doi.org/10.1139/p63-094**

Woodworth, D., and Gordon, R.G., 2018. Paleolatitude of the Hawaiian hot spot Since 48 Ma: evidence for a mid-Cenozoic true polar stillstand followed by late Cenozoic true polar wander coincident with Northern Hemisphere glaciation. Geophysical Research Letters, 45(21):11632–11640. **https://doi.org/10.1029/2018GL080787**

Zheng, L., Gordon, R.G., and Woodworth, D., 2018. Pacific plate apparent polar wander, hot spot fixity, and true polar wander during the formation of the Hawaiian Island and Seamount Chain from an analysis of the skewness of magnetic anomaly 20r (44 Ma). Tectonics, 37(7):2094–2105. **https://doi.org/10.1029/2017TC004897**

Zhou, H., Hoernle, K., Geldmacher, J., Hauff, F., Homrighausen, S., Garbe-Schönberg, D., and Jung, S., 2020. Geochemistry of Etendeka magmatism: spatial heterogeneity in the Tristan-Gough plume head. Earth and Planetary Science Letters, 535:116123. **https://doi.org/10.1016/j.epsl.2020.116123**